Ferroelectric-on-Silicon Switchable Bulk Acoustic Wave Resonators and Filters for RF Applications

by

Seyit Ahmet Sis

A dissertation submitted in partial fulfillment of the
requirements for the degree of
Doctor of Philosophy
(Electrical Engineering)
in The University of Michigan
2014

Doctoral Committee:

 Professor Amir Mortazawi, Chair
 Associate Professor Anthony Grbic
 Associate Professor Jerome P. Lynch
 Professor Jamie Dean Phillips

Acknowledgements

Table of Contents

List of Tables

List of Figures

List of Appendices

Abstract

Ferroelectric-on-Silicon Switchable Bulk Acoustic Wave Resonators and Filters for RF Applications

by

Seyit Ahmet Sis

Chair: Amir Mortazawi

Todays' multi-band mobile phones' RF front ends require separate transceivers for each frequency band. Future wireless mobile devices are expected to accommodate a larger number of frequency bands; therefore using the existing transceiver configurations becomes prohibitive. One of the key RF components in wireless devices is the image reject and band-selection filter. Today's multi-band mobile phones use bulk acoustic wave (BAW) filters in conjunction with solid-state or MEMS-based RF switches for selecting the frequency band of operation. This approach results in very complex circuits. As number of frequency bands increases, ferroelectric BST, operating at its paraelectric phase, has recently been utilized in designing intrinsically switchable BAW resonators and filters due to its voltage induced piezoelectricity. The intrinsically switchable BAW resonators and filters are suitable for designing compact multiband and frequency agile transceivers as they can be switched on and off by simply controlling the

dc bias voltage across the ferroelectric layer instead of using separate MEMS or solid-state based RF switches.

In this thesis, composite ferroelectric resonators are studied to improve the Q of intrinsically switchable BAW resonators. Intrinsically switchable BAW resonators with record Q values based on ferroelectric-on-silicon composite structures have been demonstrated. In addition, two types of intrinsically switchable BAW filters using ferroelectric-on-silicon composite structure: electrically connected filters and laterally coupled acoustic filters are studied. In the first part of this thesis, the design, fabrication and measurement results for high-Q composite film bulk acoustic resonators (FBARs) are discussed. Subsequently, an intrinsically switchable electrically connected filter based on ferroelectric-on-silicon composite FBARs is presented. Finally, an intrinsically switchable laterally coupled acoustic filter with a ferroelectric-on-silicon composite structure is presented. The reported laterally coupled acoustic filter represents the first demonstration of a BST based intrinsically switchable acoustically coupled filter.

Chapter 1

Introduction

1.1   Motivation

Multiband and frequency-agile transceivers are ubiquitous in today's communication and radar systems. They are used in various applications including mobile phones and frequency hopping radars. For example, today's smart phones utilize 3G or 4G wireless technologies which provide fast internet connection through multiple cellular frequency bands (850/900/1700/1900/2100/600 MHz). In addition, almost all smart phones have the capability for communicating through various other standards such as wireless area network (WAN) and Bluetooth standards (Wi-Fi 2.4/5GHz, Bluetooth 2.4 GHz), and providing global positioning system service (GPS 1.5 GHz) [1-3].

Currently, in a mobile handset, each of these standards has its own transceiver circuit with separate filters, amplifiers, switches and antennas [2]. A part of a typical RF front-end for a 3G mobile handset is shown in Figure 1.1. Most of the frequency bands of operation shown in Figure 1.1 have been included in mobile phones in the last decade. There is a steady increasing trend in the number of frequency bands used in smart phones.
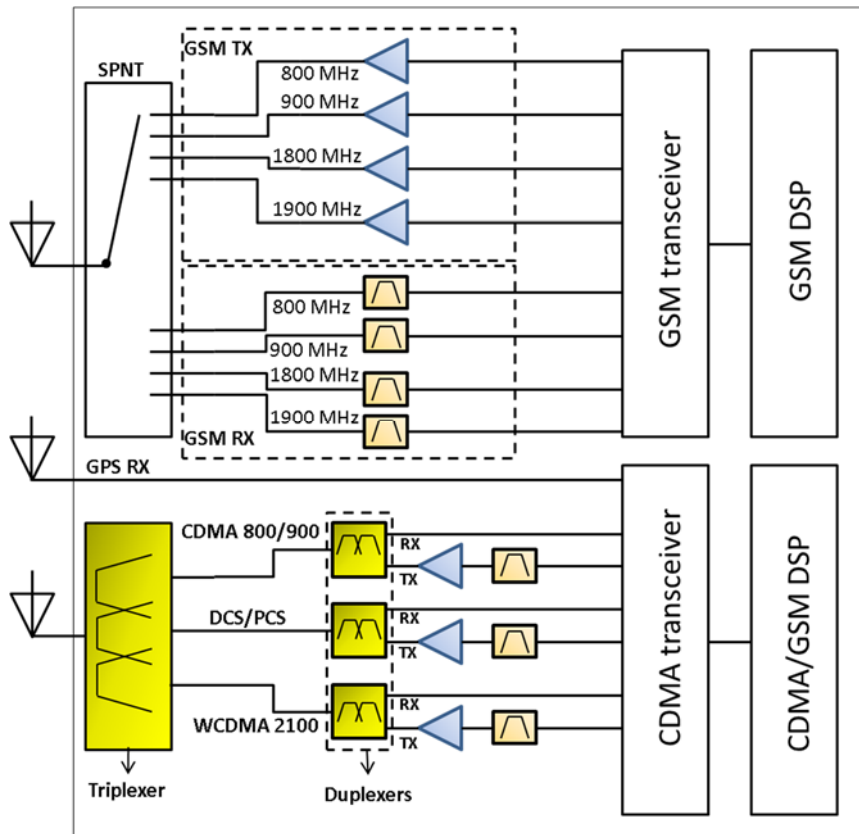
Figure 1.1: Typical mobile phone front-end architecture [1]

Currently, not all the licensed frequency bands are used efficiently [4-10]. To use the frequency spectrum more efficiently, complex radio technologies are required for future communication systems. Cognitive radio is an example of such technologies based on multi-band, frequency-reconfigurable transceivers.

Cognitive radio's basic operation is based on sensing the frequency spectrum, detecting the available frequency bands, and finally reconfiguring its transmission and reception parameters. These parameters include frequency, power level, bandwidth, data rate and transmission mode [4]. The process for cognitive radio's interaction with the communication environment and determination of its transmission and reception parameters is illustrated with the cognitive cycle and shown in Figure 1.2 [4, 9].
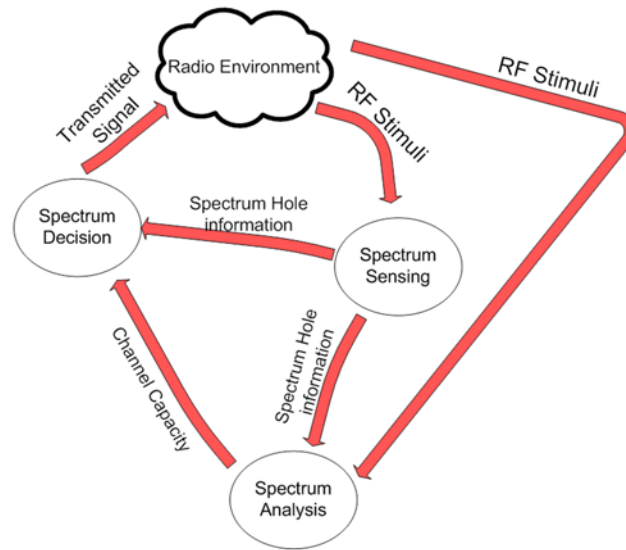
Figure 1.2: Cognitive cycle for a cognitive radio [4]

To operate within a wide range of frequencies, cognitive radios based on traditional transceivers require individual RF front-ends including filters, switches and amplifiers for each frequency band. Traditional transceiver configurations result in complex, bulky and expensive cognitive radios. Therefore, frequency-agile transceivers are needed for compact and low-cost cognitive radios.

One of the key components used in multiband and frequency-agile transceivers are switched filters for the RF band selection. Each filter, operating at a different frequency band, is connected to the signal path through an RF switch as shown in Figure 1.1. RF switches can be based on solid-state or MEMS technologies. In general, switches introduce loss in the signal path and increase the circuit real estate. For example, a two-channel TriQuint's BAW based switched filter bank [11], and a six-channel Herley's switched filter bank based on printed filters [12] are shown in Figure 1.3. The RF switches as well as the transmission lines connecting the input and output of the TriQuint's compact BAW filters to switches occupy a significant portion of the overall

circuit area as can be seen in Figure 1.3 (a). The insertion loss of individual TriQuint filters in switched filter bank is 1.5 dB; however, the insertion loss increases to approximately 2.5 dB when these filters are connected to p-HEMT based solid state switches [11]. Similarly, the insertion loss of the Herley's filters is larger than 6 dB in all six channels as shown in Figure 1.3 (b) [12]. A significant part of this loss can be attributed to RF losses due to switches and interconnects.

No.	Freq. Range (GHz)	Ins. Loss (dB)	Stop Band 55 dBc (GHz)	Stop Band 70 dBc (GHz)
1	5.5 to 7.9	6.0	2.0 to 4.3	9.2 to 19.0
2	7.7 to 10.0	6.8	2.0 to 6.2	11.3 to 19.0
3	9.6 to 12.0	6.8	2.0 to 8.2	13.3 to 19.0
4	11.7 to 14.0	6.5	2.0 to 10.5	15.5 to 19.0
5	13.7 to 15.7	6.5	2.0 to 12.0	17.0 to 19.0
6	15.6 to 17.8	6.5	2.0 to 13.5	@ 19.0

(a)　　　　　　　　　　　　　(b)
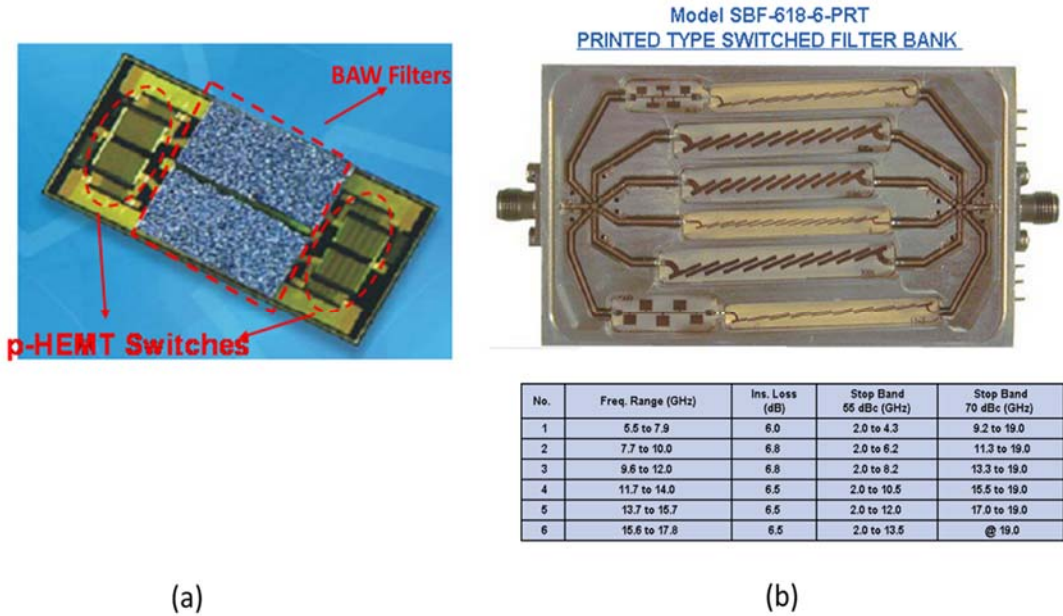
Figure 1.3: (a) Two-channel TriQuint's switched filter bank based on BAW filters [11], (b) six-channel Herley's switched filter bank based on printed filters [12]

To design compact and low-cost multiband and frequency-agile systems, there is a need for an innovative approach to simplify the transceiver's configuration. New technologies and methods are required to design switched filters in multiband and frequency-agile systems. One solution would be to utilize tunable filters and amplifiers which can cover the entire frequency bands used in the system, making a fully-tunable RF front-end. However, this may not be practical due to the difficulty of implementing

very wide frequency range tunable RF filters which meet the required performance across the entire frequency range. Instead, an alternative solution would be to combine tunable amplifiers, tunable antennas and compact switched filters based on new technologies. To design very compact switched filters, several technologies and methods, including ferroelectric based intrinsically switchable bulk acoustic wave (BAW) resonators and DC voltage switchable silicon micro-resonators have been proposed.

Barium strontium titanate ($Ba_{(x)}$ $Sr_{(1-x)}$ TiO_3, BST) based intrinsically switchable resonators and filters have already been successfully demonstrated [13-30]. The underlying principle of the switching mechanism in these devices is the strong electrostrictive effect in ferroelectric BST material. The electrostrictive effect causes induced piezoelectricity with the application of an electric field, resulting in electric field induced (or voltage induced) piezoelectricity. Voltage induced piezoelectricity is ultimately used to switch the electromechanical transduction on & off within the BAW resonators and filters allowing the design of intrinsically switchable BAW devices. Electrostriction and voltage induced piezoelectricity will be discussed with detail in Section 1.2.

Along with its voltage induced piezoelectric effect, BST exhibits voltage tunable permittivity. This property has also been utilized in designing various components such as tunable filters, tunable amplifiers, tunable antennas, phase shifters, tunable matching circuits, and voltage-controlled oscillators (VCO) [31-45]. BST's inherent voltage tunable permittivity and voltage induced piezoelectric effect can be utilized to implement compact RF front-ends that are suitable for complex multiband and frequency agile

systems [3]. Figure 1.4 shows a proposed compact mobile phone front-end architecture utilizing switchable and tunable BST based RF components.

The aim of this work is to improve the quality factor (Q) and fabrication yield of BST based intrinsically switchable BAW resonators for both filter and oscillator applications. A composite structure has been implemented, which has already been successfully applied to the design of AlN and ZnO based BAW resonators [46-50]. The improvement in the quality factor and mechanical strength of the resonators is achieved through fabrication of BST-on-silicon composite structures which will be detailed in Chapter 2. Using this composite structure, intrinsically switchable electrically connected and acoustically coupled filters are also designed, fabricated and characterized and will be discussed throughout this dissertation.
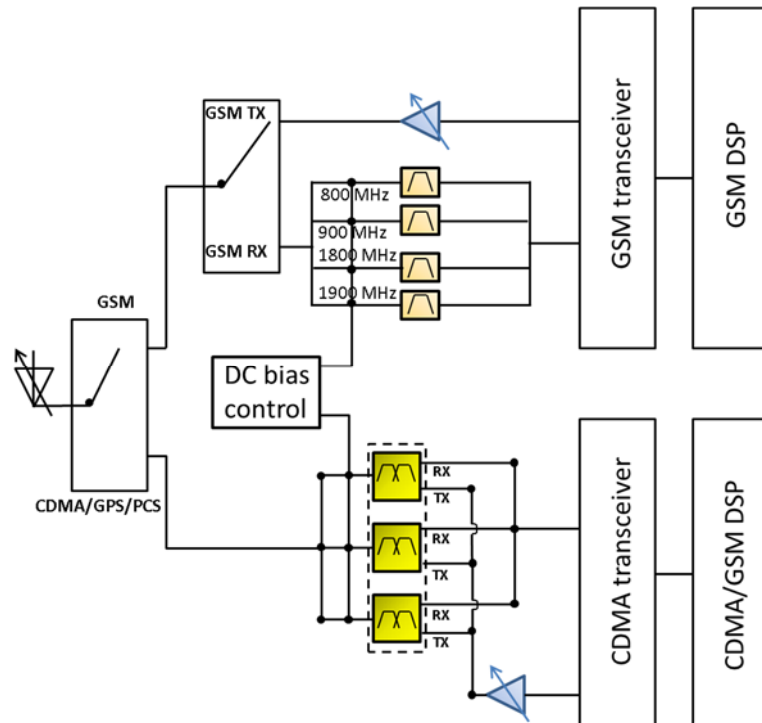
Figure 1.4: Compact RF front-end for mobile phones based on BST based tunable and switchable components

1.2 An Overview of Acoustic Resonator Technologies in RF Applications

Mechanical resonators exhibit the largest displacement at their natural frequency of vibration (acoustic resonance frequency). There are multiple resonance modes for a given 3-D structure. For example, a simple rectangular 3-D structure has thickness-extensional, width-length extensional, shear and lamb wave modes, each one having a different displacement shape. Furthermore, each of these modes may exhibit higher order modes, called "harmonics" or "overtones". In many applications, these resonance modes are intentionally avoided for various reasons. For example, in civil engineering, resonance modes in tall buildings or bridges are avoided or damped. On the other hand, there are applications that are based on acoustic resonance phenomena, such as musical instruments, clocks, sensors, and electric circuits.

In electric circuits, acoustic resonators are utilized to obtain a high-Q electrical resonance response for designing filters and low phase noise oscillators. The resonance frequency of them is determined by their geometry and inversely related to their size. Advancement in micro-fabrication techniques have allowed designers to reduce resonator's size that are suitable for operating at RF & microwave frequencies, allowing the RF filters, and low-phase-noise oscillators to employ acoustic resonators. For example, crystals made with bulk quartz piezoelectric plates operating in the MHz range have been available in electric circuit applications since the 1930s. On the other hand, thin film based bulk acoustic wave (BAW) resonators operating in the GHz range have only recently been used in commercial applications due to advancement in fabrication techniques [51].

To achieve electric resonance response in acoustic resonators, an electromechanical transduction mechanism is needed to couple electric signal to acoustic energy. In RF applications, the most common transduction mechanisms are electrostatic (capacitive) and piezoelectric transduction [52]. Recently, the electrostrictive transduction mechanism was utilized for designing intrinsically switchable resonators and filters for RF applications. This thesis discusses intrinsically switchable composite FBARs and filters utilizing electrostrictive transduction. The following sections discuss these transduction mechanisms in detail.

1.2.1 Acoustic Resonators Using Electrostatic Transduction

The electrostatic (capacitive) transduction principle is based on the electrostatic force between charges. Two charged electrodes, separated by a distance of d having an overlapping area of A, experience an electrostatic force ($F_{electrostatic}$) [53]:

$$F_{electrostatic} = \frac{Q_{charge}^2}{2\varepsilon_0 \varepsilon_r A} \tag{1.1}$$

where ε_0, ε_r and A are permittivity of air, relative permitivity of the medium between two electrodes and overlapped area of the electrodes, respectively. The Q_{charge} is the total electric charges at the plates and is a function of the applied voltage (V) and the parallel capacitance (C_0). The C_0 can be calculates using (1.2).

$$C_0 = \frac{\varepsilon_0 \varepsilon_r A}{d} \tag{1.2}$$

To illustrate the operation of electrostatically transduced resonators, the schematics for a one port and a two port clamped-clamped beam micro-resonators are shown in Figure 1.5 (a) and Figure 1.5 (b), respectively. These schematics can be used to understand the

operating principle of other electrostatically transduced resonators as well, such as clamped-free and disk resonators. As seen in Figure 1.5, the electrostatically transduced resonators consist of one or more parallel plate capacitors. At least one of the electrodes is connected to a mechanical structure which is designed for a certain mode of vibration at a desired resonance frequency. When an RF signal is applied at the resonance frequency, the structure (e.g. beam) exhibits a large displacement. Due to the significant change in the capacitance caused by this displacement, a large motional current is induced at the electrodes, providing a rapid impedance variation and a high-Q electrical resonance response at the device resonance frequency.

A DC bias voltage, called "polarization voltage (V_P)", is needed for electrostatic transduction [54-63] (Figure 1.5). This can be attributed to the fact that the electrostatic force ($F_{electrostatic}$) between electrodes is always attractive regardless of the applied signal's polarity as shown in (1.1) [62]. The electrostatically transduced beam resonators, shown in Figure 1.5, utilize either fundamental or higher order flexural modes [52]. Figure 1.7 illustrates the flexural vibrating modes of a beam for the fundamental and the 5th resonance modes. The resonance frequency of a beam resonator operating at its nth resonance mode is calculated using (1.3) [52, 58]:

$$f_n = \frac{\lambda_n^2}{2\pi\sqrt{12}}\left(\frac{W}{L^2}\right)\sqrt{\frac{E}{\rho}} \tag{1.3}$$

where W, L, E and ρ are width, length, Young's modulus and the density of the beam, respectively. In (1.3), the λ_n can be calculated using (1.4) [52, 58].

$$\cos\lambda_n \cdot \cosh\lambda_n = 1. \tag{1.4}$$

Figure 1.6 shows the schematic and scanning electron microscope (SEM) pictures for reported beam resonators [58]. The SEM pictures on the bottom left and bottom right in Figure 1.6 show fabricated clamped-clamped and clamped-free beam resonator, respectively [58]. In [58], the authors utilize polysilicon as the electrodes making an all-Si micro-resonator. Qs as high as 177000 at 19 kHz, and 74000 at 80 kHz are reported for clamped-free and clamped-clamped beam resonators, respectively [58].
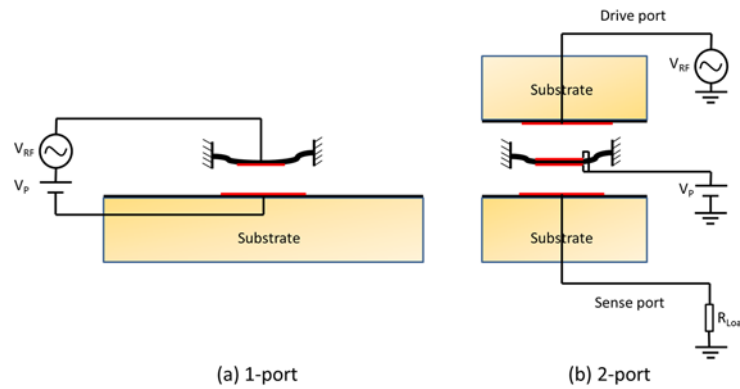
Figure 1.5: Schematics for (a) a one-port and (b) a two-port electrostatically transduced clamped-clamped beam resonators
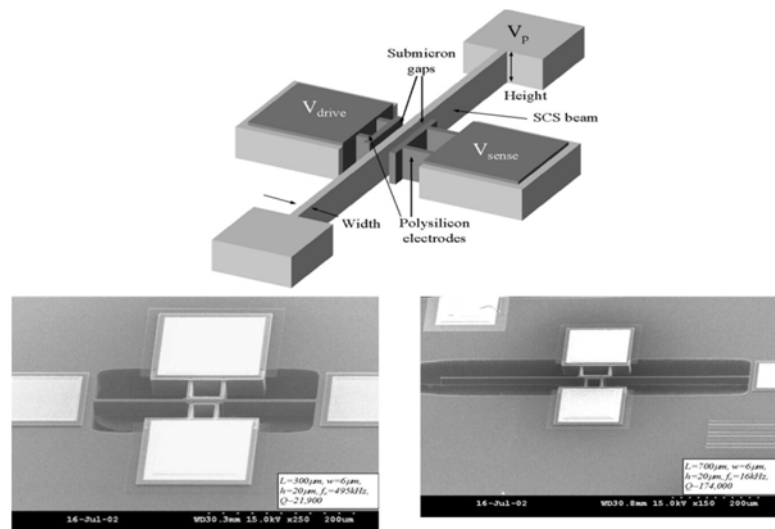
Figure 1.6: Electrostatically transduced beam resonators [58]. Top picture is the schematic, bottom left and right pictures are the SEM photos for fabricated clamped-clamped and clamped-free resonators [58].

10
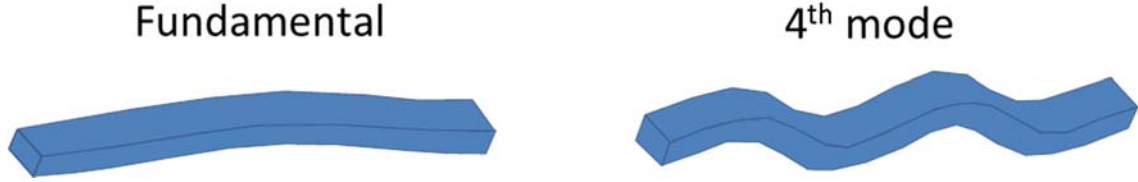
Figure 1.7: The fundamental and the 4th order flexural mode shapes of a beam structure.

The electrostatically transduced beam resonators discussed above operate at low frequencies, usually less than 100 MHz. Higher resonance frequencies can be obtained in electrostatically transduced resonators utilizing bulk modes as compared to resonators based on flexural modes [52]. This is attributed to the fact that the resonators based on bulk modes exhibit larger mechanical stiffness [52]. Figure 1.8 shows a reported silicon bulk acoustic wave resonator (SiBAR) utilizing a long and thick bulk-micromachined resonating block [59, 60]. The middle picture in Figure 1.8 shows the modal shape at the fundamental resonance mode [59, 60]. The structure vibrates in width-extensional mode and exhibits a displacement node at the center of the width (W). The resonating block is connected to the substrate at this node for the highest resonator performance. The resonance frequency of a SiBAR operating at its nth resonance mode is calculated using (1.5) [59, 60]

$$f_n = \frac{n}{2W} \sqrt{\frac{E}{\rho}} \tag{1.5}$$

where W, E, and ρ are width, Young's modulus and the density of the bulk resonating block shown in Figure 1.8, respectively. In [59, 60], the reported resonance frequencies vary from 85.9 MHz to 1.55 GHz for various devices and mode numbers. In these devices, Qs as high as 24400 are reported [59, 60].
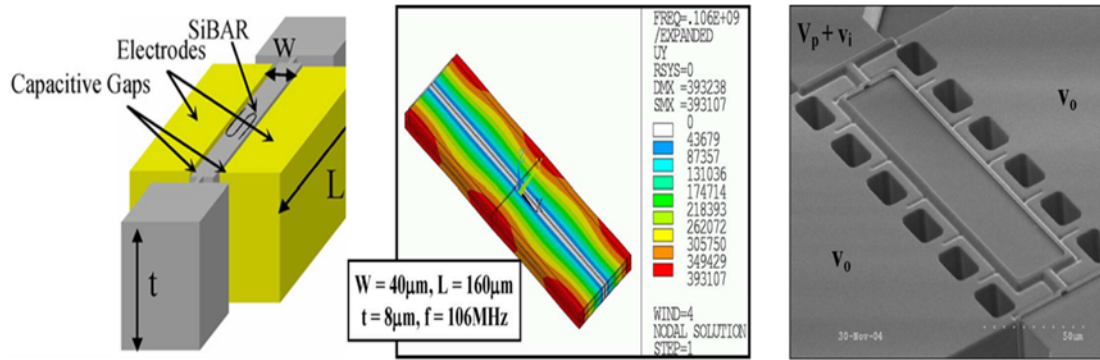
Figure 1.8: The schematic, a fundamental mode shape and a fabricated device for a SiBAR are shown from left to right, respectively [59, 60].

Figure 1.9 shows another example of an electrostatically transduced bulk acoustic resonator [56]. The resonating bulk structure in this device is a polysilicon disk vibrating at its wine glass mode shape. To turn the electromechanical transduction on, the device is biased at the input and output electrodes [56]. The reported resonance frequency and Q for this device are 1.156 GHz and 2689, respectively [56].

Schematic and 2-port measurement configuration   Wine glass mode shape
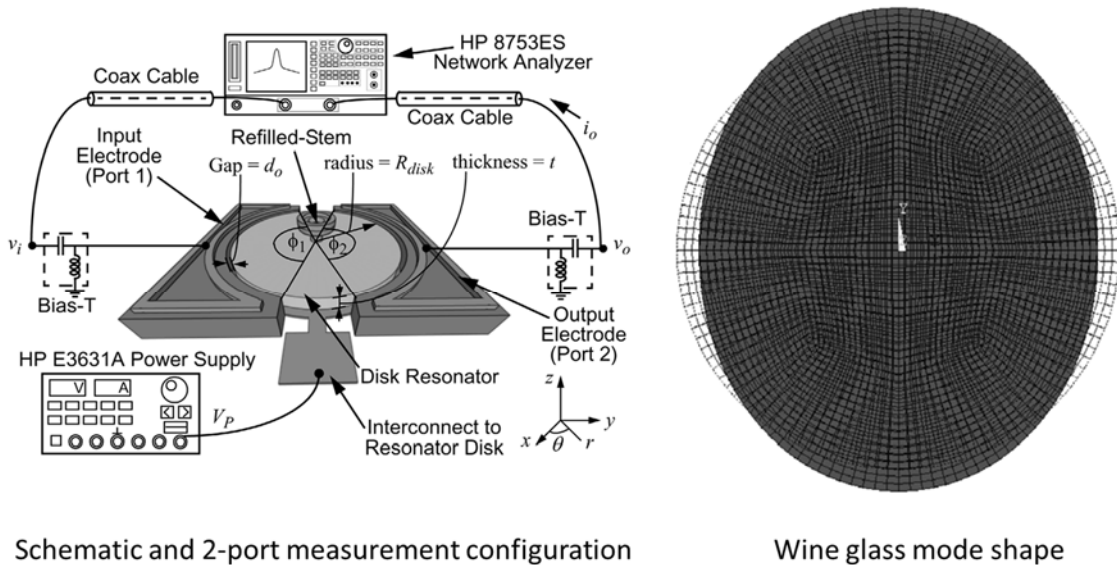
Figure 1.9: The schematic and a wine glass mode shape for an electrostatically transduced bulk acoustic resonator [56].

As shown in the reported devices discussed above, electrostatic transduction mechanism requires a DC bias voltage (V_p) for turning the electromechanical transduction on. This requirement makes electrostatically transduced resonators attractive for wireless applications, as it provides a voltage dependent switching functionality [52]. Furthermore, resonance frequency can be tuned slightly by changing the V_p, through the voltage induced stiffness effect [58]. This can be used to fine tune the resonator for compensating the frequency shift caused by fabrication tolerances and temperature change [58].

Electrostatically transduced resonators exhibit very-high quality factors (Qs) as compared to other technologies. This is attributed to the fact that the transducer has no physical contact with the resonating structure [52]. However, the same fact causes high motional resistance in these resonators, unless the gap between electrodes is very small [52]. High motional resistance is a significant drawback of these resonators for use in RF systems that consist of 50 Ω matched blocks.

1.2.2   Acoustic Resonators Using Piezoelectric Transduction

Most of the acoustic resonators used in RF systems are based on piezoelectric transduction mechanism. This section discusses various piezoelectrically transduced acoustic resonators. To better explain the function of these devices, a brief discussion of the piezoelectricity phenomenon is provided first.

1.2.2.1   Piezoelectricity

Piezoelectricity is a physical property that causes strong polarization and charge accumulation in certain classes of crystals, ceramics and various other solids when an

external mechanical stress is applied. This physical property is also reversible; an electric field or voltage applied to these materials creates an internal stress that causes a displacement in the material's 3-D structure. This reverse effect is called inverse-piezoelectricity. Piezoelectricity was experimentally verified by Jacques and Pierre Curie brothers in France using a quartz plate [64, 65]. A year later, inverse piezoelectricity was demonstrated by another French physicist, Gabriel Libmann. Since then, the piezoelectric phenomenon has been utilized in many applications. With the discovery of new piezoelectric materials and advanced fabrication techniques, high quality, low-cost piezoelectric materials have become ubiquitous in everyday life. The market value for piezoelectric devices is more than US$10 billion annually [66].

Piezoelectric materials exhibit an asymmetry in their crystalline structure [67], and can be classified as polar and non-polar piezoelectrics [68]. Polar piezoelectrics exhibit a spontaneous polarization (P_s) even without an applied mechanical stress. An applied mechanical stress changes the magnitude and direction of the existing polarization in the material. To ensure the piezoelectric response or to improve the piezoelectric effect in polar piezoelectrics, spontaneous polarization is aligned in a certain direction by applying a large electric field at elevated temperatures. This process is called Corona charging [64]. On the other hand, non-polar piezoelectrics do not exhibit spontaneous polarization; applied mechanical stress creates a non-zero electric polarization in the material.

In piezoelectric materials, the mechanical and electrical properties are coupled through the electric polarization vector (P). This can be explained by first discussing the electric field induced polarization in a simple dielectric material. In a dielectric medium, the electric displacement vector (D) is given by [69]:

14

$$D = \varepsilon_0 E + P \tag{1.6}$$

where ε_0, E and P are the permittivity of air, electric field and electric field induced polarization, respectively. P is related to the electric field (E) through susceptibility (χ) as shown in (1.7). By plugging (1.7) into (1.6), D can be expressed as shown in (1.8)

$$P = \varepsilon_0 \chi E \tag{1.7}$$

$$D = \varepsilon_0 E + \varepsilon_0 \chi E = \varepsilon_0 (1 + \chi) E = \varepsilon_0 (\varepsilon_r) E \tag{1.8}$$

where ε_r is the relative permittivity for the dielectric layer. If the dielectric material exhibits piezoelectricity, an electric polarization is created by the applied external stress given by [69]:

$$P_{piezo} = dT \tag{1.9}$$

where P_{piezo}, d and T are the electric polarization caused by external stress, the piezoelectric strain coefficient, and external stress, respectively. In this case, electric displacement has two polarization components: electric field induced polarization (P) and strain induced polarization (P_{piezo}). Then, (1.6) and (1.8) are rewritten as:

$$D = \varepsilon_0 E + P + P_{piezo} = \varepsilon_0 (\varepsilon_r) E + dT. \tag{1.10}$$

Equation (1.10) represents the direct piezoelectric effect. The inverse piezoelectric effect can also be derived similarly starting from Hooke's law and relating the stress or strain to applied electric polarization. Direct and inverse piezoelectric equations together constitute the coupled piezoelectric equations shown below (1.11) [69].

$$\begin{aligned} D &= \varepsilon^T E + dT \\ S &= s^E T + dE \end{aligned} \tag{1.11}$$

In (1.11), S represents the mechanical strain. The superscripts T and E in (1.11) indicate that the permittivity (ε) and the compliance (s) matrices are for constant stress and electric field conditions. Equations (1.11) are called "coupled piezoelectric equations", and can be expressed in various other forms depending on the electric (D or E) and mechanical variables (S or T). These alternative equations, given IEEE's piezoelectricity standard publication, are shown in (1.12) - (1.14) [70].

$$E = -gT + \beta^T D$$
$$S = s^D T + gD$$
(1.12)

$$E = -h\,S + \beta^S D$$
$$T = c^D S - hD$$
(1.13)

$$D = eS + \varepsilon^S E$$
$$T = c^E S - eE$$
(1.14)

In (1.11)-(1.14), d, g, h, and e are the piezoelectric strain coefficient, the piezoelectric voltage coefficient, the piezoelectric stress coefficient, and the piezoelectric charge coefficient, respectively. In (1.12) and (1.13), β is impermitivity of the material which is defined as $\beta=(\varepsilon)^{-1}$. The piezoelectric coefficients above can be converted from one to another using suitable equations [70].

Piezoelectric materials are anisotropic due to their usually single-crystalline or highly-crystalline structures; therefore piezoelectric coupled equations shown in (1.11)-(1.14) are expressed in matrix form. (1.15) shows the matrix form of the coupled equation given in (1.11).

$$
\begin{bmatrix} S_1 \\ S_2 \\ S_3 \\ S_4 \\ S_5 \\ S_6 \end{bmatrix} = \begin{bmatrix} s_{11} & s_{12} & s_{13} & s_{14} & s_{15} & s_{16} \\ s_{21} & s_{22} & s_{23} & s_{24} & s_{25} & s_{26} \\ s_{31} & s_{32} & s_{33} & s_{34} & s_{35} & s_{36} \\ s_{41} & s_{42} & s_{43} & s_{44} & s_{45} & s_{46} \\ s_{51} & s_{52} & s_{53} & s_{54} & s_{55} & s_{56} \\ s_{61} & s_{62} & s_{63} & s_{64} & s_{65} & s_{66} \end{bmatrix} \cdot \begin{bmatrix} T_1 \\ T_2 \\ T_3 \\ T_4 \\ T_5 \\ T_6 \end{bmatrix} + \begin{bmatrix} d_{11} & d_{12} & d_{13} \\ d_{21} & d_{22} & d_{23} \\ d_{31} & d_{32} & d_{33} \\ d_{41} & d_{42} & d_{43} \\ d_{51} & d_{52} & d_{53} \\ d_{61} & d_{62} & d_{63} \end{bmatrix} \cdot \begin{bmatrix} E_1 \\ E_2 \\ E_3 \end{bmatrix}
$$

$$
\begin{bmatrix} D_1 \\ D_2 \\ D_3 \end{bmatrix} = \begin{bmatrix} d_{11} & d_{12} & d_{13} & d_{14} & d_{15} & d_{16} \\ d_{11} & d_{22} & d_{23} & d_{24} & d_{25} & d_{26} \\ d_{31} & d_{32} & d_{33} & d_{34} & d_{35} & d_{36} \end{bmatrix} \cdot \begin{bmatrix} T_1 \\ T_2 \\ T_3 \\ T_4 \\ T_5 \\ T_6 \end{bmatrix} + \begin{bmatrix} \varepsilon_{11} & \varepsilon_{12} & \varepsilon_{13} \\ \varepsilon_{21} & \varepsilon_{22} & \varepsilon_{23} \\ \varepsilon_{31} & \varepsilon_{32} & \varepsilon_{33} \end{bmatrix} \cdot \begin{bmatrix} E_1 \\ E_2 \\ E_3 \end{bmatrix}
$$

(1.15)

Most common piezoelectric materials for use in RF acoustic resonators are aluminum nitride (AlN), zinc oxide (ZnO), lead zirconium titatane (PZT) and lithium niobate (LiNbO$_3$). These piezoelectric materials are either utilized as bulk substrates or fabricated as thin film layers on substrates using various deposition techniques. Common deposition techniques include sputtering, epitaxial growth, sol-gel, chemical vapor deposition (CVD) and pulsed laser deposition [3, 52, 64]. Usually, it is difficult to obtain the same property and performance of the bulk materials is difficult [64]. Therefore, several researchers have experimented with fabricating thin films by thinning the bulk piezoelectric materials. Piezoelectric layers as thin as 5 μm is obtained by thinning bulk piezoelectric substrates [64].

Piezoelectrically transduced acoustic resonators are based on acoustic waves propagating either at the surface or in the bulk of the resonator structure. The following two subsections discuss piezoelectrically transduced surface acoustic wave and bulk acoustic wave resonators.

1.2.2.2   Surface Acoustic Wave (SAW) Resonators

Surface acoustic wave (SAW) resonators consisting of input and output interdigitated electrodes (IDT) on a piezoelectric substrate are shown in Figure 1.10. An RF signal excited at the input IDT excites surface acoustic waves on the surface of the material via the inverse piezoelectric effect. The acoustic waves propagate to the output IDT and are converted back to electric signals via the direct piezoelectric effect. The reflectors shown in Figure 1.10 are used to confine the acoustic waves by creating an acoustic cavity. In SAW resonators, typically more than 90% of the acoustic energy propagates within one wavelength thickness from the substrate's top surface [71].
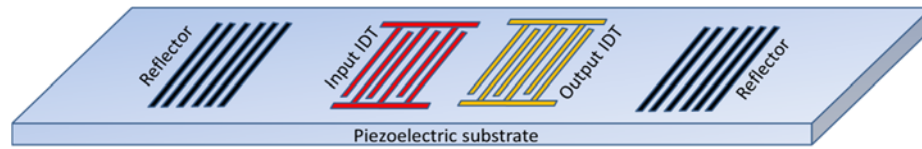
Figure 1.10**:** A typical structure for surface acoustic wave resonator (SAW)

The SAW resonators are fabricated on piezoelectric substrates rather than thin film piezoelectric layers. Most of the acoustic energy stays on the surface of the piezoelectric layer and their resonance frequency is independent of the piezoelectric layer's thickness. Therefore, SAW fabrication is simpler as compared to that of bulk acoustic wave (BAW) resonators, as the SAW fabrication process avoids the complexity and the cost associated with high temperature piezoelectric deposition. The resonance frequency of the SAW resonators is determined by the spacing between fingers in IDT as follows:

$$f = \frac{v}{\lambda} \tag{1.16}$$

where v and λ are the acoustic wave velocity and the periodic distance between fingers. Therefore, multiple frequency SAW resonators and filters can be easily fabricated on the same substrate by simply changing the lateral geometry of the devices for operating at different frequencies. However, their maximum achievable resonance frequency is limited by the minimum feature size of the lithography process. Commercial SAW resonators are available at frequencies up to 2.5 GHz. SAW resonators up to 14 GHz are demonstrated using advanced e-beam lithography techniques [72].

1.2.2.3   Bulk Acoustic Wave (BAW) Resonators

Piezoelectrically transduced bulk acoustic wave (BAW) resonators are based on acoustic wave propagation in the bulk of the resonator structure. Common examples are thin film bulk acoustic resonators (FBARs), solidly mounted resonators (SMRs) and contour (lateral) mode resonators. This thesis discusses FBARs, composite FBARs, and SMRs in detail in Chapter 2. Therefore, in this section, the structure and operating principle of these devices are briefly explained. An example device for a recent approach for FBARs with symmetric composite structure is briefly discussed here [46]. A more detailed explanation on piezoelectrically transduced contour mode resonators is also provided in this section.

The FBARs and SMRs are acoustic cavities consisting of a piezoelectric layer sandwiched between the top and bottom electrodes. The acoustic wave is confined within the piezoelectric layer and electrodes by the reflective boundaries at the top and bottom surfaces. In FBARs, the reflective boundaries are created by the air interface with the top and bottom surfaces. In SMRs, a Bragg reflector is utilized to reflect the acoustic waves.

As in FBARs and SMRs, composite FBARs are also acoustic cavities consisting of a piezoelectric layer sandwiched between top and bottom electrodes. However, composite FBARs employ additional non-piezoelectric, low-loss layer acting as a membrane under the sandwiched piezoelectric layer, as compared to FBARs and SMRs. Composite FBARs exhibit larger Q values and operate at higher order modes. Figure 1.11 shows the typical FBAR (a), SMR (b) and composite FBAR (c) structures and acoustic mode shape for an FBAR operating at the fundamental mode (d). For FBARs and SMRs, Qs as high as 3000, are reported. For the composite FBARs, a Q of 68000 is reported [47].

Composite FBARs shown in Figure 1.11 (c) are asymmetric along the horizontal line at the middle of the piezoelectric layer (transduction layer). Therefore, they exhibit both even and odd resonance modes as opposed to FBARs and SMRs which excite only odd resonance modes [48]. A recently reported method for the design of composite FBARs is based on creating a symmetric structure by depositing a low-loss, non-piezoelectric layer at both the top and the bottom of the piezoelectric layer. Figure 1.12 shows a reported AlN/SiO2 symmetric composite FBAR [46]. The device exhibits its strongest resonance response at the 3rd resonance mode with a Q and an effective electromechanical coupling coefficient (K_t^2) of 1450 and 0.005, respectively. Quality factor values as high as 2000 have been reported at other resonance modes [46].
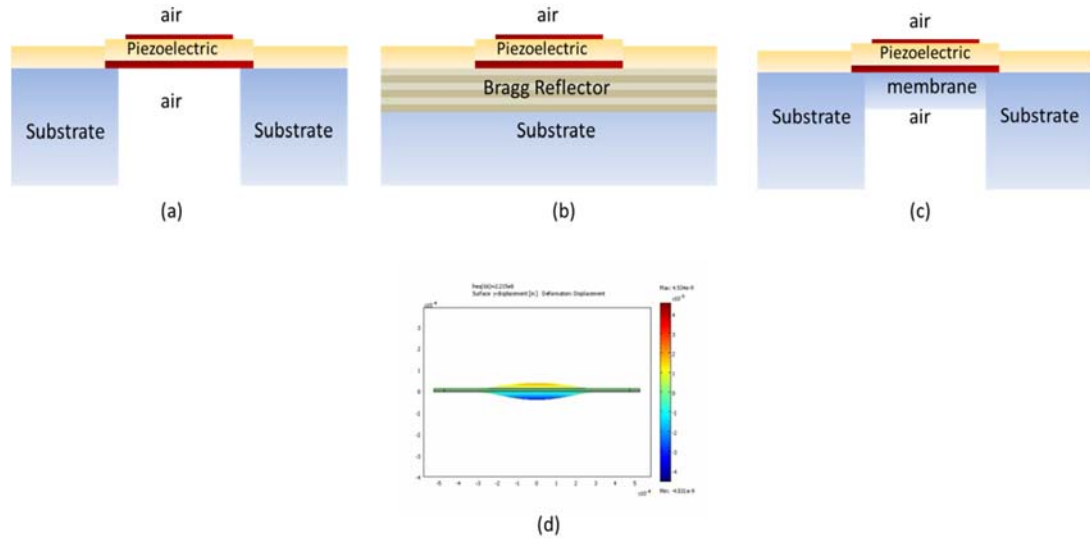
Figure 1.11: Typical 2-D structures for (a) FBARs, (b) SMRs, (c) composite FBARs. A mode shape for an FBAR at fundamental resonance mode is shown in (c)
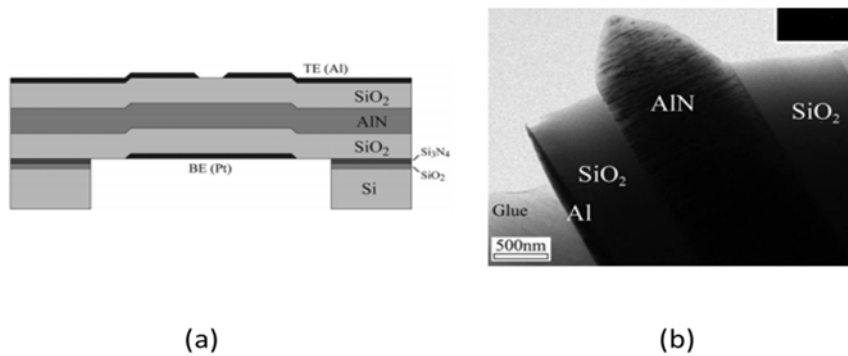
Figure 1.12: Symmetric composite FBAR's (a) schematic, (b) TEM picture [46].

FBARs and SMRs discussed above are thickness-extensional mode resonators. In these resonators, the resonance frequency is set by the resonator's overall thickness. Electrical response and resonance frequencies of these resonators can be obtained by using a 1-D acoustic transmission line model.

Another commonly used piezoelectrically transduced BAW resonator is a contour mode (Lateral mode) resonator. Contour mode resonators can operate at their width-

extensional, length-extensional and radial-extensional resonance modes depending on the resonance structure. Their resonance frequency is mainly determined by the lateral dimension of the resonator, as in SAW devices. Therefore, the maximum achievable resonance frequency is limited by minimum feature size achievable by the lithography process. Contour mode resonators operating at different frequencies can be easily fabricated on the same substrate.

As in FBARs, contour mode resonators consist of a piezoelectric layer sandwiched between top and bottom electrodes. RF signal at the electrodes excite lateral displacement in the structure through d_{31} piezoelectric coefficient. Contour mode resonators are connected to substrates through anchors as shown in Figure 1.14. It should be noted that contour mode resonators are released from the substrate at both the bottom and sides of the resonator. The anchors are connected to the resonator at the displacement nodes of the resonance mode. Anchors provide the only connection to the substrate in contour mode resonators.

Figure 1.13 shows the modes shapes for a radially-extensional ring shape and a length-extensional rectangular shape contour mode resonators. Figure 1.14 shows the scanning electron microscope (SEM) pictures for a reported radially-extensional ring shape and length-extensional rectangular shape contour mode resonators demonstrated in [73]. In [73], devices with resonance frequencies varying from 19 MHz to 656 MHz, with Qs as high as 4300 have been reported.

(a)   (b)
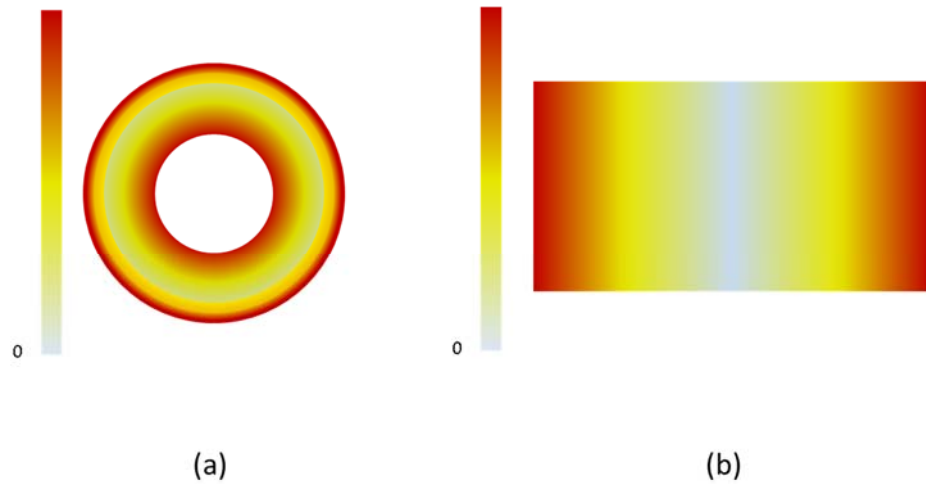
Figure 1.13: Mode shape for the (a) radially-extensional ring shape and (b) length-extensional rectangular shape contour mode resonators

(a)   (b)
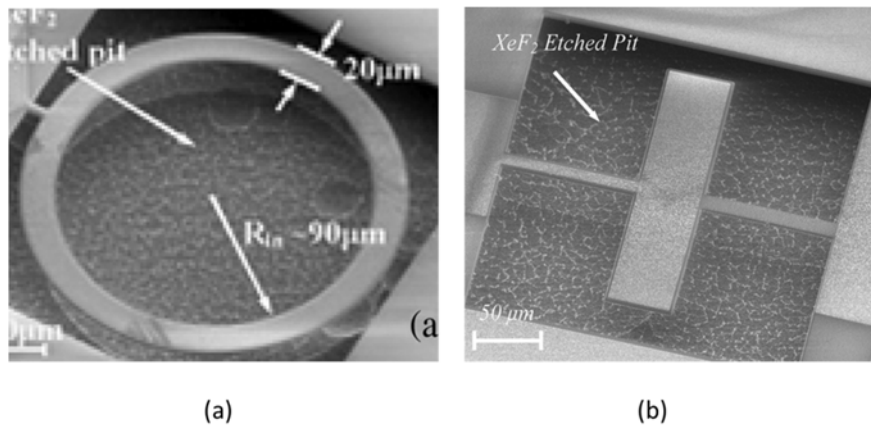
Figure 1.14: SEM pictures for a reported (a) radially-extensional ring shape and (b) length-extensional rectangular shape contour mode resonators [73].

To increase their resonance frequency, higher-order contour mode resonators are demonstrated by using inter-digitated electrode configurations [74]. Resonators operating up to 4.5 GHz, and Qs as high as 520 are reported [74].

1.2.3 Acoustic Resonators Using Electrostrictive Transduction

Electrostriction is a common property observed in all dielectrics causing mechanical stress or strain when an electric field is applied across the dielectric. In most of the dielectric materials, the strain created by an applied electric field is very small for use in any practical applications. In certain dielectrics, such as ferroelectrics, the electrostrictive effect is large enough such that it can create an electric field (or voltage) induced and controlled piezoelectricity. This thesis discusses several intrinsically switchable bulk acoustic wave (BAW) resonators and filters based on electrostrictive transduction mechanism. In these resonators and fiters, ferroelectric barium strontium titane ($Ba_{(x)} Sr_{(1-x)} TiO_3$ or BST) is used for electromechanical transduction due to its strong electrostrictive effect.

As compared to BST's hysteresis behavior and voltage tunable permittivity, BST's voltage induced piezoelectricity is relatively new in circuit applications. For example, BST's hysteresis behavior has already been used in non-volatile memories [75-77]. Similarly, BST's voltage tunable permittivity has been utilized to design varactors in frequency tunable circuits for a long time. Therefore, BST's dielectric properties are well-characterized. For this reason, to better explain electrostriction and voltage induced piezoelectric effect in the following sections, the BST's ferroelectric and voltage tunable permittivity are discussed first. Subsequently, electrostrictive effect and voltage induced piezoelectricity are discussed along with several recently reported switchable BAW resonators based on electrostrictive transduction.

1.2.3.1   Ferroelectricity and Voltage Tunable Permittivity in BST

Ferroelectric materials are non-linear dielectrics; their electric polarization exhibits a non-linear dependency to applied electric field as shown in Figure 1.15 (a). At the same time, ferroelectrics exhibit a hysteresis behavior due to the spontaneous polarization (Figure 1.15). These properties make ferroelectrics quite different from linear dielectrics. Figure 1.15 (b) shows typical electric polarization as a function of electric field in linear dielectrics.

(a) Polarization in ferroelectrics   (b) Polarization in linear dielectrics
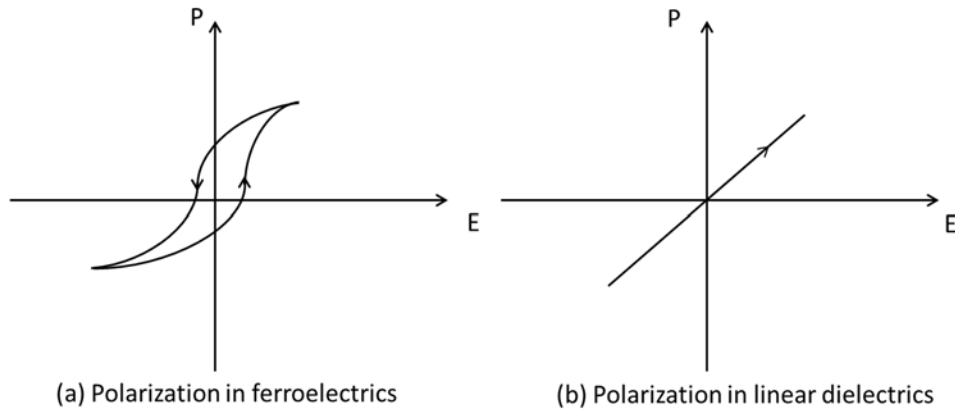
Figure 1.15: Electric polarization as a function of applied electric field (a) in ferroelectrics, (b) in linear dielectrics.

In ferroelectrics, the non-linear electric field dependent polarization provides voltage tunable permittivity as can be seen in expressions (1.7) and (1.8). This property is useful for designing frequency tunable RF circuits and components. To avoid the hysteresis effect and at the same time to maintain the non-linear polarization, one needs to use the ferroelectric materials at their paraelectric phase above the Curie temperature [78]. This is because ferroelectrics do not exhibit spontaneous polarization at the paraelectric phase. The Curie temperature for barium strontium titanate (BST) can be determined by the ratio of barium and strontium atoms in BST's stoichiometry ($Ba_{(x)}$ $Sr_{(1-x)}$ TiO_3). For example,

for barium titanate (BaTiO$_3$) where x is 1 in the stoichiometry, the Curie temperature is approximately 116 ºC [78]. When x is reduced to 0.3 by adding Sr atoms, the stoichiometry of BST becomes Ba$_{(0.3)}$Sr$_{(0.7)}$TiO$_3$, and the Curie temperature is reduced to approximately -110 ºC [78]. Therefore, by manipulating the BST's stoichiometry, one can ensure operating at paraelectric phase with no hysteresis effect. BST in the paraelectric phase has a typical polarization-electric field relation as shown in Figure 1.16.
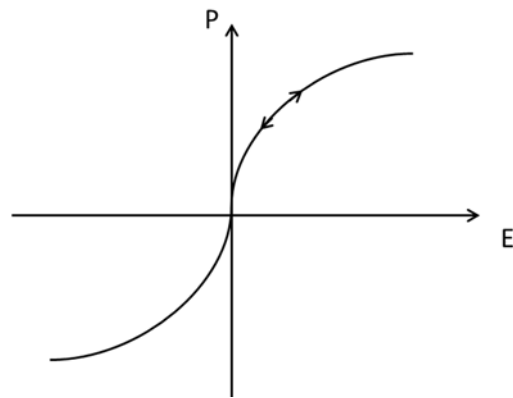
Figure 1.16: Electric polarization vs applied electric field at paraelectric phase

BST's non-linear polarization behavior that provides voltage tunable permittivity can be explained by its paraelectric phase crystal structure as shown in Figure 1.17. BST has a cubic perovskite unit cell structure in which titanium (Ti) atom is located at the center of the structure. The Ti atom exhibits large displacement with the applied RF electric field [78]. The amount of displacement is the largest when Ti is at the center of the structure; therefore, in this case, BST exhibits highest permittivity due to its large electric polarization. When a DC bias is applied along with an RF electric field, the Ti atom is shifted from its center point and exhibit smaller displacement as compared to the unbiased condition. Therefore, the permittivity is reduced due to smaller electric

26

polarization. This is illustrated with arrows across the Ti atom in Figure 1.17 (a) and Figure 1.17 (b). The typical parallel plate capacitance (C) of a BST capacitor as a function of DC bias voltage (V_{dc}) is shown in Figure 1.18.

BST based tunable capacitors have been used in designing various frequency-agile RF circuits, including tunable capacitors (varactors), phase shifters, tunable filters, voltage controlled oscillators, tunable antennas and tunable amplifiers [31-45]. The following section discusses the electrostriction and voltage induced & controlled piezoelectric effect in BST.
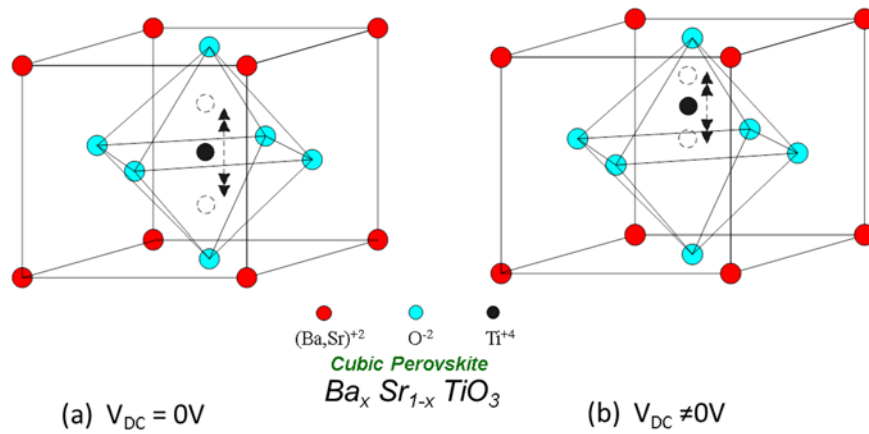
Figure 1.17: Cubic Perovskite unit cell for BST
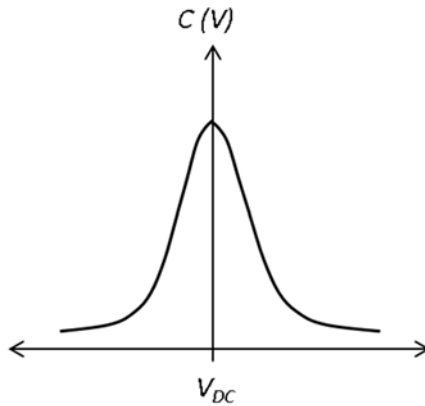
Figure 1.18: The typical DC voltage dependent capacitance response for BST tunable capacitors

1.2.3.2 Electrostriction and Voltage Induced Piezoelectric Effect in BST

Electrostriction is a property of all dielectrics that relates an applied electric field to the induced mechanical strain caused by the electric field [79-81]. Considering this property only in one dimension for simplicity, electric field-induced mechanical strain (S) is related to electric polarization as follows [79, 81]:

$$S = s^E T + QP^2 \qquad (1.17)$$

where s, T, P and Q are the compliance, mechanical stress, electric polarization and charge-related electrostrictive coefficient, respectively [81]. In most dielectrics, the electrostrictive coefficient (Q) is negligible such that (1.17) becomes an uncoupled equation expressing Hooke's law. However, in some dielectric materials such as ferroelectrics, the electrostrictive coefficient is large enough to create significant amounts of electric field-induced mechanical strain. This large electrostrictive coefficient can be used to obtain voltage induced piezoelectricity. Voltage induced piezoelectricity can be briefly explained as follows: in ferroelectrics, electric polarization can be expressed as [79]:

$$P = P_s + \chi E \qquad (1.18)$$

where P_s, χ and E are the spontaneous polarization, susceptibility and electric field, respectively. By plugging (1.18) into (1.17) and assuming there is no applied mechanical stress (T=0), one can obtain electric field induced mechanical strain as follows:

$$S = QP_s^2 + 2QP_s\chi E + Q\chi^2 E^2. \qquad (1.19)$$

In (1.19), the three terms on the right side of the equation, from left to right, represent strain due to the spontaneous polarization, strain due to piezoelectric effect and strain due to electrostrictive effect, respectively [79]. When factoring out the last two terms for the common term E, one can rewrite (1.19) as shown below (1.20) [80]

$$S = QP_s^2 + E(2QP_s\chi + Q\chi^2 E).$$ (1.20)

In (1.20), the two terms in parentheses can be thought of as the effective piezoelectric coefficient since S and E are linearly dependent one another [80]. While the first term of the effective piezoelectric coefficient is constant, the second term is E-field dependent. Therefore, electrostriction can be considered as E-field induced piezoelectricity [80]. When BST is used in the paraelectric phase, the spontaneous polarization is not present (Ps=0) and (1.20) can be simplified as follows:

$$S = E(Q\chi^2 E).$$ (1.21)

As it is seen in (5), at the paraelectric phase, electromechanical transduction occurs primarily through the electric field or voltage induced piezoelectric effect that originates from BST's strong electrostriction.

The voltage induced piezoelectric effect has been utilized in designing bulk acoustic (BAW) resonators for use in multiband and frequency-agile RF circuits [3]. BST based resonators are intrinsically switchable: when BST layer is not subject to an external electric-field, there is no electromechanical transduction; therefore the device acts as a capacitor. With the application of an electric field, electromechanical transduction is turned on and devices act as acoustic resonators.

Recently reported BST and strontium titanate (STO) based switchable resonators are based on FBAR and SMR structures, shown in Figure 1.11. In BST based SMRs and

FBARs, quality factors (Qs) as high as 350 are reported [30, 82]. In addition, BST and strontium titanate (STO) based switchable filters based on SMRs and FBARs are demonstrated [23, 28, 83].

1.2.4 Comparison of Electrostatic, Piezoelectric and Electrostrictive Transduction Mechanisms

Table 1.1 compares the performance of acoustic resonators based on electrostatic, piezoelectric and electrostrictive transduction mechanisms.

Table 1.1 Comparison of resonators based on transduction mechanisms

PROPERTIES	Electrostatic Transduction Based Resonators	Piezoelectric Transduction Based Resonators	Electrostrictive Transduction Based Resonators
Quality Factor (Q)	Very High (>10000)	High (>2000)*	*Low (~ 350)*
Electromechanical coupling (K_t^2)	Low	High*	High*
Motional Resistance (V_{dc})	Very High	Low	Low
DC Bias (V_{dc})	Required (*Voltage controlled Switchable*)	Not Required	Required (*Voltage controlled Switchable*)
Resonance Frequency	Low (<2 GHz)	High	High

* Q_s and K_t^2 are reported for non-composite resonators, such as FBARs and SMRs

- Electrostatic Transduction Based Resonators:

Very large Qs are achievable in electrostatically transduced resonators. In addition to that, the requirement for DC bias voltage makes these resonators attractive in frequency

agile systems, as the resonators can be turned on & off by simply controlling the applied bias voltage. However, very high motional resistance of these resonators is a major limiting their use in RF systems with 50 Ω standard impedance due to significant impedance mismatch.

- Piezoelectric Transduction Based Resonators:

Resonators based on piezoelectric transduction exhibit high Qs with low motional resistance values. Therefore, these resonators are suitable for RF systems in terms of performance and integration with 50 Ω matched components. However, in piezoelectrically transduced resonators, electromechanical transduction cannot be turned off. Therefore, these resonators need RF switches when used in a switched filter bank. RF switches are lossy and increase the size and complexity of the system.

- Electrostrictive Transduction Based Resonators:

Resonators based on electrostrictive transduction exhibit low motional resistance. These resonators need DC bias voltage to be turned on & off, making them intrinsically switchable with the application of bias voltage. Therefore, electrostrictive transduction based resonators are suitable for use in switched filters for multiband and frequency-agile systems. Quality factor (Q) of intrinsically switchable resonators needs further improvement as can be seen in Table 1.1.

1.3 Thesis Goal and Contributions

The goal of this thesis is to improve the quality factor (Q) of intrinsically switchable BST based BAW resonators. To accomplish this goal, low-loss single-crystal silicon (Si) is combined with electrostrictive BST to form a BST-on-Si composite structure.

A fabrication process using silicon-on-insulator (SOI) wafers is developed for fabricating composite BST-on-Si FBARs. Intrinsically switchable BST-on-Si composite FBARs provide measured Qs. This represents the highest Q value reported for BST based BAW resonators utilizing electrostrictive transduction.

Electrically connected and acoustically coupled filters are designed and fabricated using BST-on-Si composite BAW resonators. To the best of author's knowledge, this is the first BST based intrinsically switchable acoustically coupled filter reported.

1.4 Thesis Outline

This thesis is organized as follows:

Chapter 2 discusses the structure and operating principles for FBAR, SMR and composite FBARs. Design considerations and modeling methods for composite FBARs are provided. Subsequently, design and fabrication procedures for high-Q intrinsically switchable BST-on-Si composite FBARs are explained. Finally, measurement results for a fabricated composite FBAR along with extracted mBVD model parameters are presented.

Chapter 3 discusses the intrinsically switchable electrically connected filters based on BST-on-Si composite FBARs. Design and fabrication procedures for electrically connected filters are provided. Finally, the measurement results for a BST-on-Si intrinsically switchable electrically connected filter are presented.

Chapter 4 discusses laterally coupled acoustic filters based on BST-on-Si composite structure. First, the structure and operating principles for acoustically coupled filters are discussed. A lumped element model that represents acoustically coupled filters is provided. Subsequently, finite element method (FEM) based simulation results are

presented for the laterally coupled acoustic filters. Finally, fabrication procedure and measurement results for a laterally coupled acoustic filter are presented.

Chapter 5 summarizes the achievements of this thesis and discusses the future direction for the research at the intrinsically switchable BAW resonators.

Chapter 2

Intrinsically Switchable High-Q, BST-on-Si Composite FBARs

2.1 Introduction

Thin film bulk acoustic resonators (FBARs) are extensively used as BAW filters in wireless applications, such as mobile phones and GPS devices. The main advantages of FBAR filters are their higher power handling levels and higher Q values as compared to SAW filters and much smaller sizes as compared to ceramic filter [84]. High Q values of FBARs allow designing filters with sharp skirts that can meet tight filter roll-off requirements in CDMA duplexers [84].

FBARs have also been proposed for use in low-phase-noise RF oscillators [85-88]. The biggest challenge in the design of FBAR oscillators is to achieve the same temperature stability and phase-noise values as of quartz crystal oscillators that are commonly used in today's wireless devices. However, as FBARs have significant advantages over the quartz crystals in terms of size, frequency of operation and integration with CMOS. These advantages have helped to intensify the effort to further improve FBAR performance in terms of its Q and temperature stability.

Commonly used FBARs are based on several piezoelectric materials such as aluminum nitride (AlN), zinc oxide (ZnO) and lead zirconate titanate (PZT). Currently AlN is the only piezoelectric material used in commercial applications due to its fabrication ease in IC facilities [84]. Recently, electrostrictive transduction has been proposed for use in FBARs [22, 82]. The voltage induced piezoelectric effect that originates from strong electrostriction allows for designing intrinsically switchable resonators and filters, providing more compact switched filters in multiband communication systems. Since the electrostrictive transduction mechanism is relatively new in FBARs, there is a significant need for improving the device performance to meet today's wireless communication standard's requirements.

In this chapter, intrinsically switchable composite FBARs based on BST-on-Si structure is discussed. Emphasis is given in designing thicknesses in vertically stacked layers for optimal device performance. Devices reported in this chapter demonstrate highest achieved Q values for intrinsically switchable BAW resonators utilizing electrostrictive transduction mechanism. This chapter is organized as follows: First, FBAR structures and operation principles are explained. Design considerations and figures of merit (FOM) for the FBARs are discussed. Common FBAR models; modified Butterworth-Van Dyke model and 1-D acoustic transmission line model and are discussed. Subsequently, a detailed TL model based design procedure for high-Q, intrinsically switchable composite FBARs are presented. The detailed fabrication steps for the intrinsically switchable composite FBARs are presented. Finally the measurement results of a high-Q composite FBAR are presented.

2.2   FBAR Structures and Operation Principles

2.2.1   FBAR Structures

FBAR structure consists of a thin film piezoelectric layer sandwiched between two electrodes. An acoustic wave is trapped by the electrode-air interfaces at the top and bottom electrode surfaces, creating an acoustic cavity as shown in Figure 2.1. FBARs are usually fabricated on silicon substrates. To provide electrode-air interface at the bottom electrode, the substrate under the bottom electrode can be removed either completely by creating a hole from the bottom surface of substrate (Figure 2.1 (a)), or partially by creating an air-gap between substrate and bottom electrode (Figure 2.1 (b)).
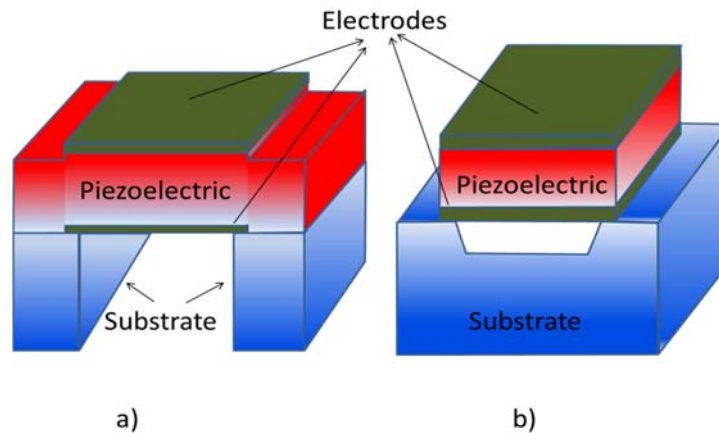
Figure 2.1: The 3-D structure FBAR: Si under the device is removed (a) completely, and (b) partially.

An alternative way for creating an acoustic cavity is to isolate the acoustic energy from the substrate by designing a Bragg reflector under the bottom electrode as shown in Figure 2.2. Since the sandwiched piezoelectric layer is mounted on the substrate with a Bragg reflector, this type of resonator is called a solidly mounted resonator (SMR).
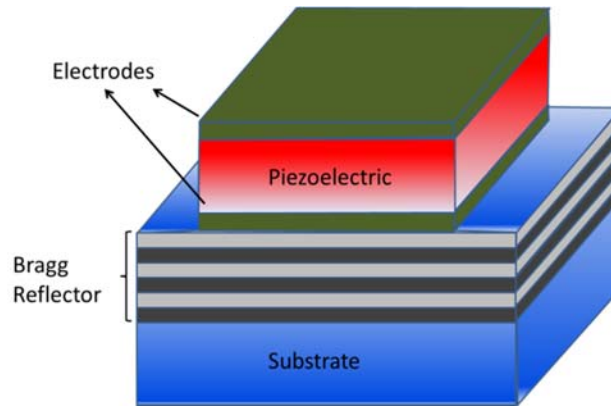
Figure 2.2: The 3-D structure of solidly mounted resonator (SMR)

The Bragg reflector consists of multiple layers of thin films with alternating acoustic impedances stacked vertically as shown in Figure 2.2. The SMRs are fabricated by planar micro-fabrication techniques with successive deposition and lithography steps. Therefore, the SMRs are advantageous in terms of robustness. However, the SMRs usually exhibit lower resonator performance in terms of quality factor and electromechanical coupling as compared to FBARs [51]. This is due to lower acoustic wave reflecting performance of the Bragg reflector as compared to the air-electrode interface [51].

Composite structure has been used in FBARs to improve the Q and the robustness of the resonators [47-50]. The intrinsically switchable composite FBARs presented in this chapter are based on BST-on-Si structure as shown in Figure 2.3. Ferroelectric BST is used mainly as the transduction layer. The strong electrostriction in BST renders the composite FBAR intrinsically switchable as a function of DC bias. The Si membrane, which is relatively thick as compared to BST layer, is used to increase the resonator Q and robustness.
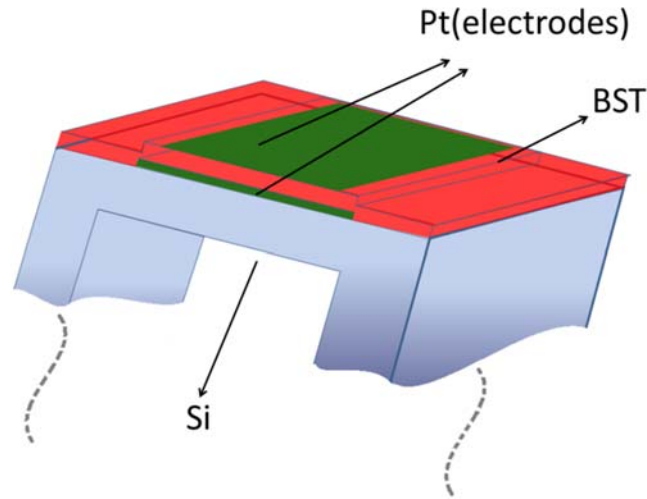
Figure 2.3: The 3-D structure of the intrinsically switchable BST-on-Si Composite FBARs

In intrinsically switchable composite FBARs, the acoustic energy is trapped within the BST-on-Si structure by the air-electrode and the air-Si interfaces at the top and bottom of the resonator, respectively. Therefore, significant amounts of acoustic energy stay inside the low-loss Si layer, increasing the Q of the resonator at the cost of reduced electromechanical coupling. In composite FBARs, the thicknesses of the transduction layer (BST), the membrane (Si) and resonance mode of operation should be chosen carefully for a desired resonance frequency and performance, as will be discussed later in this chapter.

2.2.2   FBAR Operation Principles

The FBARs (non-composite) operate at the structure's fundamental thickness-extensional mode of vibration. In this mode, resonator structure exhibits largest acoustic displacement at the top and bottom air-electrode interfaces and a displacement node at the center of the piezoelectric layer. There is approximately a half-wavelength acoustic displacement across the resonator structure as shown in Figure 2.4. Resonator Q is

mainly affected by the mechanical loss of the piezoelectric layer and electrodes. In FBARs (non-composite) and SMRs, even order resonance modes do not exist due to symmetry of structure. Furthermore, higher order odd resonance modes are very weak due to very small effective electromechanical coupling coefficient (K_t^2). Therefore, these resonators are usually utilized at their fundamental resonance mode.
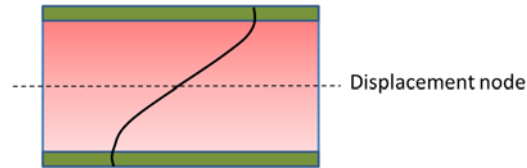
Figure 2.4: Acoustic displacement across FBARs at fundamental resonance mode

On the other hand, composite FBARs operate at higher order thickness-extensional resonance modes. The strongest resonance mode is determined by the thicknesses and mechanical Q of each layer. To illustrate higher order resonance mode shapes, acoustic displacement across composite FBARs operating at 3rd and 4th resonance modes for are shown in Figure 2.5 for the maximum electromechanical coupling.

3rd mode   4th mode
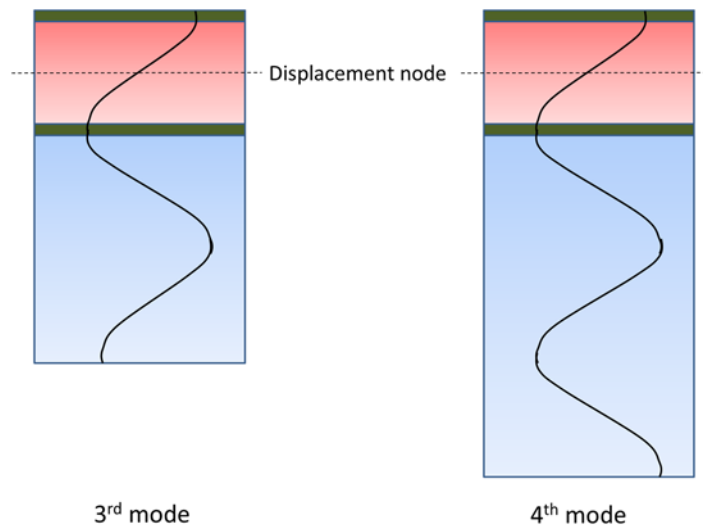
Figure 2.5: Acoustic displacement across composite FBAR structure (a) at 3rd resonance mode, (b) at 4th resonance mode.

Design of thicknesses in composite FBARs will be explained in detail in the following sections. Before that, FBAR design considerations should be discussed to explain FBAR performance figures that are optimized in the design section.

2.3   Composite FBAR Design Considerations

The typical impedance response of a 1-port composite FBAR, near a resonance mode, is shown in Figure 2.6 and Figure 2.7 on cartesian and Smith chart plots, respectively. In composite FBARs, each resonance mode exhibits a series (f_s) and a parallel resonance frequency (f_p). The f_s and f_p are defined as the frequencies where the real part of the admittance and impedance reach their maximum value, respectively, for a particular resonance mode [15]. Unless the resonator Q is very small, the f_s and f_p correspond to the points where the phase or imaginary component of complex impedance becomes zero, as indicated in Figure 2.6 and Figure 2.7. Therefore, the input impedance becomes purely resistive at series and parallel resonance frequencies. These resistors can be represented by R_{fs} and R_{fp} at f_s and f_p, respectively, and are important parameters when designing FBAR filters [51, 84]. The impedance of the FBAR is capacitive everywhere except the frequencies between the f_s and f_p, where the resonator exhibits an inductive impedance response.

There are three important figures to evaluate the performance of composite FBARs at a particular resonance mode. These figures are the effective electromechanical coupling coefficient (K_t^2), the quality factor (Q) and K_t^2Q product, and will be discussed in detail in the following sections [51, 84].
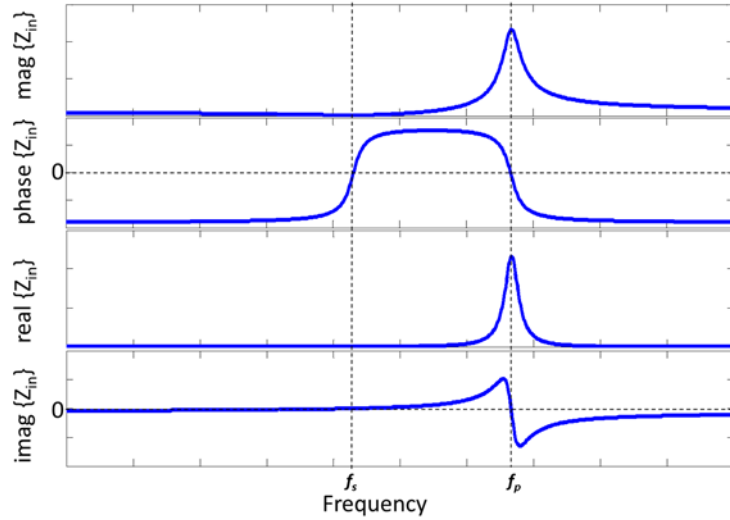
Figure 2.6: The typical impedance response of an FBAR near a resonance mode on Cartesian plot
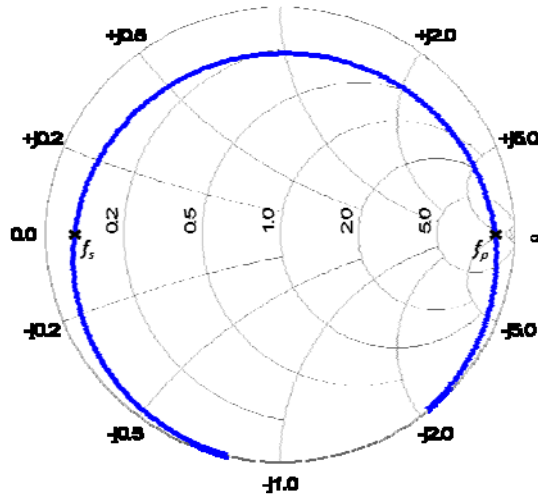
Figure 2.7: The typical impedance response of an FBAR near a resonance mode on Smith Chart plot

2.3.1 Effective Electromechanical Coupling Coefficient ($K_t{}^2$)

The effective electromechanical coupling coefficient ($K_t{}^2$) represents the electromechanical conversion efficiency at a particular resonance mode. It is directly related to the intrinsic electromechanical coupling coefficient (K^2) of the transduction

41

layer. The exact relationship between K_t^2, K^2 and the thicknesses for the composite FBARs will be given in the 1-D transmission line modeling section of this chapter. The K_t^2 at any resonance mode can be calculated from the input impedance using the series (f_s) and parallel (f_p) resonance frequencies as follows [47]:

$$K_t^2 = \frac{\pi}{2} \frac{f_s}{f_p} \tan\left(\frac{\pi}{2} \frac{(f_p - f_s)}{f_p}\right).$$

(2.1)

The K_t^2 is very important in the design of FBAR filters. The maximum achievable filter bandwidth (BW) is limited by the K_t^2 of the FBARs in an FBAR filter [51, 89]. Furthermore, the insertion loss and out-of-band rejection performance of an FBAR filter is directly related to the $K_t^2 Q$ product of each resonator [51, 84, 90, 91]. If FBARs are utilized in oscillators, the K_t^2 is not as important as Q for the oscillator performance; however, a very small K_t^2 may prevent oscillations from starting up [88]. In order for a resonator to provide an inductive region between the series and parallel resonance frequencies, where majority of the oscillators operates [87], a $K_t^2 Q$ product of more than approximately 2.5 is required [92].

2.3.2   Quality Factor (Q)

The Q represents the ratio of stored energy to dissipated power per cycle in resonators [51]. A high Q resonance response is desired in the FBARs. As mentioned in the previous section, the $K_t^2 Q$ product directly affects the insertion loss and rejection level performance of FBAR filters. In FBAR based oscillators, the oscillator phase-noise is inversely proportional to the resonator Q^2 [93]. Therefore, obtaining a high Q resonance response is vital in designing a low-phase noise oscillator. The Q of an FBAR at a

particular resonance mode can be calculated from the input impedance response using [47]:

$$Q_{s,p} = \frac{f}{2} \left| \frac{d\phi_{Zin}}{df} \right|_{f=fs,fp}$$ (2.2)

where ϕ_{Zin} is the phase of input impedance and Q_s and Q_p represent the resonator Qs at f_s and f_p, respectively.

2.3.3 The Figure of Merit (K_t^2Q Product)

The K_t^2Q product for an FBAR is defined as a figure of merit (FOM) for FBARs [51]. At a given resonance mode, the size of the resonance circle on Smith chart is proportional to the K_t^2Q product at that resonance mode. Larger circle sizes are highly desirable in FBAR filters and oscillators [51]. This is because, the resistance values at the series and parallel resonance frequencies (R_{fs} and R_{fp}) are related to the size of resonance circles. Smaller R_{fs} and larger R_{fp} values are required for good filter and oscillator performance [51].

Figure 2.8 (a), (b) shows the simulated impedance response for an FBAR near a resonance mode for various K_t^2Q product values. Figure 2.9 shows the impedance response of an FBAR for a constant K_t^2Q product with various K_t^2 and Q values. As seen in Figure 2.8 (a) and (b), the size of the resonance circles increases with larger K_t^2Q product. When K_t^2Q product is maintained constant, the size of the resonance circles are maintained, regardless of the individual values for K_t^2 and Q as shown in Figure 2.9 (c). In these simulations, the R_{fs} and R_{fp} are also calculated for various K_t^2Q product values. Smaller R_{fs} and larger R_{fp} values are obtained as the K_t^2Q product increases, as shown in Figure 2.10. It should be noted that in Figure 2.8-Figure 2.10, the static capacitance of

the resonator is chosen such that the FBAR exhibits a 50 Ω capacitive impedance; therefore the resonance circles starts at $-j1$ on the Smith chart

(a) $K_t^2 = 0.05$ (constant)

(b) $Q = 500$ (constant)
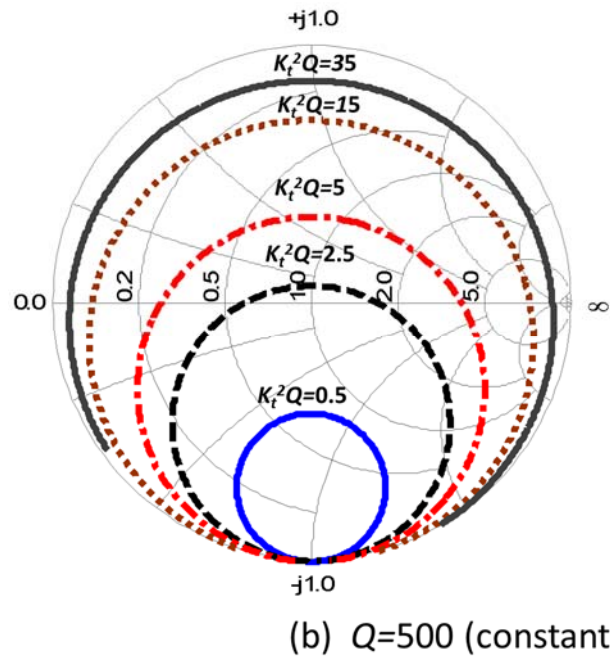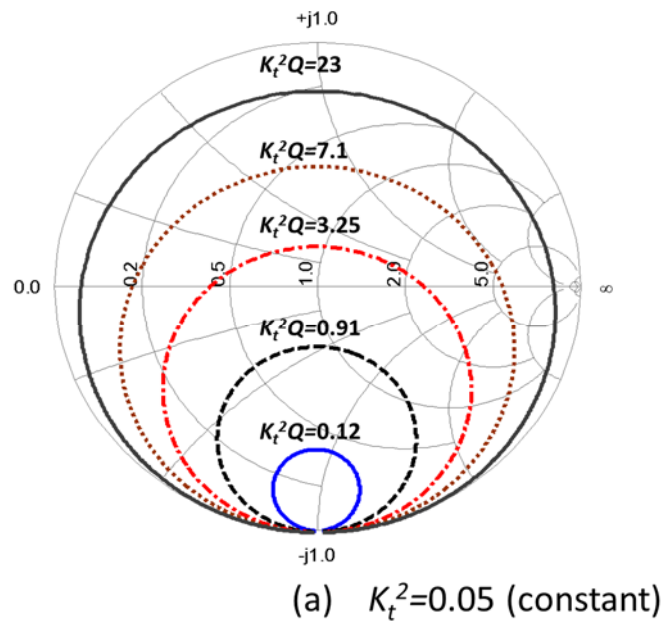
Figure 2.8: Resonance circles on Smith chart (a) for constant K_t^2 with increasing K_t^2Q product (b) constant Q with increasing K_t^2Q product

(c) $K_t^2Q=10$ (constant)
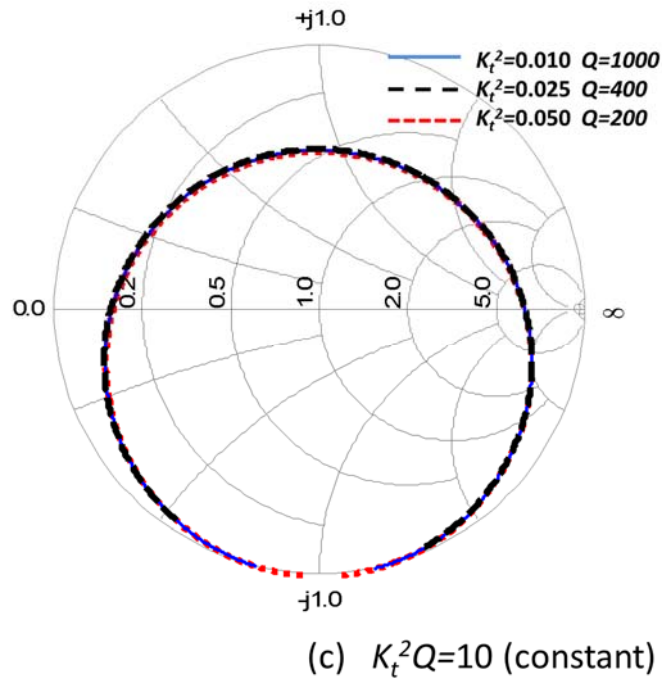
Figure 2.9: Resonance circles on Smith chart for constant K_t^2Q product with various K_t^2 and Q.
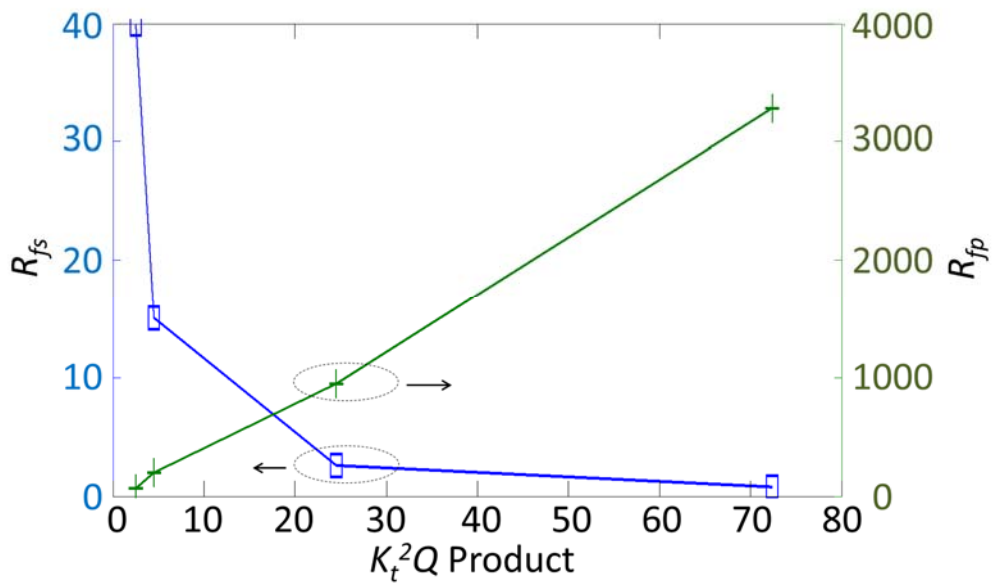
Figure 2.10: The R_{fs} and R_{fp} as a function of K_t^2Q product

2.4   FBAR Modeling

2.4.1   A Lumped Element Model (mBVD Model)

An FBAR can be represented accurately by a modified Butterworth Van-Dyke (mBVD) model shown in Figure 2.11 [94]. The mBVD model consists of the motional and the electrical branches, which are parallel to each other. The motional branch is formed by a series connected resistor (R_m), capacitor (C_m) and inductor (L_m) which represent the series resonance of the given resonance mode. The R_m in combination with L_m and C_m represents the acoustic Q of the device. The electrical branch is formed by a series-connected resistor (R_e) and a capacitor (C_e) as shown in Figure 2.11. The combination of C_e, L_m, and C_m represents the parallel resonance of the given resonance mode. In Figure 2.11, C_e represents the parallel plate capacitance formed by the electrodes and transduction layer (BST). The resistors R_p, R_s, and R_e account for electrical losses. The R_s represents the resistive losses associated with electrodes, and the R_e and the R_p represent the dielectric losses associated with the transduction layer.
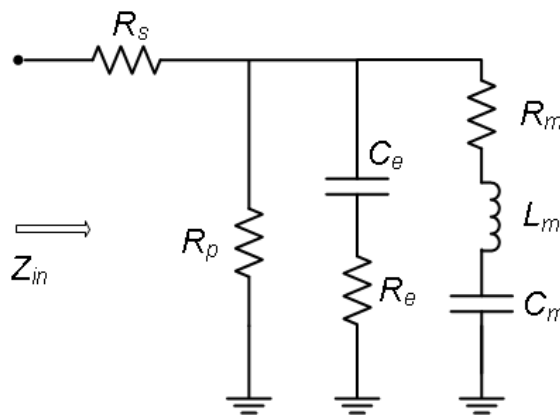
Figure 2.11: The modified Butterworth Van-Dyke Model

The parallel plate capacitance of the FBAR, shown in Figure 2.11, is a function of resonator area through the following equation:

$$C_e = \frac{\varepsilon_0 \varepsilon_r A}{d} \tag{2.3}$$

where ε_0, ε_r, A, and d are the permittivity of air, relative permittivity of transduction layer (BST), the area of the FBAR, and the thickness of the transduction layer, respectively. The lumped components in mBVD model shown in Figure 2.11, at a particular resonance mode, are related to the device geometry and material properties as follows [100]:

$$C_m = \frac{8}{\pi^2} K_t^2 C_e = \frac{8}{\pi^2} K_t^2 \frac{\varepsilon_0 \varepsilon_r A}{d} \tag{2.4}$$

$$L_m = \frac{1}{(2\pi f_s)^2 C_m} \tag{2.5}$$

$$R_m = \frac{2\pi f_s L_m}{Q}. \tag{2.6}$$

In (2.7), K_t^2 is a function of the piezoelectric coefficient and acoustic properties of the transduction layer and the layer thicknesses which constitute the composite FBAR structure. The exact relationship between K_t^2 and layer thicknesses is provided in the following 1-D acoustic transmission line model section. Note that in (2.6), the Q represents the quality factor of the resonance mode in case the effect of parasitic resistances (R_s , R_p and R_e) is not included. In this case, the quality factor at series and parallel resonance frequencies, Q_s and Q_p, respectively, are the same and equal to Q. The Q is a function of mechanical quality factor of each layer (Q_m) and layer thicknesses of the composite FBAR. The exact relationship between Q, Q_m and the layer thicknesses is discussed in the following 1-D acoustic transmission line model section.

47

The mBVD model is useful in the circuit simulation softwares when designing FBAR based circuits, such as filters and oscillators. The values of lumped components in mBVD model are a function FBAR geometry [95]. Therefore, the required mBVD component values for a desired filter or oscillator performance can be used to determine optimum device geometry. Furthermore, the mBVD model helps distinguishing various loss mechanisms that affect the Q of the FBARs, when fitted to an FBAR measurement results. For example, the extracted R_s, which represents the conductor losses of electrodes, mainly degrades the Q at the series resonance frequency (Q_s).

2.4.2 A 1-D Acoustic Transmission Line Model

A composite FBAR consists of various layers, such as transduction layer (BST), electrodes and membrane as shown in Figure 2.12. Therefore, a model that provides electrical impedance as a function of layer thicknesses and acoustic properties is needed for designing composite FBARs.

A 1-dimensional acoustic transmission line model [47, 96] is utilized in the design of the intrinsically switchable composite FBARs presented in this chapter. In this model, each layer in the composite FBAR structure is represented as a transmission line with acoustic wave propagating in the vertical direction with respect to the electrode surfaces. The layers considered in the model, which constitute the intrinsically switchable composite FBAR structure, are the top electrode, the electromechanical transduction layer, the bottom electrode, the buffer layer, and the Si membrane, respectively, as shown in Figure 2.12. Gold (Au) and platinum (Pt) are used to form the top and bottom electrodes. The BST is used as the transduction layer due to its strong electrostrictive effect. Silicon dioxide (SiO_2) is used as a buffer layer, acting as a diffusion barrier

48

between the Si membrane and the Pt bottom electrode during high temperature deposition of BST thin film. Single crystalline, (100)-oriented Si is used as the low mechanical loss membrane layer.

In the transmission line model, the air is represented by its acoustic characteristic impedance $Z_{0\ (air)}$ as shown in Figure 2.12. This impedance is transformed to acoustic impedances of Z_t and Z_b (Figure 2.12), through successive impedance transformations using [97]

$$Z = Z_0 \frac{Z_L + Z_0 \tanh(\gamma t)}{Z_0 + Z_L \tanh(\gamma t)} \tag{2.7}$$

where, γ, t, Z_0 and Z_L, are the acoustic propagation constant of each layer, thickness of each layer, acoustic characteristic impedance of each layer and acoustic impedance seen looking into previous layer, respectively. The complex propagation constant (γ) for each layer, used in (2.7), is calculated using (2.8) and (2.9) [98]:

$$\gamma = \alpha + j\beta \tag{2.8}$$

$$\beta = \frac{\omega}{v} \ , \alpha = \frac{\beta}{2Q_m} \tag{2.9}$$

where α, β, ω, v and Q_m represent the attenuation constant, phase constant, angular frequency, acoustic velocity and the mechanical quality factor for each layer, respectively. The calculated acoustic impedances Z_t and Z_b are then normalized by the acoustic characteristic impedance of BST ($Z_{0\ (BST)}$):

$$\overline{z_t} = \frac{Z_t}{Z_{0\ (BST)}} \ , \ \overline{z_b} = \frac{Z_b}{Z_{0\ (BST)}} \ . \tag{2.10}$$

Finally, the composite FBAR's electrical impedance ($Z_{electric}$) is calculated using (2.11) [47]:

$$Z_{electric} = \frac{1}{j\omega C_e} \cdot \left[1 - K^2 \frac{\tan(\frac{\varphi}{2})}{\frac{\varphi}{2}} \cdot \frac{\left(\overline{z_t} + \overline{z_b} \right)\cos^2(\frac{\varphi}{2}) + j\sin(\varphi)}{\left(\overline{z_t} + \overline{z_b} \right)\cos(\varphi) + j\left(\overline{z_t}\,\overline{z_b} + 1 \right)\sin(\varphi)} \right] \qquad (2.11)$$

where K^2, φ, and C_e are the electromechanical coupling coefficient of the BST, the acoustic phase across the BST layer and the parallel plate capacitance between the top and bottom electrodes, respectively. The parameters for each layer used in the transmission line mode are provided in Table 2.1.

Table 2.1 Acoustic parameters used in transmission line model

Material	v (m/s)	Z_0(kg/m^2·s)	Q_m	K^2
Pt	3300	69.8×10^6	130	-
BST	5600	33.0×10^6	300	0.062
SiO$_2$	5100	12.5×10^6	130	-
Si	8100	19.5×10^6	5000	-
Au	2800	63.8×10^6	130	-
Air	360	4.0×10^2	-	-

In the following simulations, the dielectric loss of the BST layer and the conductor loss of electrodes are accounted for in the transmission line model by adding a shunt resistance R_p and a series resistance R_s as shown in Figure 2.12 [46]. The R_p is calculated using

$$R_p = \frac{1}{\omega C_e \tan \delta} \qquad (2.12)$$

where the loss tangent (tan δ) for the BST layer is 0.007 [99]. The value of R_s is 1 Ω which is approximated based on the mBVD model fitted to previously fabricated devices. By taking R_s and R_p into consideration, the electrical input impedance in (2.11) is modified as follows:

$$Z_{in} = R_s + \left(\frac{R_p \cdot Z_{electric}}{R_p + Z_{electric}} \right) \qquad (2.13)$$
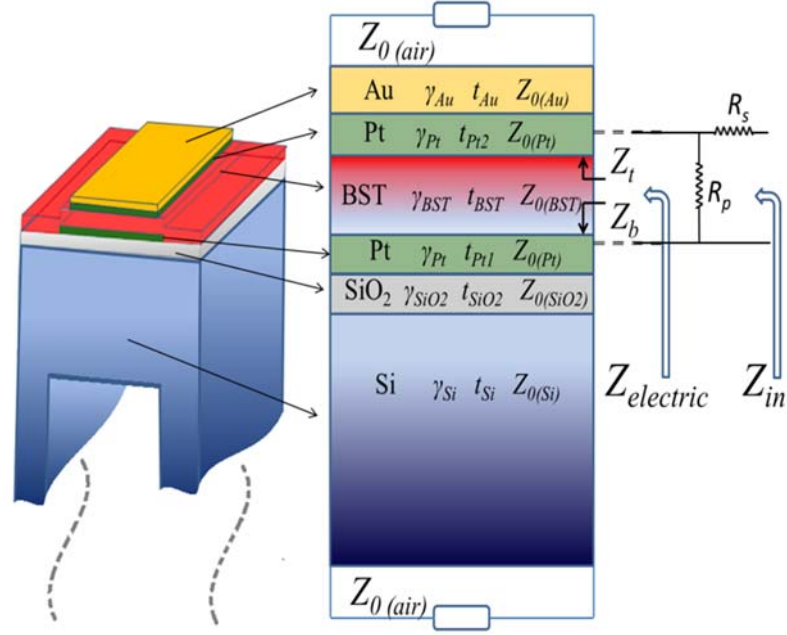
Figure 2.12: Acoustic TL model for composite FBARs.

Based on the input impedance given in

(2.13), the series (f_s) and parallel (f_p) resonance frequencies for a given resonance mode are determined. From the input impedance, the resonator K_t^2 and Q are calculated for each resonance mode using (2.1) and (2.2). By considering the resonance frequencies, quality factors, and electromechanical coupling coefficient at each resonance mode, the optimal thicknesses for the composite FBARs can be determined.

2.5 BST-on-Si Composite FBAR Design

2.5.1 Optimum BST and Si Thicknesses

In composite FBARs, the values of K_t^2 and Q as well as the resonance frequency at each resonance mode are strongly dependent on the distribution of acoustic displacement

across the resonator structure [46, 48-50, 96]. Therefore, optimization of the thicknesses of each layer, especially the transduction layer (BST) and the membrane layer (Si), is very important in achieving the desired resonator performance [46, 48-50]. The optimum thicknesses of the layers for intrinsically switchable composite FBARs are determined using the transmission line mode discussed in the previous section.

The high-Q intrinsically switchable composite FBAR presented in this chapter is designed for a 1.25 GHz operation. To determine the appropriate BST and Si thicknesses, and resonance mode of operation, the resonator electrical input impedance ($Z_{electric}$) is simulated as a function of BST to Si thickness ratio using the acoustic transmission line model. The thicknesses of the electrodes and buffer layer used in the model are given in Table 2.2.

Table 2.2 Thicknesses of electrodes and buffer layer

	Material	*Thickness*
Top Electrode	Pt+Au	150nm+100nm
Bottom Electrode	Pt	150 nm
Buffer Layer	SiO$_2$	200nm

The K_t^2 and Q are calculated from $Z_{electric}$ using (2.1) and (2.2) at various resonance modes. The resonance frequency is set at 1.25 GHz. As the BST to Si thickness ratio change, to maintain the resonance frequency constant, both BST and Si thicknesses must be adjusted. The plots of the predicted K_t^2 and Q as a function of thickness ratio at various resonance modes are shown in Figure 2.13 and Figure 2.14, respectively. Finally, for operation at 1.25 GHz, the required BST thickness as a function of BST to Si thickness ratio at various resonance modes is determined and shown in Figure 2.15. By using the plots in Figure 2.13, Figure 2.14 and Figure 2.15, the optimum BST and Si

thicknesses can be chosen for a desired resonator performance. It should be noted that the effect of parasitic resistances, R_s and R_p, has not been taken in to account yet in the calculation of the K_t^2 and Q, shown in Figure 2.13 and Figure 2.14. The R_s and R_p will be added to the model once the optimum thicknesses and resonance mode are chosen.

As seen in Figure 2.13 and Figure 2.14 each resonance mode exhibits peak Q and K_t^2 as a function of BST to Si thickness ratio. The K_t^2 peak values decrease with mode number, because the fraction of acoustic displacement across the BST layer (transduction layer) reduces. The Q peak values, on the other hand, increase with mode number; since the fraction of acoustic displacement across the low loss Si layer increases. Furthermore, the effect of losses from electrode and SiO_2 layers also decreases with mode number, since the Si thickness increases with mode number while electrode and SiO_2 thickness is constant. For example, the peak Q ($\sim$ 600) at 2nd resonance mode occurs with a BST to Si thickness ratio of approximately 0.1, as seen in Figure 2.14. For 1.25 GHz operation, the required BST and Si thicknesses are 450 nm and 4.5 μm, respectively. However, the required BST and Si thicknesses are approximately 500 nm and 17 μm at the peak Q ($\sim$ 1500), which occurs at a BST to Si thickness ratio of 0.03, for 6th resonance mode.
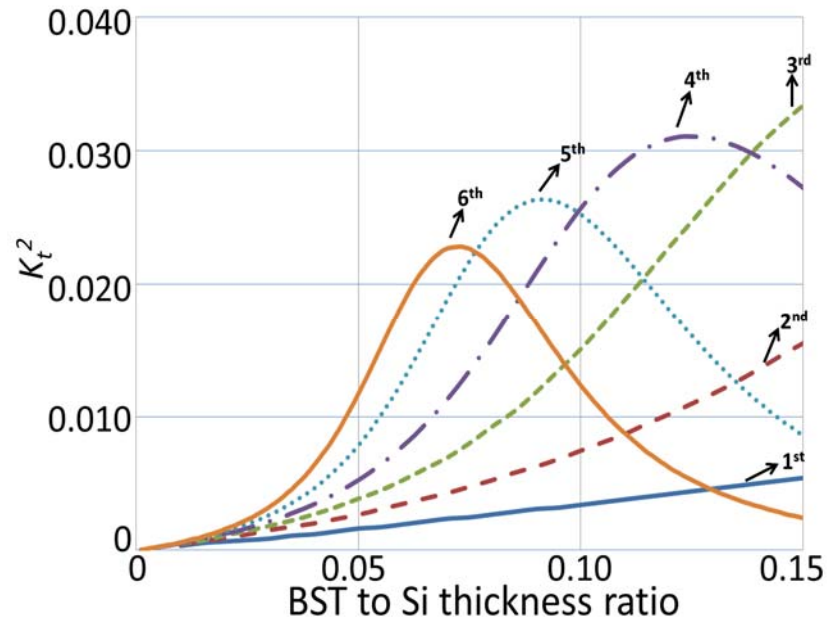
Figure 2.13: The K_t^2 as a function of BST to Si thickness ratio
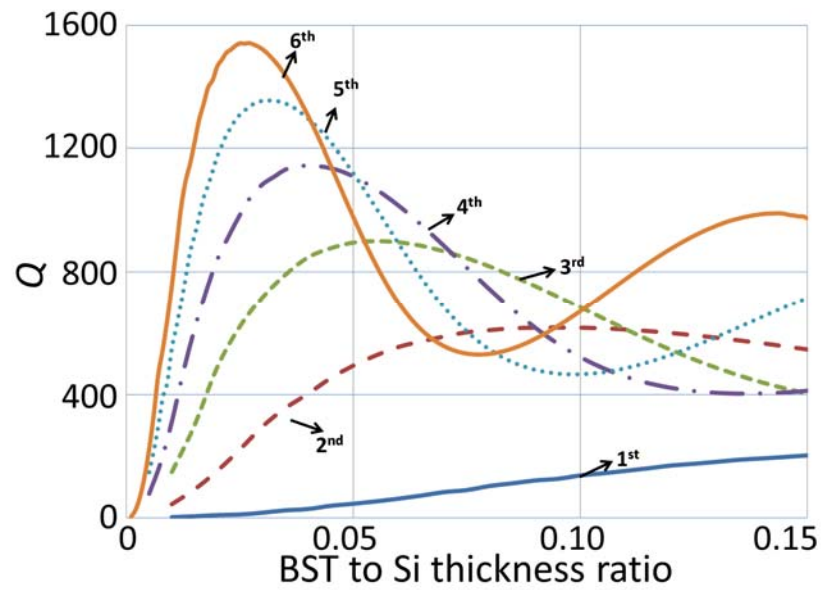
Figure 2.14: The Q as a function of BST to Si thickness ratio
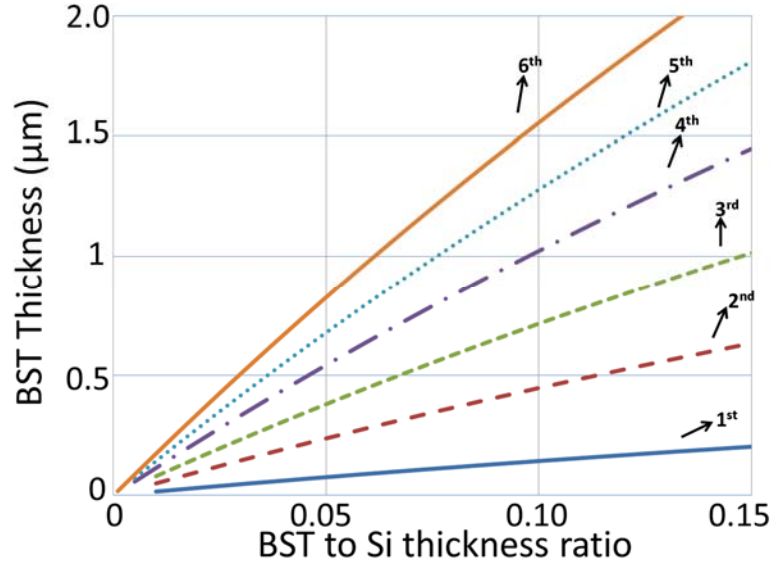
Figure 2.15: The BST thickness as a function of BST to Si thickness ratio

Although higher order modes can provide higher Qs, in this work, the 4th resonance mode is selected to achieve high Q values while avoiding highly overmoded resonator design. Based on the K_t^2 and Q plots in Figure 2.13 and Figure 2.14, the targeted BST to Si thickness ratio in this work is 0.05, near peak Q for the 4th resonance mode with K_t^2 of more than 0.005. After adding the parasitic resistances R_s and R_p to the model, the predicted Qs are approximately 800 and 1000 at series and parallel resonance frequencies (Q_s and Q_p), respectively. The required BST and Si thickness values, obtained using Figure 2.15, are 540 nm and 10.8 μm, respectively. An off-the-shelf SOI wafer with a 10 μm thick Si device layer is used to design and fabricate the composite FBARs. In this case, to maintain the BST to Si thickness ratio, the required BST thickness is modified to 500 nm, providing a slightly increased resonance frequency.

For a comparison, a non-composite FBAR is also simulated in a transmission line model using the acoustic parameters of BST and Pt and Au layers given in Table I. A

non-composite FBAR with a 1.2 μm thick layer of BST provides a fundamental resonance frequency of approximately 1.25 GHz with a K_t^2, Q_s and Q_p of 0.07, 160 and 210, respectively. Therefore, composite FBARs exhibit significantly higher Qs with reduced K_t^2 as compared to non-composite FBARs.

2.5.2   The Effect of FBAR Area on the Input Impedance

The area of an FBAR determines the impedance of the resonator. Figure 2.16 shows the resonance circles for the composite FBAR near the 4th resonance mode for various composite FBAR areas. This plot is obtained from the transmission line model with optimized BST and Si thicknesses for 4th resonance mode as discussed in the previous section. The lumped components in mBVD model shown in Figure 2.11, at a particular resonance mode is given in (2.3)-(2.6). As seen in (2.3) and (2.4), the C_e and C_m increase with the resonator area. Figure 2.17 shows the extracted C_e and C_m from the transmission line model as a function of FBAR area for the 4th resonance mode at 1.25 GHz. On the other hand, the L_m and R_m decrease with the resonator area as can be seen in (2.5) and (2.6). Figure 2.18 shows the extracted L_m and R_m from the transmission line model as a function of resonator area.

In FBAR filters, the optimum FBAR area depends on the desired filter specifications and port impedance. For example, for a higher out-of-band-rejection, smaller series and larger shunt FBARs are utilized in ladder type FBAR filters [3, 83]. On the other hand, a smaller R_m is desired for low power consumption in FBAR based oscillators [101]. Therefore, the FBAR area should be large enough to provide a small R_m. However, the parasitic resistances, R_s, R_p, and R_e shown in Figure 2.11 become more effective on the resonator Q when R_m is very small [30], degrading the performance of the FBAR. Hence,

an optimum FBAR area depends on the application and desired resonator performance. In this work, BST-on-Si composite FBARs with various areas are fabricated with optimum thicknesses determined in the previous section.
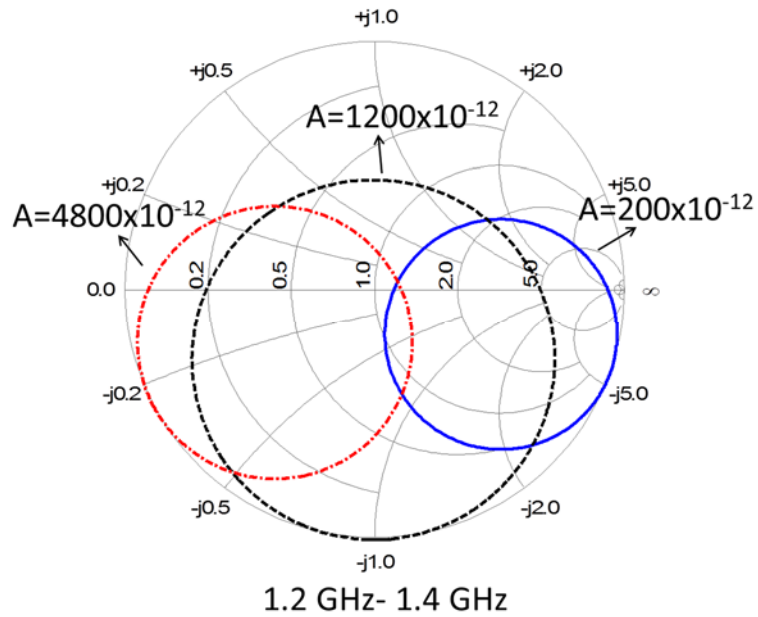
Figure 2.16: The resonance circles for various FBAR areas
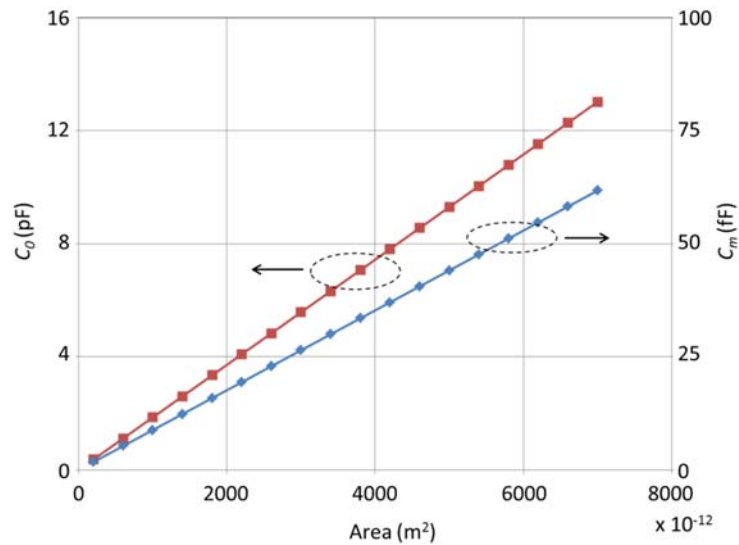
Figure 2.17: The C_0 and C_m as a function of FBAR area at 4th resonance mode
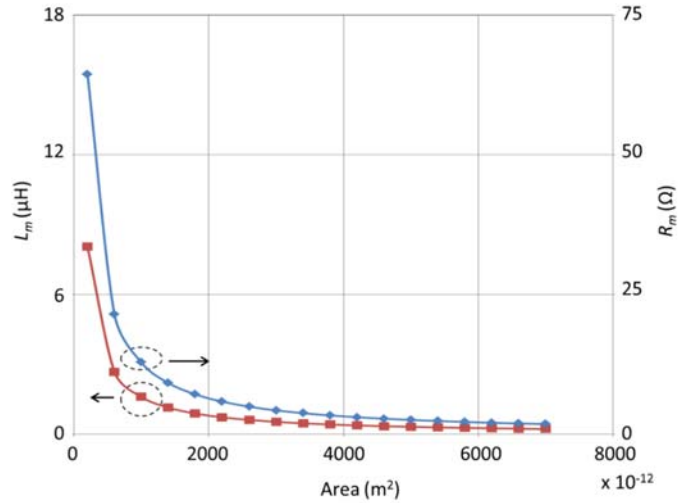
Figure 2.18: The L_m and R_m as a function of FBAR area at 4th resonance mode

2.6 BST-on-Si Composite FBAR Fabrication

Composite FBARs based on the BST-on-Si structure are fabricated on a silicon-on-insulator (SOI) wafer. The SOI wafer has a 10 μm thick, (100)-oriented high resistivity Si device layer on top of a 0.6 μm thick buried oxide layer and a 500 μm thick Si handle layer as shown in Figure 2.19. The 10 μm thick device layer forms the Si membrane for the composite FBARs. The buried oxide is used as the etch-stop during the releasing step in the fabrication of composite FBARs.
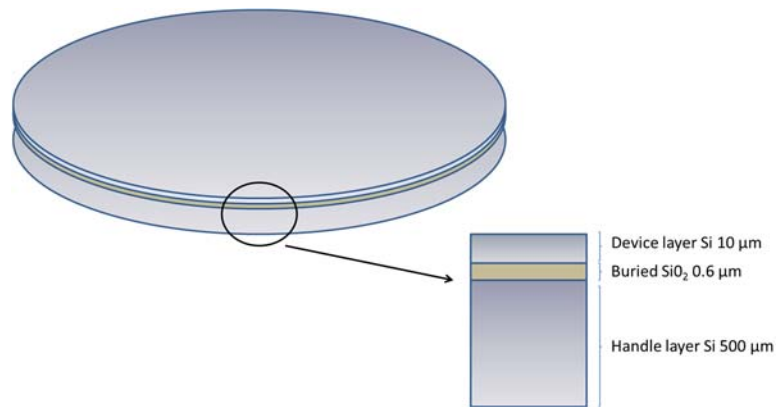
Figure 2.19: The structure of the SOI wafer used in the fabrication of BST-on-Si composite FBARs

The device fabrication starts with growing a 200 nm thick layer of high quality SiO_2 on the SOI wafer. This SiO_2 layer serves as a buffer layer during the high temperature deposition of BST layer. A 40 nm of TiO_2 and a 150 nm layer of platinum (bottom electrode) are deposited on the SiO_2 layer. The bottom electrode is patterned by selectively etching the Pt. Approximately 500 nm BST is deposited on top of the bottom electrode by pulsed laser deposition (PLD) at a substrate temperature of 650 °C under a partial oxygen pressure of 300 mT. Next, a 100 nm thick layer of platinum and a 100 nm thick layer of gold is deposited and patterned by e-beam evaporation and lift-off for the top electrode. The BST thin film is selectively etched using diluted hydrofluoric acid (HF). A 500 nm thick layer of gold is deposited for the probe contact pads. The silicon handle layer is etched away completely by deep reactive ion etching (DRIE) from the back side of the wafer. Finally, the buried oxide layer is wet etched to fully release the device. The fabrication steps for the BST-on-Si composite FBARs are illustrated in Figure 2.20. The detailed recipes for each step are given in Appendix A.

1) SiO_2 and TiO_2 layers deposited. Bottom electrode deposited and patterned

3) Part of BST layer is etched to reach bottom electrodes. Gold layers are deposited on measurement pads and top electrode.

2) BST layer is deposited by PLD. Top electrodes are deposited and patterned by lift-off

4) Buried oxide is wet etched as a final step

Au   Pt   Si   BST   SiO2
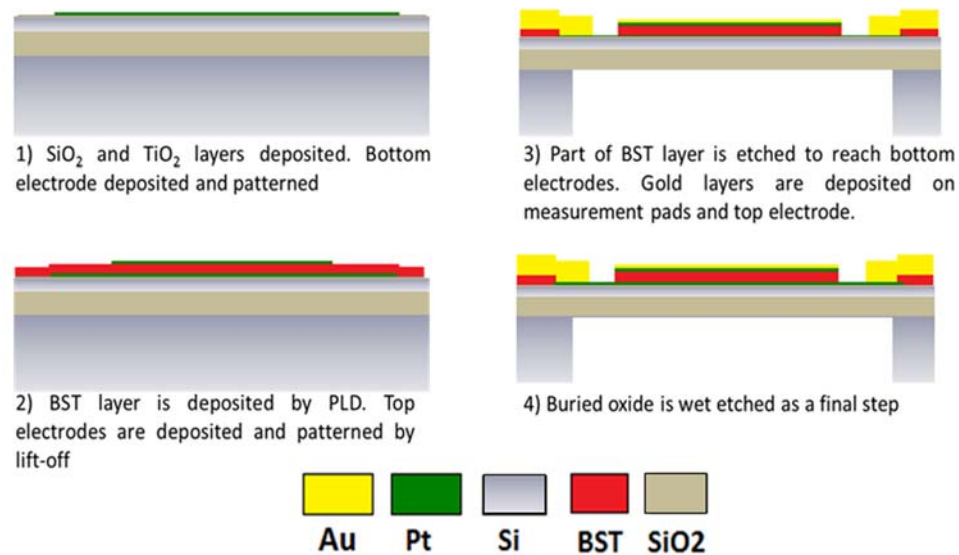
Figure 2.20: The fabrication steps for BST-on-Si composite FBARs.

2.7 BST-on-Si Composite FBAR Measurement Results

The fabricated composite FBARs are measured with a ground-signal-ground (GSG) RF probe using an Agilent E8364C PNA network analyzer. The DC bias voltage (V_{dc}) is applied through the measurement port using a bias tee. A photograph of a measured device with an area of 60 µm × 80 µm is shown in Figure 2.21.
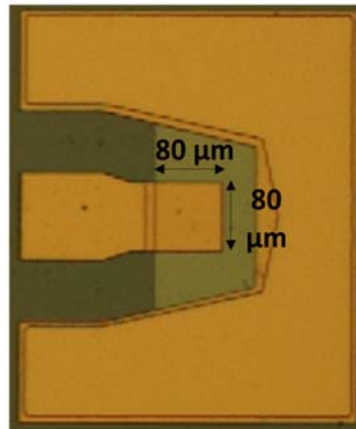
Figure 2.21**:** Microscope photograph of measured composite FBAR with an area of 80µm × 60µm

During the measurement, the bias voltage is increased gradually from 0 V to 25 V until the input impedance no longer varies with the bias voltage due to the saturation of the voltage-induced electric polarization in the BST layer [78]. The measured input impedance (Z_{in}) and reflection coefficient (S_{11}) for a high-Q intrinsically switchable composite FBAR are shown in Figure 2.22. As seen in Figure 2.22, no acoustic resonance mode is observed at 0 V dc bias; therefore, there is no electromechanical transduction. Strong acoustic resonance modes appear with the application of the dc bias voltage (e.g V_{dc}=25V) due to electrostriction in the BST layer, clearly demonstrating the bias dependent switchable BST thin film resonators.

To evaluate the accuracy of the transmission line model used in the design procedure, the input impedance of a measured device at 25 V dc bias is compared with the input impedance obtained from the transmission line model and shown in Figure 2.23. The measured resonance frequencies are slightly lower than those obtained from the transmission line model. This can be attributed to small deviations in the thicknesses of the fabricated device.
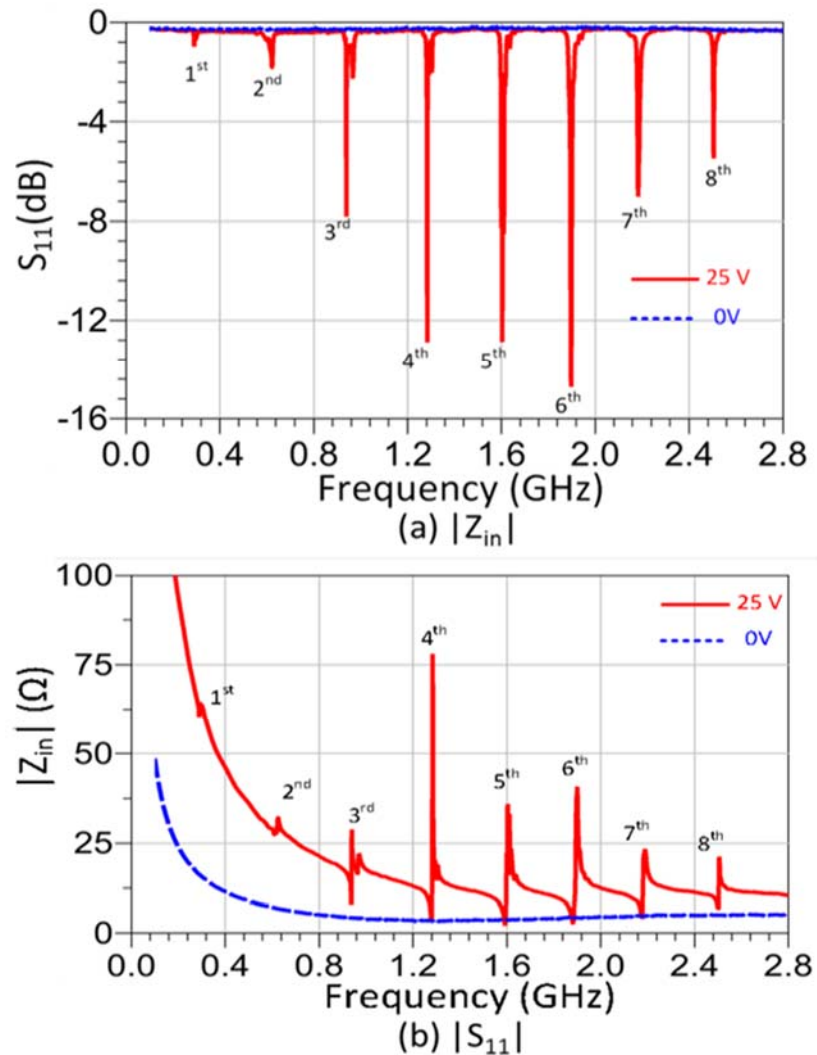
Figure 2.22: Measured magnitude of (a) S_{11} and (b) input impedance of a composite FBAR for 0 V and 25 V dc bias
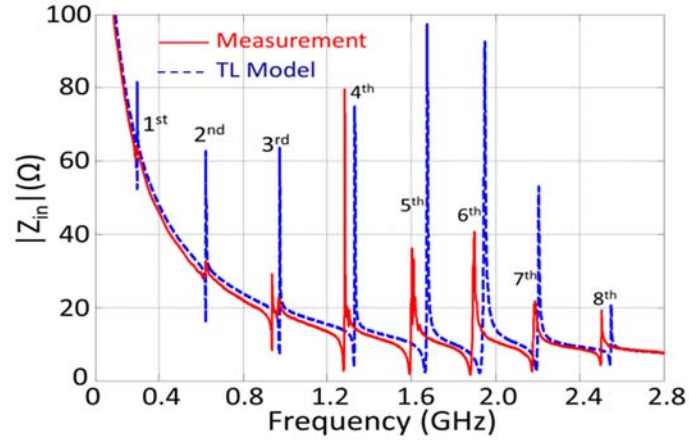
Figure 2.23: The comparison of input impedance vs. frequency between measurement results and transmission line model

The differences between the measurement and transmission line model results are attributed to effects that cannot be simulated in transmission line model, such as the spurious resonances, the acoustic energy leakage in the lateral direction and the substrate [102], as well as the area effect (edge effect) [100]. For example, there is degradation in the measured resonance response near parallel resonance frequencies of 3rd and 5th resonance modes due to spurious resonances. The tolerance in the thicknesses of the fabricated device also contributes to the disagreement between the measurement and the transmission line model. Overall, the results obtained by the transmission line model agree with the measurement results.

As expected from the transmission line model, the highest Q is obtained at the 4th resonance mode. The measured resonance frequency (f_s) at the 4th resonance mode is 1.28 GHz. The K_t^2, Q_s and Q_p at 4th resonance mode are calculated to be *0.0085, 552* and *802,* respectively, using (2.1) and (2.2), and given in Table 2.3. To the best of authors' knowledge, these Qs represent the highest reported values for BST based BAW resonators.

The mBVD model parameters, shown in Figure 2.11 are also provided to better evaluate and understand the device behavior and various loss mechanisms in the device. The extracted mBVD lumped element values and calculated K_t^2 and Qs at the 4th resonance mode are given in Table 2.3. The complex impedance values based on the mBVD model and measurement results near the 4th resonance mode are compared on the Smith chart as seen in Figure 2.24.

Table 2.3 The mBVD model parameters, K_t^2, and Qs at 4th resonance mode

Parameter	Value
C_e	10 pF
C_m	83.3 fF
L_m	185 nH
R_m	1.8 Ω
R_e	0.05 Ω
R_s	0.9 Ω
R_p	2500 Ω
K_t^2	0.0085
Q_s	552
Q_p	802
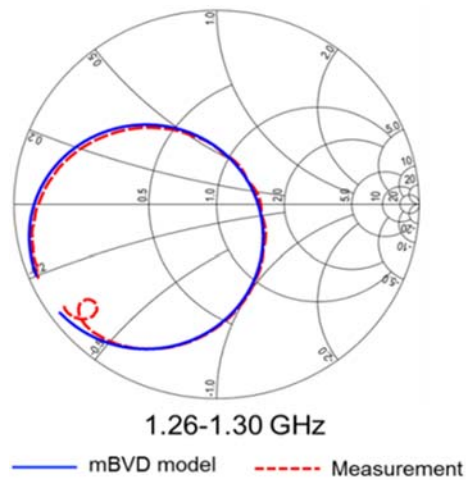
Figure 2.24**:** Comparison of measurement and mBVD model fitting results

The mBVD model at the 4th resonance mode can be utilized in the design of a low-phase-noise oscillator. The required transconductance (g_m) in the active device used in oscillator is proportional to the value of R_m; therefore, a small value for R_m (1.8 Ω as seen in Table 2.3) can significantly reduce the power consumption of the oscillator [101]. The advantage associated with the voltage controlled switchable high-Q resonance response and the low motional resistance make these resonators very suitable in the design of low power consumption, low-phase noise oscillators in future application of frequency-agile communication systems.

Along with the 4th resonance mode, the 5th and 6th modes also exhibit a good resonance performance in terms of K_t^2 and Q. In most of the measured FBARs, the largest K_t^2Q product and largest K_t^2 are obtained at the 5th and 6th resonance modes. Since K_t^2Q is the most important figure in electrically connected FBAR filters, in Chapter 3, the 5th resonance mode of the composite FBARs fabricated on the same chip with the ones presented in this chapter is utilized in the design of an electrically connected filter.

2.8 Conclusion

A high-Q BST based composite FBAR is demonstrated by introducing a low loss single crystalline Si to the FBAR structure. The measured intrinsically switchable FBARs exhibited Qs over 800 with a K_t^2 of 0.0085. The highest Q resonance mode for the intrinsically switchable composite FBARs, such as the one demonstrated in this chapter, is intended for frequency-agile low-phase noise oscillators.

Chapter 3

A 1.5 Stage Intrinsically Switchable, Ladder Type Electrically Connected Filter Based on BST-on-Si Composite Structure

3.1   Introduction

Electrically connected film bulk acoustic resonator (FBAR) filters are the most common type of bulk acoustic wave (BAW) filters used at RF frequencies and extensively used in duplexers for today's mobile phones. By providing steep filter skirts and low insertion loss, electrically connected filters meet the stringent requirements of mobile phone duplexers and occupy a much smaller area as compared to ceramic filters [84].

This chapter discusses the intrinsically switchable ladder type electrically connected filters based on BST-on-Si composite structures. BST's strong voltage induced piezoelectricity at the paraelectric phase is exploited to make these filters switchable. The intrinsically switchable filters discussed in this chapter have the potential for use in

65

complex multiband and frequency-agile communication systems. The filters utilize the composite FBARs that have the same thicknesses with the composite FBARs discussed in Chapter 2.

This chapter is organized as follows: first, the operation principle and design considerations for ladder type electrically connected filters are discussed; then, a 1.5 stage intrinsically switchable ladder type electrically connected filter design is presented; finally the measurement results for a fabricated electrically connected ladder type filter are presented.

3.2 Ladder Type Electrically Connected Filters

3.2.1 Operation Principle

The electrically connected ladder type FBAR filters consist of cascaded series-shunt connected FBAR stages as shown in Figure 3.1. Filter order is determined by the number of stages in the filter. For example, a filter with six FBARs is called a 3-stage or a 3-3 ladder type electrically connected filter [84].
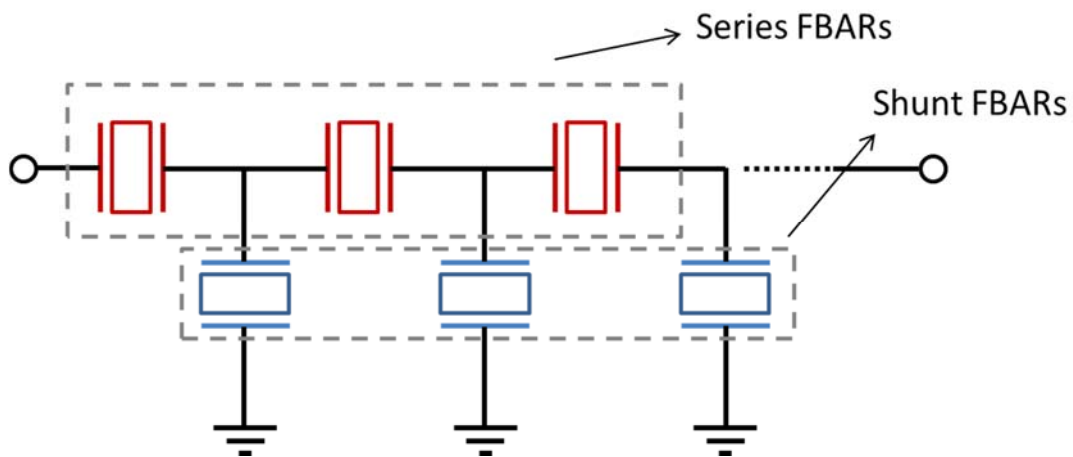
Figure 3.1 : The schematic for the electrically connected ladder type filters

The operation principle of an FBAR filter can be explained by using a typical 1-port composite FBAR impedance response near a resonance mode shown in Figure 3.2. Each composite FBAR exhibits a series and a shunt resonance mode (f_s and f_p). The shunt connected FBARs, shown in Figure 3.1, operate at a slightly lower resonance frequency than the resonance frequency of the series connected FBARs. Therefore, shunt FBAR's parallel resonance frequency is approximately equal to the series resonance frequency of the series connected FBARs (Figure 3.2). With this configuration, one can obtain a minimum insertion between input and output ports, creating a pass band response near the series and the parallel resonance frequencies (f_s^{series} and f_p^{shunt}) of the series and shunt connected FBARs, respectively, as shown in Figure 3.2. This is because, in the pass-band, series FBARs exhibit very low impedance between input and output ports, and the shunt FBARs exhibits very high impedance to the ground (Figure 3.2), providing a low impedance path between input and output ports of the filter.

Since the RF signal is bypassed to ground due to the small impedance of the shunt FBARs at f_s^{shunt}, a transmission zero is created at a slightly lower frequency from the lower edge of the filter's pass-band (at f_s^{shunt}) as shown in Figure 3.2. Similarly, the high impedance of the series connected FBARs at f_p^{series} prevents the RF signal from reaching the output port at the parallel resonance frequency of the series connected FBARs (at at f_p^{series}). This creates a second transmission zero at a slightly higher frequency of the upper edge of the filter pass-band. These two transmission zeros significantly increase the steepness of both the upper and lower filter skirts. As can be seen in Figure 3.2, the steepness performance of electrically connected FBAR filters is directly related to each FBAR's figure of merit (FOM) discussed in Chapter 2.
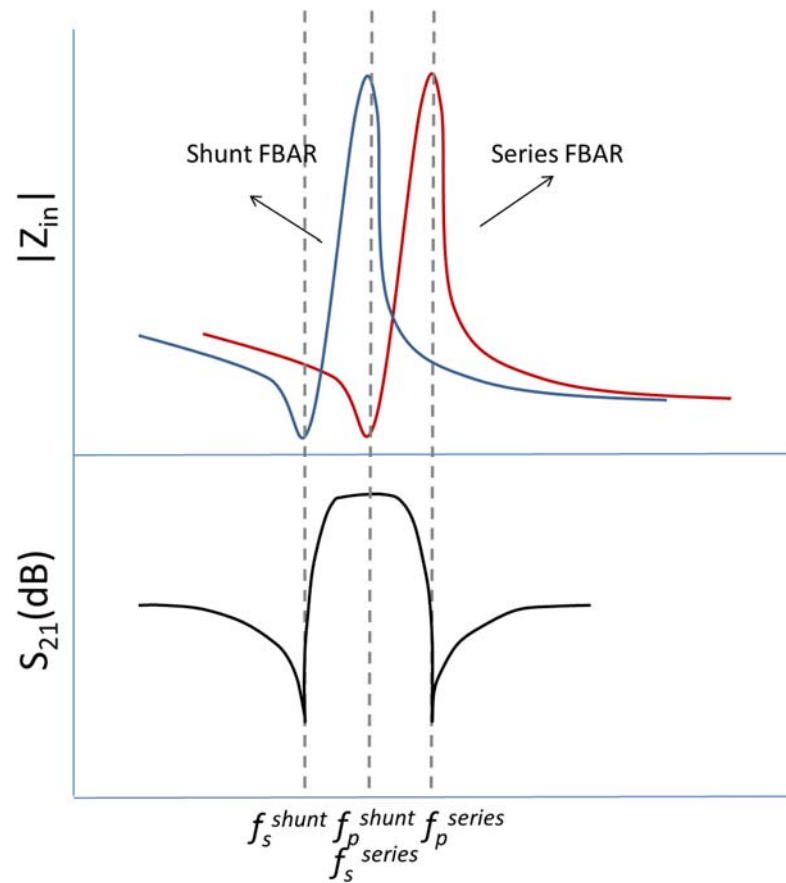
Figure 3.2: An FBAR filter response based on ladder type connected FBARs

The out-of-band rejection for ladder type filters is dependent on the number of stages (series-shunt FBARs) in the filter. Larger number of stages provides higher out-of-band rejection performance at the cost of increased chip area. Another way of increasing the out-of-band rejection level is to utilize larger shunt and smaller series FBARs. This is because each FBAR in the ladder type filter configuration, shown in Figure 3.1, is essentially a capacitor at out-of-band frequencies, creating a ladder type capacitive network. In this network, the higher impedance for the series capacitors and lower impedance for shunt capacitors, respectively, provide a larger isolation between input and

output ports. Manipulating the FBAR areas and increasing the number of stages in tandem is a common practice to improve the out-of-band rejection level for FBAR filters.

The ladder type electrically connected filters can also be implemented using a balanced configuration as shown in Figure 3.3. The balanced FBAR filters exhibit lower bandwidth as compared to unbalanced filters, however, balanced FBAR filters are desired in ICs where balanced amplifiers are utilized [84].
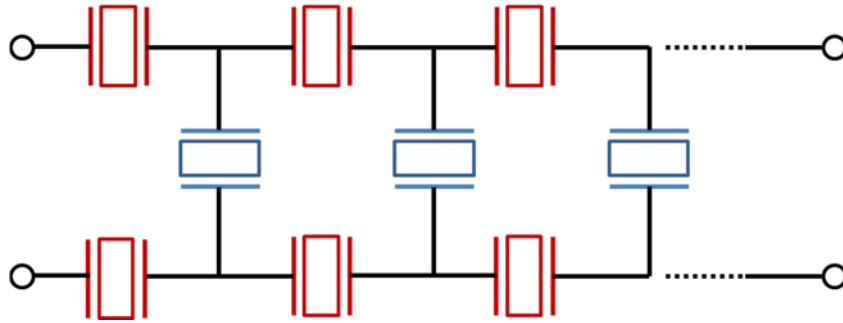
Figure 3.3: Schematic for a balanced ladder type electrically connected FBAR filters

3.2.2   Design Considerations

An FBAR's impedance becomes purely resistive at the series and parallel resonance frequencies (f_s and f_p) defined as R_{fs} and R_{fp} at f_s and f_p, respectively. As discussed in detail in Chapter 2. The filter's insertion loss and roll-off performance (steepness of skirts) is strongly dependent on the R_{fs} and R_{fp} of the FBARs used in the filters [51, 84, 91, 103]. As can be seen in Figure 3.2, a filter's insertion loss is determined by the impedances at the series resonance frequency of the series FBARs (f_s^{series}) and parallel resonance frequency of the shunt FBARs (f_p^{shunt}); therefore, providing smaller R_{fs} and larger R_{fp} values for series and shunt FBARs is a key requirement for obtaining a low insertion loss.

The filter's skirt steepness is also dependent on R_{fs} and R_{fp} of the FBARs. As can be seen in Figure 3.2, a smaller R_{fs} for the shunt FBARs at f_s^{shunt} provides steeper filter skirt

below the pass band. Similarly, a larger R_{fp} for the series FBARs at f_p^{series} provides a steeper filter skirt above the pass band. Therefore, for a good filter performance in terms of insertion loss and steepness of the skirt, smaller R_{fs} and larger R_{fp} values are highly desirable in the FBARs used in electrically connected filters.

The values of R_{fs} and R_{fp} are directly related to the size of resonance circles of the FBARs on Smith chart. The resonance circle size increases and approaches to the edge of the Smith chart with increasing $K_t^2 Q$ product as discussed in Chapter 2. Figure 2.8 in Chapter 2 shows the resonance circles, obtained from the transmission line model, for various $K_t^2 Q$ products. The extracted R_{fs} and R_{fp} from the FBAR impedance response for as a function of $K_t^2 Q$ product is shown in Figure 2.10. As can be seen in Figure 2.10, smaller R_{fs} and larger R_{fp} are obtained with larger $K_t^2 Q$ product. This shows that the $K_t^2 Q$ product for the FBARs is needed to be as high as possible for a good filter performance in terms of insertion loss and skirt steepness.

3.3 A 1.5 Stage Intrinsically Switchable Electrically Connected Filter Based on BST-on-Si Composite Structure

The intrinsically switchable FBARs based on BST-on-Si composite structure are already discussed in Chapter 2. In this section, a 1.5 stage electrically connected ladder type filter is designed using these composite FBARs. A higher order resonance mode that exhibits the largest $K_t^2 Q$ product is utilized to obtain a good filter performance in terms of insertion loss and skirt steepness. Based on the measurement results for composite FBARs, 5th and 6th resonance modes provide the largest $K_t^2 Q$ and K_t^2 values, respectively. Therefore, the 5th resonance mode was chosen when designing intrinsically switchable electrically connected FBAR filters.

The schematic and bias configuration for the 1.5 stage intrinsically switchable ladder type electrically connected filter is shown in Figure 3.4. The filter consists of a shunt composite FBAR connected in between two series composite FBARs (Figure 3.4). Each composite FBAR needs to be biased, due to their voltage induced piezoelectric effect. To switch the filter on & off, a DC bias is applied between the top and the bottom electrodes (across BST layer) of each composite FBAR in the filter. A DC bias voltage connected at the middle point in the schematic can bias all the FBARs as shown in Figure 3.4. This bias point corresponds to the bottom electrodes for the FBARs in the fabricated filters. The DC bias voltage is applied through a high resistivity bias line to prevent RF leakage. The top electrodes of the series FBARs are connected to the input and output ports of the filter. At the same time, they are grounded through the bias tees connected at the input and output ports as shown in Figure 3.4. The top electrode of the shunt FBAR is connected to RF ground as shown in Figure 3.4.

To predict the filter performance, the electric impedance of series and shunt composite FBARs (Z_{series} and Z_{shunt}) shown in Figure 3.4 is simulated using the 1-D acoustic transmission line model discussed in Chapter 2. Then, filter insertion loss and return loss is calculated by determining the ABCD network parameters using Z_{series} and Z_{shunt} in Figure 3.4, and converting to S-parameters. ABCD parameters for the filter shown in Figure 3.4 are calculated using (3.1)-(3.4) [104]. The return-loss (S_{11}) and insertion-loss (S_{21}) of the filter, for a 50 Ω port impedance can be calculated from the ABCD parameters using (3.5)-(3.7) [104]. The matlab codes for calculating the resonator impedances (Z_{series} and Z_{shunt}), the ABCD matrix and the S-parameters (S_{11} and S_{21}) are given in Appendix B.
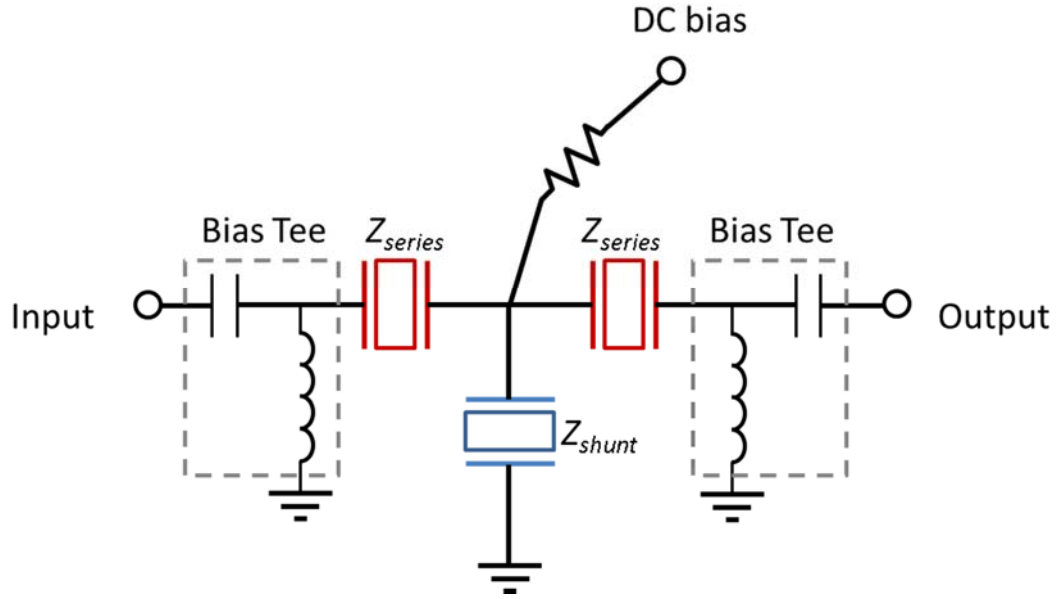
Figure 3.4: Schematic for an intrinsically switchable 1.5 stage ladder type electrically connected filter. Z_{series} and Z_{shunt} represents the electric impedance of series and shunt resonators, respectively

$$A = 1 + \frac{Z_{series}}{Z_{shunt}} \tag{3.1}$$

$$B = 2Z_{series} + \frac{(Z_{series})^2}{Z_{shunt}} \tag{3.2}$$

$$C = \frac{1}{Z_{shunt}} \tag{3.3}$$

$$D = 1 + \frac{Z_{series}}{Z_{shunt}} \tag{3.4}$$

$$\vartriangle = A + \frac{B}{50} + C \cdot 50 + D \tag{3.5}$$

$$S_{11} = \frac{A + \dfrac{B}{50} - C \cdot 50 - D}{\vartriangle} \tag{3.6}$$

$$S_{21} = \frac{2 \cdot (A \cdot D - B \cdot C)}{\Delta}$$

(3.7)

Based on transmission line model simulations above, the series and shunt FBARs with areas of 1050 x 10^{-12} m^2 and 2300 x 10^{-12} m^2, respectively, are chosen for the filter. In these simulations the resonance frequency of the shunt composite FBARs are slightly reduced by increasing the thickness of the top gold (Au) layer by 20 nm. The input impedance for the series and shunt FBARs is shown in Figure 3.5 (a). The filter's simulated return loss and insertion loss are shown in Figure 3.5 (b) at 5th resonance mode with a center frequency of 1.67 GHz. During the fabrication of these filters, a separate deposition and lift-off step is needed to add a 20 nm thick layer of Au on the shunt composite FBARs.

As shown in Figure 3.5, the predicted filter insertion loss and return loss are 2.5 dB and 18 dB, respectively. The simulated dB bandwidth (BW) is approximately 11 MHz (0.66 %). The filters are fabricated on the same chip with the intrinsically switchable BST-on-Si composite FBARs presented in Chapter 2. Therefore, the fabrication steps are exactly the same as those of composite FBARs shown in Figure 2.20.
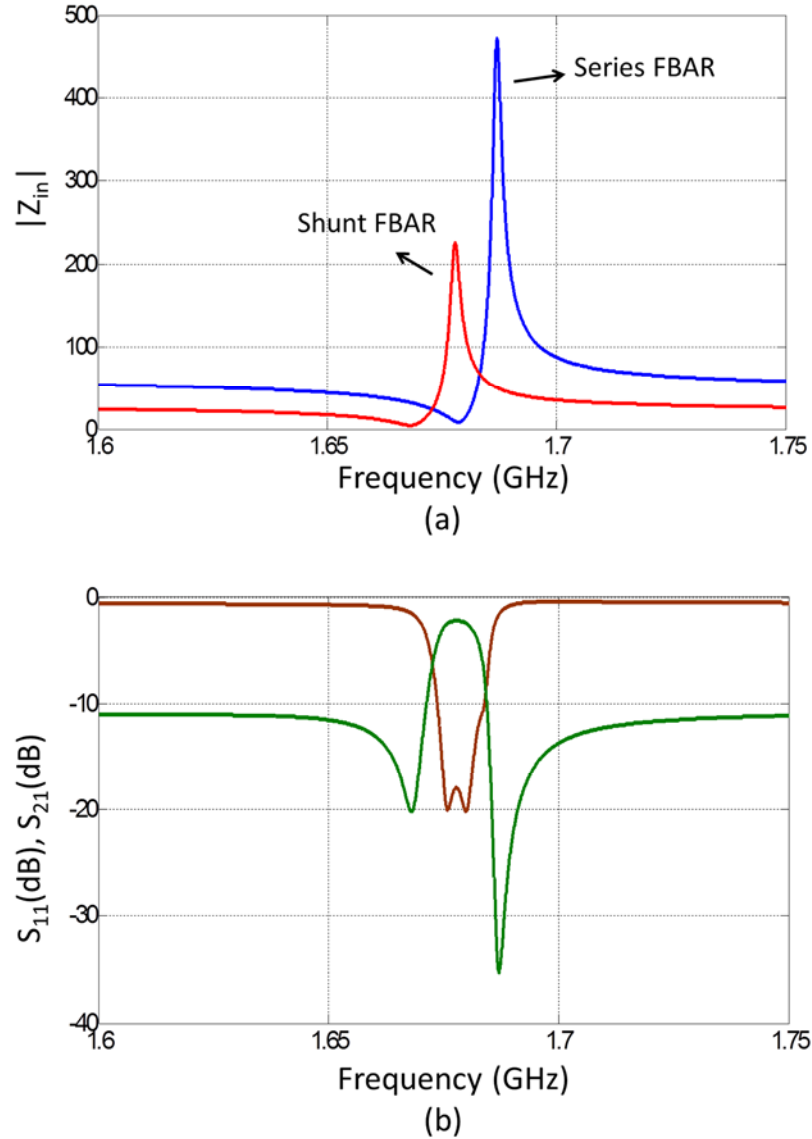
Figure 3.5: (a) Simulated input impedance for series and shunt FBARs, (b) Simulated insertion loss and return loss for the filter. Simulations are performed at 5th resonance mode

3.4 Measurement Results

Figure 3.6 shows a microphotograph of a fabricated intrinsically switchable 1.5 stage ladder type electrically connected filter based on a BST-on-Si composite structure. The fabricated filters are measured with Cascade Microtech's 150 μm pitch size ground-

signal-ground (GSG) RF probes using an Agilent E8364C PNA network analyzer. The measurement set up is calibrated using short-open-load-thru (SOLT) calibration standards on a Cascade Microtech's impedance standard substrate (ISS). During the measurement, the DC bias voltage (V_{dc}) is applied to the bottom electrode through a high resistance bias line. The top electrodes for the series FBARs are connected to a DC ground using bias tees at the ports. The bias voltage is increased gradually from 0 V to 30 V until the input impedance no longer varies with the bias voltage due to the saturation of the voltage-induced electric polarization in the BST layer [78]. Further increase in the DC bias voltage after saturation (e.g 40 V) may result in dielectric breakdown. It should be noted that the break-down voltage depends on the BST thickness. The measured BST thickness near a measured filter was approximately 550 nm.

The measured return loss and insertion loss of a device for 0 V (off) and 30 V (on) DC bias is shown in Figure 3.7. Since the piezoelectric coefficient is zero, there is no electromechanical transduction at 0 V dc bias. Therefore, the device acts as a capacitive tee network exhibiting the insertion loss and return loss response as shown in Figure 3.7 (a). Approximately 15 dB isolation is obtained between the input and output ports with 0 V DC bias.

The electromechanical transduction turns with the application of DC bias voltage due to voltage induced piezoelectric effect. The measured filter response at the 5th resonance mode is shown in Figure 3.7 (b) for 30 V dc bias. The measured insertion loss and return loss of the filter are 4.5 dB and more than 15 dB in the pass band, respectively. The filter's 3dB bandwidth is 9 MHz (0.56 %) and out-of-band rejection level is approximately 8 dB.

The filter's center frequency is slightly lower than that of simulated filter response shown in Figure 3.5 (b). This is attributed to tolerance in the thicknesses of the fabricated device and inaccuracy of the acoustic properties used in the model. The filter's insertion loss and 3dB BW are also slightly reduced as compared to simulation results. This can be attributed to difference in Q, K_t^2 and resonance frequency of the simulated and measured FBARs.
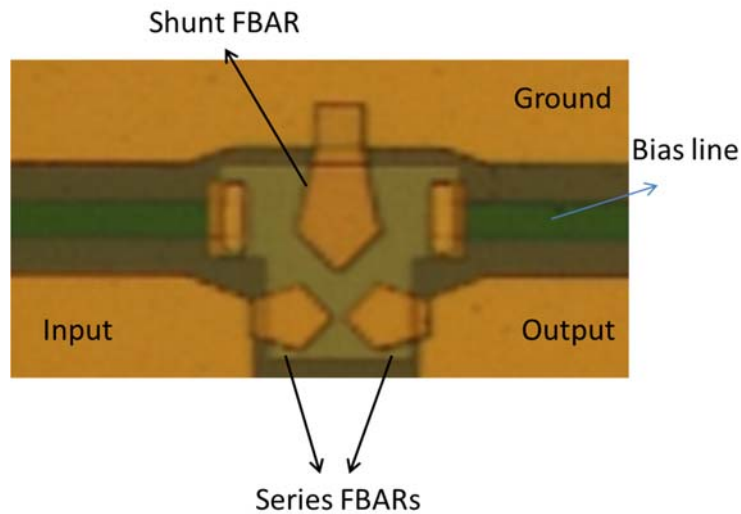
Figure 3.6: The microscope photo of a measured intrinsically switchable 1.5 stage ladder type electrically connected filter based on BST-on-Si composite structure

The wide band insertion loss of the filter is shown in Figure 3.8. As expected, the 5th resonance mode exhibits the best filter response, in terms of insertion loss.
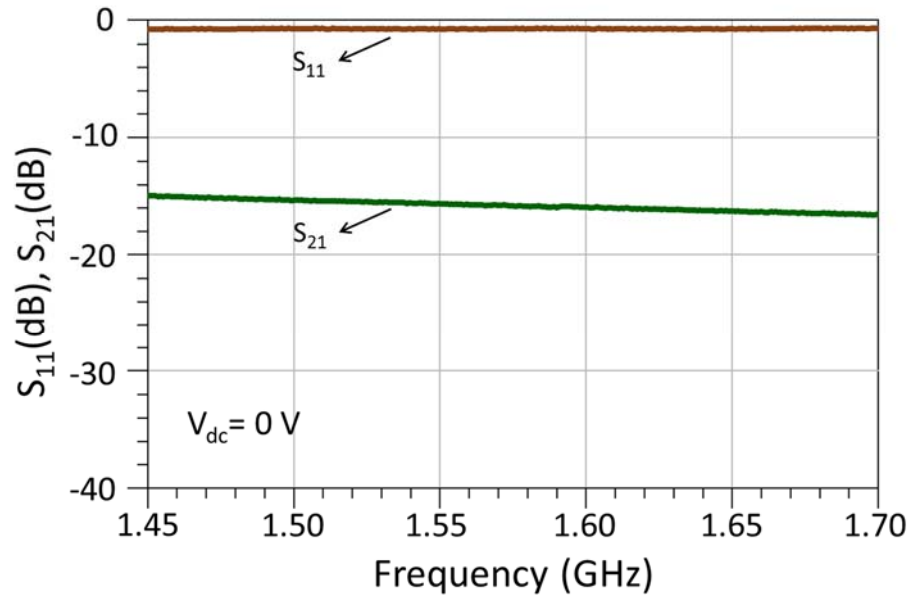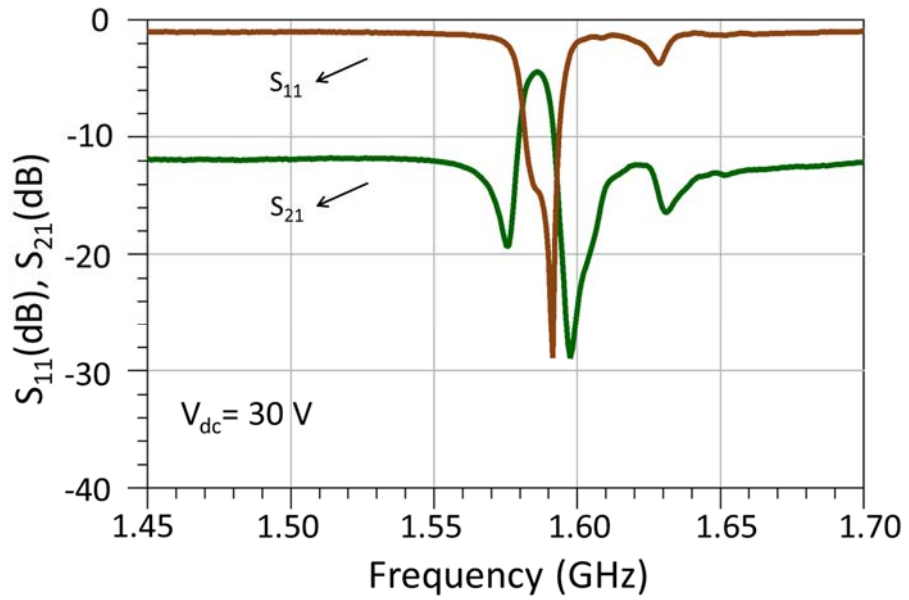
Figure 3.7: The measured return loss and insertion loss for (a) 30 V DC bias (filter is on), and (b) 0 V DC bias (filter is off)
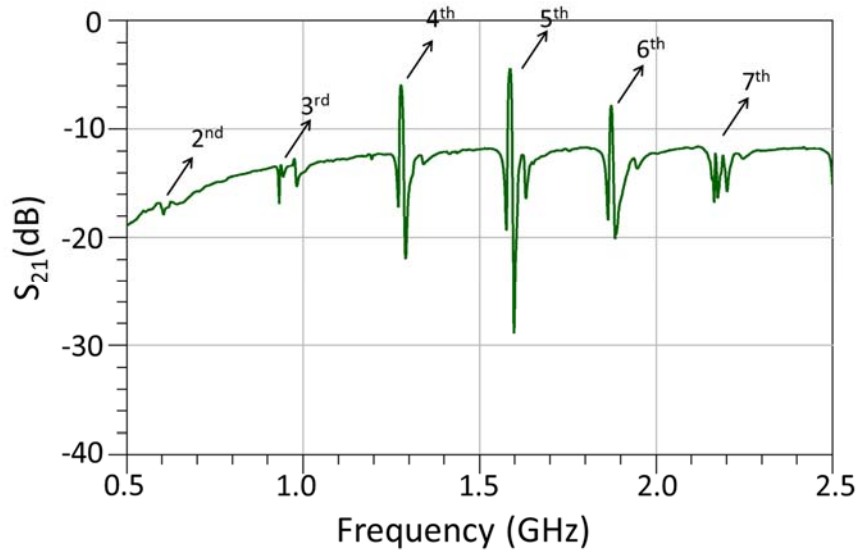
Figure 3.8: Wide band measured insertion loss of the filter

3.5 Conclusion

An intrinsically switchable ladder type electrically connected filter is demonstrated utilizing BST-on-Si composite structure. The choice of appropriate mode of operation for the composite FBARs is discussed by detailed explanation on the operation principles and design considerations in electrically connected filters.

Chapter 4

An Intrinsically Switchable, Laterally Coupled Acoustic Filter Based on BST-on-Si Composite Structure

4.1 Introduction

BAW filters are classified as electrically or acoustically coupled based on the type of coupling between the resonators used in the filters. The electrically connected filters are the most commonly available BAW filters used in RF applications and were discussed in detail in Chapter 3. This chapter describes operating principles and structures for the acoustically coupled filters. Particularly, the intrinsically switchable laterally coupled acoustic filters based on BST-on-Si composite structure are described in detail, and the measurement results for such filters are presented in this chapter.

In acoustically coupled filters, the resonators are coupled either vertically or laterally depending on the resonator structure [84, 105]. In vertically coupled filters, the resonators are stacked on top of each other such that the acoustic coupling is perpendicular to resonator surfaces. Stacked crystal filters (SCFs) and coupled resonator filters (CRFs) are examples of vertically coupled acoustic filters [84, 106-109]. In laterally coupled acoustic filters, the resonators are fabricated on the same plane, and are separated by a gap between the electrodes. In such filters, the acoustic coupling takes place in lateral

direction parallel to the resonator surfaces. Monolithic crystal filters (MCF) are one of the first BAW filters to utilize lateral coupling and have been used since 1960s for various applications such as intermediate frequency (IF) filters in radios [110-112]. The quartz crystals have been the material of choice in traditional MCFs.

Recently, laterally acoustically coupled filters have been implemented using thin film piezoelectric materials, such as AlN and zinc oxide (ZnO) [105, 113-117]. Due to their much thinner thicknesses, thin film laterally coupled acoustic filters operates at much higher frequencies as compared to MCFs, making them suitable for the RF & microwave applications.

This chapter presents the thin film intrinsically switchable laterally acoustically coupled filters based on BST-on-Si composite structure. First, detailed description of vertically acoustically coupled and laterally acoustically coupled filters is provided. A lumped element model that represents the laterally acoustically coupled filters is given. Subsequently, the effect of device geometry on the performance of the intrinsically switchable laterally acoustically coupled filters is studied using finite element simulations. Finally, the fabrication steps and measurement results for intrinsically switchable laterally coupled acoustic filters are presented.

4.1.1 Vertically-Coupled-Acoustic Filters

Vertically coupled acoustic filters consist of multiple resonators stacked on top of each other. There are two types of vertically coupled filters: stacked crystal filters and coupled resonator filters [84, 107, 108]. The two-resonator (one-pole) stacked crystal filter configuration is shown in Figure 4.1. The input and output ports are connected to the top and the bottom electrodes. The electrode shared between the top and the bottom

piezoelectric layers serves as an electrical ground. The RF signal applied between the top and the middle electrodes excites an acoustic wave via the inverse piezoelectric effect within the top piezoelectric layer. The acoustic wave then propagates to the bottom resonator where the bottom electrode surface acts as an acoustic reflector. Therefore, an acoustic cavity is created by the top and bottom electrode-air interfaces.
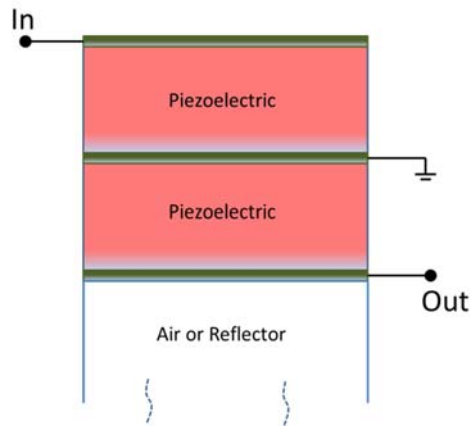
Figure 4.1: A one-pole stacked crystal filter configuration [84, 107, 108].

The acoustic wave is converted in to RF signal by the bottom resonator via the direct piezoelectric effect. This structure provides a one-pole narrowband band-pass filter response. The intensity of coupling between electric and acoustic energy is a function of the piezoelectric coefficient (electromechanical coupling coefficient of the piezoelectric layer) as well as the acoustic displacement across the piezoelectric layers. Since a half-wavelength acoustic displacement provides the largest electromechanical coupling in a transduction layer, the stacked crystal filters exhibit the widest bandwidth at the 2nd resonance mode where the overall resonator structure is one acoustic wavelength thick [84]. Figure 4.2 shows the acoustic displacement across piezoelectric layers at the fundamental and second resonance modes.

a) Fundamental mode   b) Second mode
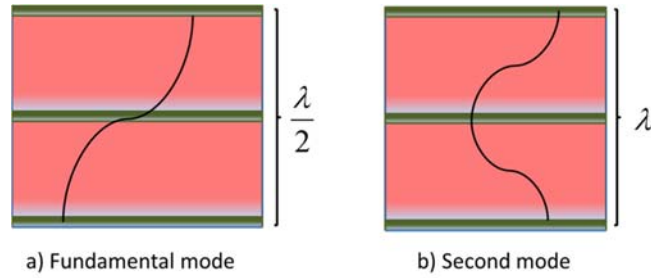
Figure 4.2: Acoustic displacement across the piezoelectric layers in stacked crystal filters for (a) fundamental mode, (b) second mode.

Filter order can be increased by connecting multiple 1-pole SCFs in series. Figure 4.3 shows a two-pole SCF which consists of two series connected one-pole SCFs [84, 107, 108].
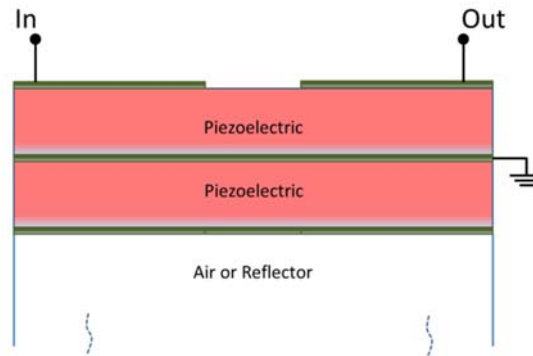
Figure 4.3: A two-pole stacked crystal filter configuration.

Another type of vertically acoustically coupled filter is a coupled resonator filter (CRF). In CRFs, coupling layers are introduced between the top and the bottom resonators as shown in Figure 4.4. The coupling layers reduce the acoustic coupling between top and bottom resonators such that the top and bottom resonators perform as two independent resonators. Such a structure can provide a two-pole filter response by controlling the thicknesses of the coupling layers. Similar to stacked crystal filters,

connecting 2 CRFs in series increases the filters order. Figure 4.4 shows a two-pole (a) and a four-pole (b) coupled resonator filter configurations.
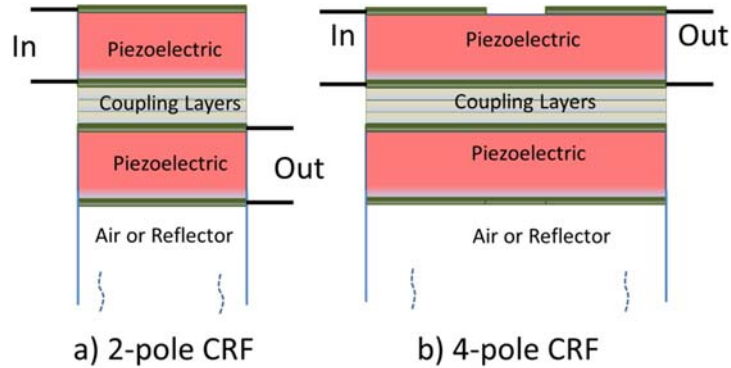
Figure 4.4**:** a) two-pole and b) four-pole coupled resonator filter configurations.

4.1.2 Laterally-Coupled-Acoustic Filters

In laterally coupled acoustic filters, the resonators are coupled in a direction perpendicular to the electrode surfaces. The traditional quartz based monolithic crystal filters (MCFs) utilize acoustic coupling in lateral direction and are employed in thin film laterally acoustically coupled filters operating at RF frequencies [115, 118].

MCFs utilize lamb waves, which are horizontally propagating thickness extensional (TE) or thickness shear (TS) plate waves [105, 113, 114, 116, 117]. There exist symmetric and anti-symmetric lamb waves for a stack of layers [105, 116, 117]. Figure 4.5 illustrates the typical acoustic displacement for symmetric and anti-symmetric lamb waves utilized in a two-resonator monolithic crystal filter. The resonance frequencies of the symmetric and anti-symmetric lamb wave modes are close enough that by carefully patterning the electrodes with appropriate layer thicknesses, a coupled resonator filter can be designed. It should be noted that the plate waves (or lamb waves) utilized in the MCFs

83

are usually accepted as spurious modes in FBAR resonators and filters discussed in Chapter 2 and Chapter 3 [84].

The operation of MCFs can be explained by dividing the MCF structure into three regions as shown in Figure 4.5. The RF signal at the input port (region 1) excites a lamb wave mode (symmetric and ant-symmetric) acoustic wave through the inverse piezoelectric effect of the piezoelectric layer (e.g quartz crystal). A standing wave is established between the surfaces of the top and the bottom electrodes due to air-electrode boundaries. Since the resonance frequencies of region 1 and region 2 are different, the standing wave excited at the input resonator (region 1) becomes evanescent at region 2 and cannot propagate into region 3. However, the acoustic energy couples into region 2 with an exponential decay, and excites the output resonator [110, 111]. The acoustic wave at the output resonator is then converted back to RF signal via the direct piezoelectric effect of quartz crystal.

For the symmetric lamb wave mode, the acoustic wave at the input and output resonators are in-phase. However, there is a 180º phase difference between the input and output ports (out-of-phase) for the anti-symmetric lamb-wave mode as shown in Figure 4.5.

In MCFs, the extent to which acoustic energy is transmitted from the input to the output port is related to the amount of exponential decay in region 2 [110, 111]. The exponential decay in region 2 is a function of the difference between the resonance frequencies of regions 1,3 and region 2 (plate-back), the separation between electrodes and the lateral geometry of the electrodes [110, 111]. Therefore, inter-resonator coupling can be controlled by carefully designing the MCF geometry.
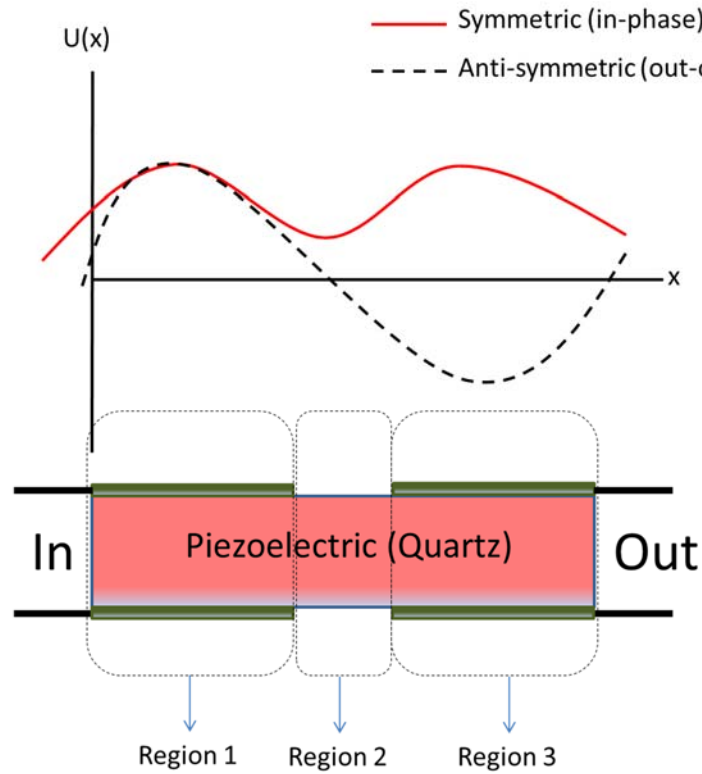
Figure 4.5: A traditional two-resonator monolithic crystal filter. Symmetric and anti-symmetric lamb wave modes are shown as a function of lateral dimension (x)

The thin film laterally coupled acoustic filters that were recently demonstrated at RF frequencies are similar to MCFs except they use thinner layer of piezoelectric materials like AlN. The thin film laterally coupled acoustic filters are fabricated on low-loss substrates such as single-crystalline silicon using thin film deposition techniques. Figure 4.6 illustrates the most common configurations for thin film laterally coupled acoustic filters.

a) Air interface at the bottom electrode   b) Bragg reflector interface at the bottom electrode
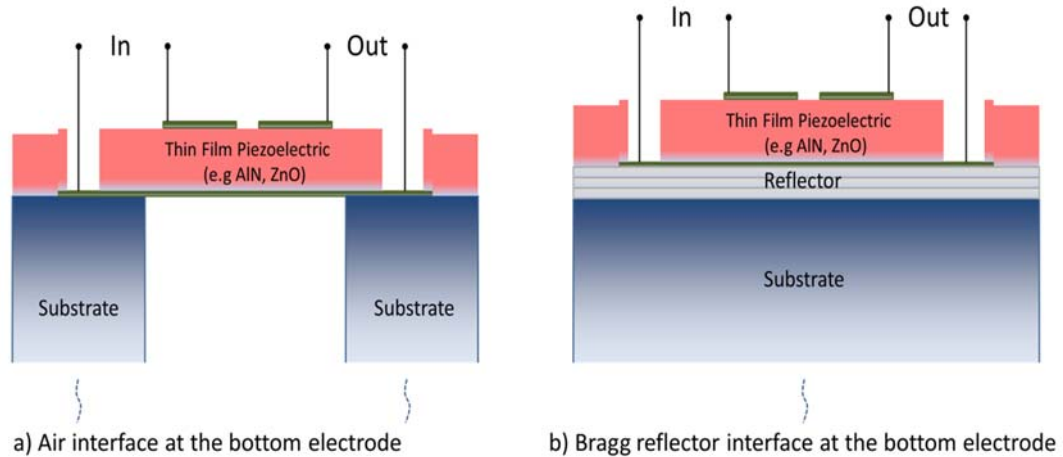
Figure 4.6: Laterally coupled thin film acoustic filters fabricated on silicon substrate. (a) The device is released from the bottom of the substrate by removing the Si underneath (b) or a Bragg reflector is utilized between substrate and bottom electrode.

The thin film laterally coupled acoustic filters can also be implemented using a composite structure [115-118]. The intrinsically switchable acoustically coupled filters discussed in this chapter are based on the BST-on-Si composite structure that is similar to composite FBARs explained in Chapter 2. The following sections present the structure, modeling, simulation results, fabrication steps and measurement results for intrinsically switchable BST-on-Si laterally coupled acoustic.

4.1.3 Intrinsically Switchable Laterally Coupled Acoustic Filters based on BST-on-Si structure

Thin film ferroelectric BST along with the top and the bottom electrodes are deposited on a (100)-oriented single crystalline high resistivity, low-loss Si membrane. Because of the BST's voltage induced piezoelectric effect, the filters can be controlled with the application of DC bias voltage. The low mechanical loss Si layer in the composite structure is expected to increase the Q of the resonators in the filter. At the same time,

86

such devices are mechanically robust and less susceptible to stress related deformations. Similar to the composite FBARs, the laterally coupled acoustic filters presented in this chapter should operate at higher order modes to achieve large electromechanical couplings.

It has been reported that interdigitated electrode configuration can improve the performance of thin film laterally acoustically coupled filters by providing an increased bandwidth and reduced spurious modes [113, 115-117].. Figure 4.7 shows the 3-D and cross-sectional view of a laterally acoustically coupled filter based on BST-on-Si composite structure. A DC bias is applied along with RF an signal to turn on the electromechanical transduction via voltage induced piezoelectric effect.

The filters discussed in this chapter are fabricated on a 5 μm thick Si membrane. The thickness of the BST layer is determined using the 1-D acoustic transmission line model discussed in Chapter 2. Based on 1-D acoustic transmission line model, a 2.5 μm thick BST is chosen to provide a large K_t^2 at the second resonance mode with a resonance frequency of approximately 750 MHz. The thicknesses of the stacked layers shown in Figure 4.7 are given in Table 4.1.

Table 4.1 The thicknesses of the stacked layers in BST-on-Si composite structure

Material	Thickness (μm)
Top Electrode (Pt)	0.1
BST	2.5
Bottom Electrode (Pt)	0.15
SiO$_2$	0.2
Si	5
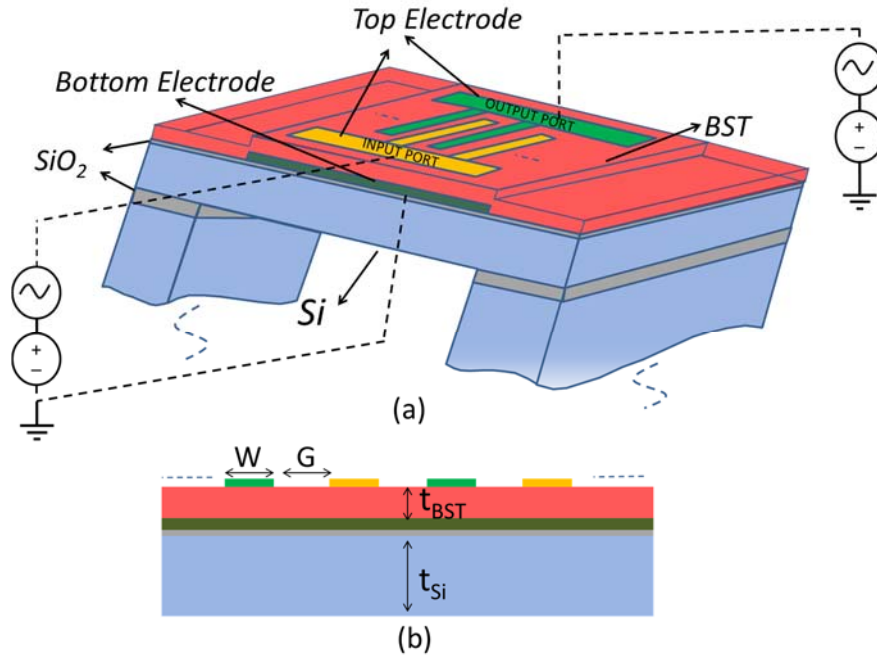
Figure 4.7: (a) 3-D and (b) cross-sectional view of acoustically coupled filters with interdigitated top electrodes

After determining the optimum thicknesses of Si membrane and BST transduction layer, the effect of lateral geometry on the filter performance is studied using commercially available FEM simulation software. This will be discussed later in this chapter; however, before discussing the FEM simulation results, the typical electrical response and a lumped element model for laterally coupled acoustic filters is described for better understanding of the filter characteristics. The following section discusses the lumped element model that was originally used in traditional MCFs. The same model is also used for thin film laterally coupled acoustic filters [117].

4.2 Lumped Element Model and Electrical Response for Laterally Coupled Acoustic Filters

The mBVD model shown in Figure 4.8 (a) is used to represent BAW resonators such as the composite FBARs discussed in Chapter 2. By using a suitable coupling element, two mBVD circuits can be used to model laterally coupled acoustic filters discussed in previous sections [110, 112]. The mechanical motion or vibrating mass of a resonance structure is electrically equivalent to an inductor. Since the coupling between resonators in laterally acoustically coupled filters is via the mechanical motion at the region between the resonators, the inter-resonator coupling can be represented by two coupled inductors (transformer) [112]. Therefore, the two mBVD circuits can be coupled through a transformer as shown in Figure 4.8 (b), providing a lumped element model for the laterally acoustically coupled filters. The amount of inter-resonator coupling can be controlled by the mutual inductance (M) in Figure 4.8 (b). To further simplify the model, the transformer shown in Figure 4.8 (b) can be replaced with an inductive T-equivalent circuit with element values that include the effect of the mutual inductance [111]. Figure 4.9 shows the simplified laterally acoustically coupled filter lumped element model. This model can be used to analyze the filter electrical response and distinguish the effect of various loss mechanisms on its performance. In Figure 4.9, the R_m in combination with L_m and C_m represents the mechanical Q at each resonator. The C_e represents the parallel plate capacitance formed by the electrodes and the transduction layer (BST). The resistors R_p, R_s, and R_e account for electrical losses. The R_s represents the resistive losses associated with electrodes, and the R_e and the R_p represent the dielectric losses associated with the transduction layer. The C_f represents the feed-thru capacitance between

resonators and it is usually much smaller than the static capacitance of the resonators (C_f << C_e).
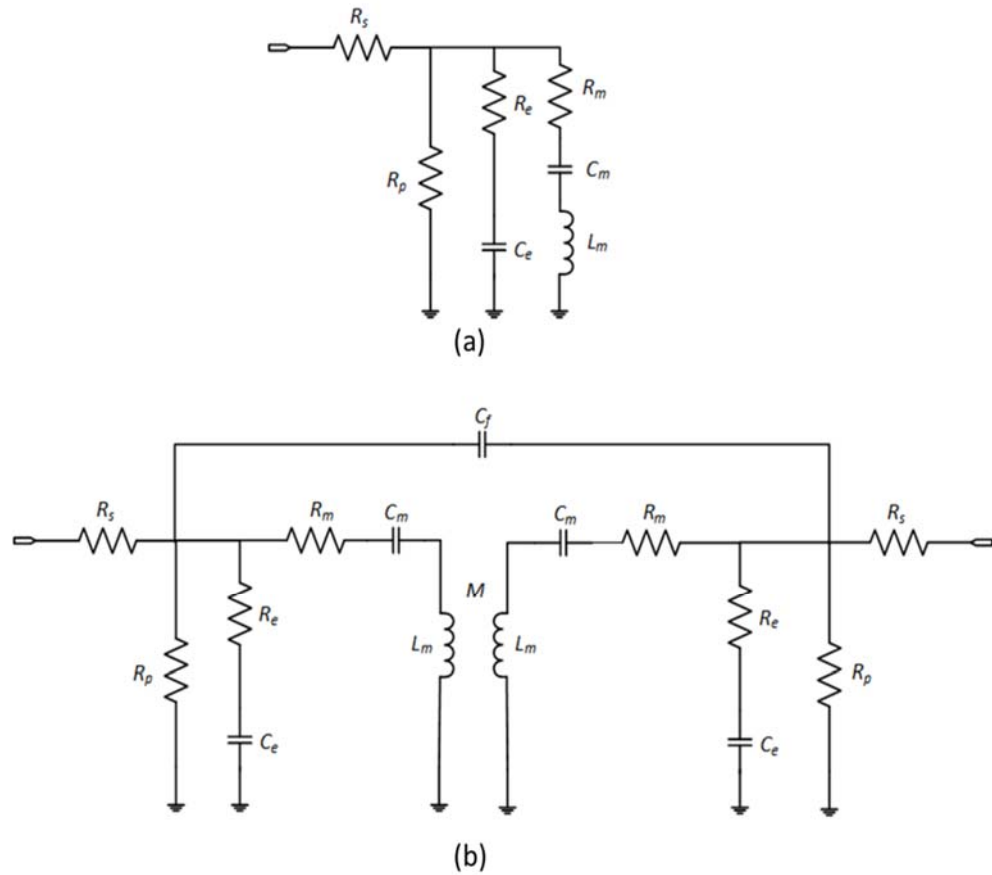
Figure 4.8: Lumped element models for (a) a single resonator and (b) a filter with acoustically coupled resonators
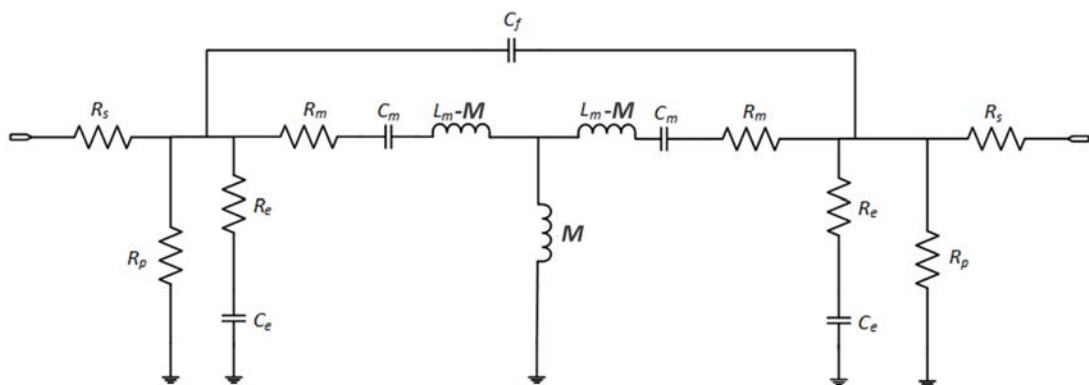
Figure 4.9: Lumped element model for the laterally coupled acoustic filter. The inter-resonator coupling is represented by inductive-T.

The amount of acoustic coupling between the resonators is quantified by the inter-resonator coupling coefficient (k) and is related to the mutual inductance in the lumped element model by the following formula [111]:

$$k = \frac{M}{\sqrt{L_m L_m}} = \frac{M}{L_m}.$$

(4.1)

Using the model shown in Figure 4.9, typical insertion loss (S_{21}), return loss (S_{11}) and short circuit input admittance (Y_{11}) plots for a laterally acoustically coupled filter are shown in Figure 4.10. The inter-resonator coupling coefficient given in (4.1) can be calculated from the filter's electrical response as follows [110, 111]:

$$k = \frac{2(f_b - f_a)}{(f_b + f_a)}$$

(4.2)

where f_a and f_b are the frequencies that correspond to peaks of the $|Y_{11}|$ as shown in Figure 4.10.

In acoustically coupled filters the inter-resonator coupling coefficient (k) is used to control the filter bandwidth (BW) and insertion loss characteristic such as in-band ripple level. Resonators can be under coupled, critically coupled or over coupled as shown in Figure 4.11 [84]. If the resonators are under coupled, a larger insertion loss and narrower bandwidth is obtained [84]. If they are over coupled, the filter's BW increases; however, filter's in-band response is degraded in terms of its flatness of the insertion loss and group delay [84]. Usually, filter geometry is optimized for critical coupling to obtain a flat insertion loss and group delay. The optimum inter-resonator coupling coefficient (k) depends on the desired filter response, input and output port impedances as well as resonator Qs.
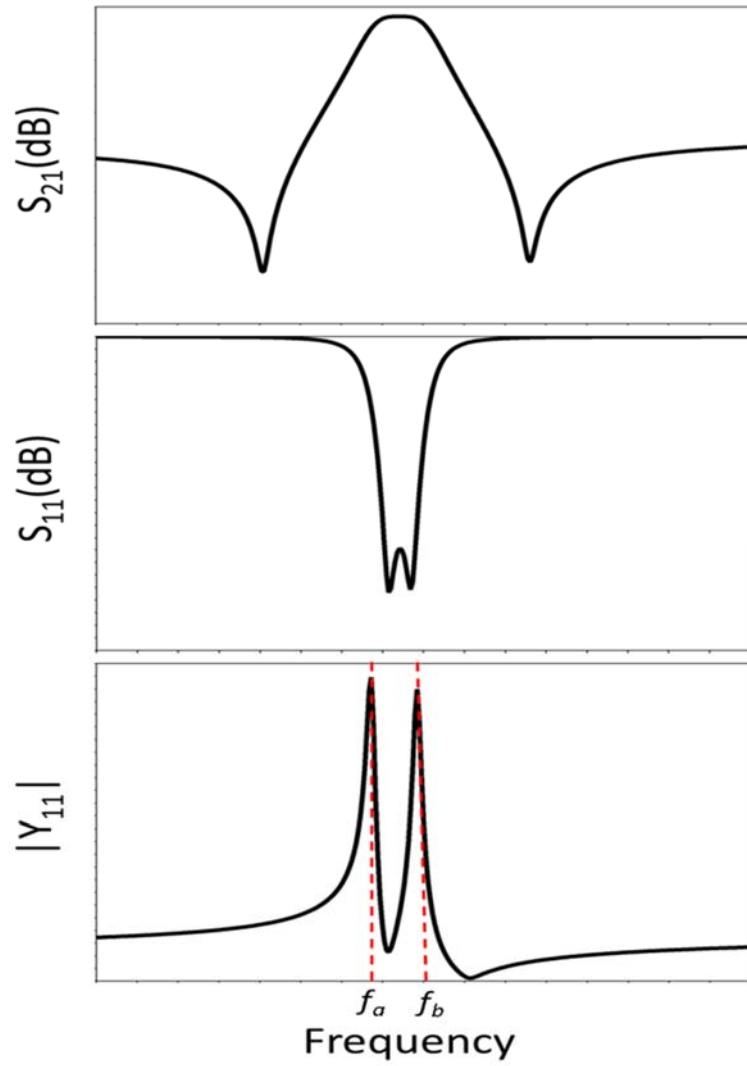
Figure 4.10: A typical electrical response for a laterally acoustically coupled filter. From top to bottom, plots are S_{21}, S_{11} and Y_{11}, respectively.
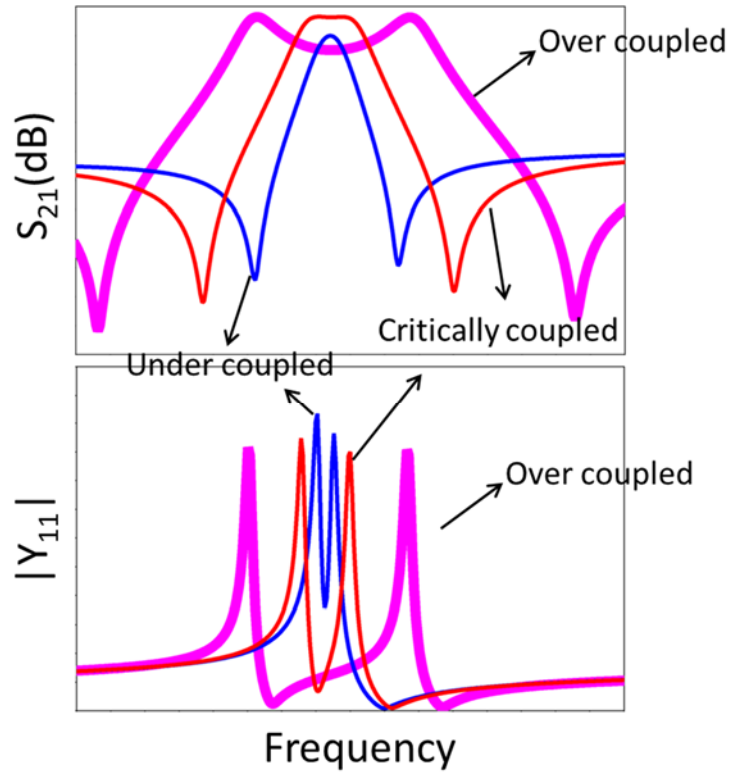
Figure 4.11**:** The effect of inter-resonator coupling on the filter insertion loss

The lumped element model for acoustically coupled filters shown in Figure 4.11 can be converted into a general ladder type band-pass filter prototype circuit using suitable transformations [110, 112]. MCF designers have been utilizing the lumped element model with suitable transformations to design MCF's geometry for a desired electrical response. This is very practical when designing quartz based MCFs; because bulk quartz crystal is very well-characterized material in terms of its acoustic and piezoelectric properties. However, the thin film ferroelectric BST's acoustic and piezoelectric properties have not been fully characterized. Furthermore, these properties are dependent on the deposition conditions for the thin films. Therefore, in this work, the lumped element model discussed above is primarily used for understanding the typical filter electrical response and analyzing the measurement results.

An important advantage of acoustically coupled filters is their larger out of band rejection level as compared to electrically connected filters (FBAR filters). This is due to very-high isolation between input and output ports in acoustically coupled filters. Figure 4.12 shows the resonator configurations for a 1.5 stage (3 resonators) ladder type electrically connected filter (FBAR filter) and a two resonator laterally acoustically coupled filter. The acoustic coupling between the resonators is represented by an inter-resonator coupling coefficient (k) as shown Figure 4.12 (b). The resonators in both electrically connected and acoustically coupled filters are essentially parallel plate capacitors at the frequencies away from the resonance frequencies. Therefore, the electrically connected and laterally acoustically coupled filters shown Figure 4.12 (a), (c) can be represented by capacitive-T and capacitive-π circuits as shown in Figure 4.12 (b) and (d), respectively. Note that, it is assumed that the resonators have the same parallel plate capacitance (C_e) in Figure 4.12 (c) and (d), for the sake of simplicity.

As shown in Figure 4.12 (b), there is a direct path between input and output ports of the electrically connected filter through the parallel plate capacitance (C_e) of the resonators. On the other hand, for laterally acoustically coupled filter, the RF signal path between the input and output port is through the feed-thru capacitance (C_f) which is much smaller than the parallel plate capacitance (C_e) of the resonators. Therefore, the isolation between input and output ports is much higher in acoustically coupled filters as compared to electrical connected filters.

(a) FBAR filter at f_r (b) Acoustically coupled filter at f_r

(c) FBAR at away from f_r (d) Acoustically coupled filter at away from f_r
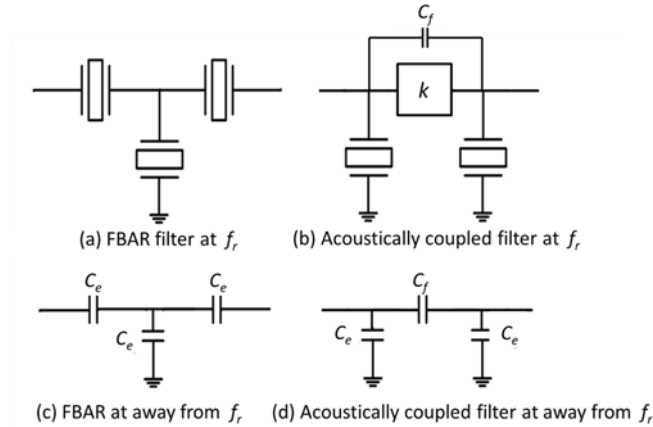
Figure 4.12: The schematic for electrically connected and laterally coupled acoustic filters at the resonance and away from the resonance frequencies

4.3 Study of Geometry Effects on the Laterally Coupled Acoustic Filters Using FEM Simulations

The performance of the laterally acoustically coupled filters strongly depends on the filter geometry [105, 113]. For example, in the composite filters, the thicknesses for the BST and Si layers should be chosen carefully for a large effective electromechanical coupling which is very important for obtaining a good filter performance [116, 117]. At the same time, lateral geometry parameters including the electrode width (W), the separation between electrodes (g) and the number of fingers for the interdigitated electrodes affect the inter-resonator coupling coefficient (k) and filter's electric response. The thicknesses for the layers of BST-on-Si composite structure can be chosen using a 1-D acoustic transmission line model. These filters are fabricated on a 5 μm thick S membrane; therefore the BST thickness is chosen to achieve a high electromechanical coupling at the 2nd resonance mode using the 1-D acoustic transmission line model. Table 4.1 shows the layer thicknesses used in the intrinsically switchable laterally coupled acoustic filter shown in Figure 4.7.

The effect of device's lateral geometry on the filter performance cannot be studied using the 1-D transmission line model which is discussed in Chapter 2. Therefore, commercially available finite element methods (FEM) simulation software is used for this purpose. In this work, Comsol 4.2 multi-physics simulation software (Comsol Inc, Burlington, MA) is used to predict the filter performance.

4.3.1   Simulation Setup

The simulated filter is a two-dimensional (2-D) structure as shown in Figure 4.13. Comsol's 2-D pizeoelectric device (pzd) physics module is used to simulate the filter performance. The 2-D simulation is preferred to 3-D simulation for saving the time and computing resources. Since the structure is simulated in 2-D, only the effect of cross-sectional lateral geometry parameters, i.e. electrode width (W), the separation between electrodes (g), and number of fingers, are studied. The effect of electrode length on the inter-resonator coupling coefficient (k) cannot be simulated; however its effect on the impedance of the resonators is accounted in the Comsol simulations. To obtain accurate and reliable results, the structure is meshed with a minimum of 10 mesh elements per wavelength at the highest simulated frequency.
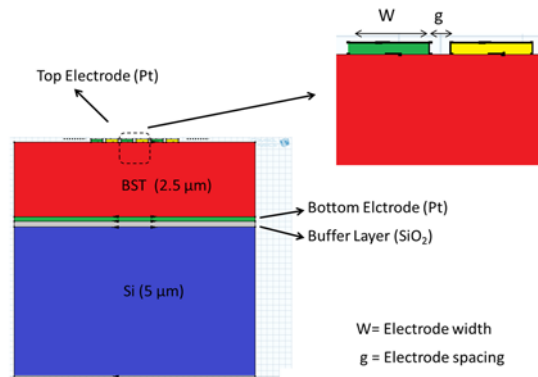
Figure 4.13: The laterally acoustically coupled filter structure simulated in Comsol

96

In the simulations, the BST layer is considered as a piezoelectric layer with piezoelectric coefficients being independent of electric field. Therefore, the electrostrictive property of BST is not simulated. The BST layer is modeled with Comsol's piezoelectric material model using the strain-charge form for the coupled piezoelectric equations. The strain-charge form piezoelectric constitutive equations given in Chapter 1 are again given in (4.3).

$$
\begin{aligned}
S &= s_E T + d^T E \\
D &= dT + \varepsilon_T E
\end{aligned}
$$

(4.3)

In (4.3), for the compliance matrix for BST, bulk BTO's compliance matrix that is available in Comsol's material library has been used with some slight modifications. To decrease the spurious mode excitation in the simulations, all the values in the piezoelectric coupling matrix (d) except d_{33} are set to zero. The d_{33} is determined based on measured BST BAWs for maximum applied DC bias voltage. The BST layer's piezoelectric and compliance matrix used in the Comsol simulations are given in (4.4) and (4.5), respectively.

$$
d = \begin{bmatrix}
0 & 0 & 0 & 0 & 0 & 0 \\
0 & 0 & 0 & 0 & 0 & 0 \\
0 & 0 & 2e-11 & 0 & 0 & 0
\end{bmatrix} (C/N)
$$

(4.4)

$$
s_E = \begin{bmatrix}
1.00e-11 & -0.27e-11 & -0.27e-11 & 0 & 0 & 0 \\
-0.27e-11 & 1.00e-11 & -0.27e-11 & 0 & 0 & 0 \\
-0.27e-11 & -0.27e-11 & 1.00e-11 & 0 & 0 & 0 \\
0 & 0 & 0 & 1.80e-11 & 0 & 0 \\
0 & 0 & 0 & 0 & 1.80e-11 & 0 \\
0 & 0 & 0 & 0 & 0 & 1.80e-11
\end{bmatrix}
$$

(4.5)

$(1/Pa)$

The Si membrane, the Pt electrodes and the SiO$_2$ buffer layer are modeled using Comsol's linear elastic model. The Si and Pt layers are considered to be un-isotropic with elasticity matrices shown in (4.6) and (4.7), respectively. The SiO$_2$ layer is considered to be isotropic with density (ρ), Young's modulus (E) and Poisson's ratio (υ) of 2200 kg/m^3, 70 GPa and 0.17, respectively.

$$c = \begin{bmatrix} 194.5 & 35.7 & 64.1 & 0 & 0 & 0 \\ 35.7 & 194.5 & 64.1 & 0 & 0 & 0 \\ 64.1 & 64.1 & 165.7 & 0 & 0 & 0 \\ 0 & 0 & 0 & 79.6 & 0 & 0 \\ 0 & 0 & 0 & 0 & 79.6 & 0 \\ 0 & 0 & 0 & 0 & 0 & 50.9 \end{bmatrix} \quad (4.6)$$

(GPa)

$$c = \begin{bmatrix} 346.7 & 250.7 & 250.7 & 0 & 0 & 0 \\ 250.7 & 346.7 & 250.7 & 0 & 0 & 0 \\ 250.7 & 250.7 & 346.7 & 0 & 0 & 0 \\ 0 & 0 & 0 & 76.5 & 0 & 0 \\ 0 & 0 & 0 & 0 & 76.5 & 0 \\ 0 & 0 & 0 & 0 & 0 & 76.5 \end{bmatrix} \quad (4.7)$$

(GPa)

The filter is simulated by injecting RF signal into the input resonator and shorting the output resonator to ground. For example, if the green top electrode, shown in Figure 4.13, is driven with the RF signal, then the yellow electrodes should be grounded (0 V). This is because, Comsol's piezoelectric module has predefined admittance parameters which can be readily used to obtain admittance matrix (Y-matrix) for a two port network if ports are terminated in properly. Since the input and output resonators are identical, the filters are symmetric and reciprocal, therefore $Y_{11} = Y_{22}$ and $Y_{12} = Y_{21}$.

98

The *Y* parameters obtained from the Comsol simulations are then converted to scattering parameters (*S*-parameters) to obtain the filter's insertion and return loss performance using [104]:

$$S_{11} = S_{22} = \frac{(Y_0 - Y_{11})(Y_0 + Y_{11}) + Y_{12}Y_{21}}{(Y_{11} + Y_0)(Y_{22} + Y_0) - Y_{12}Y_{21}} \tag{4.8}$$

$$S_{21} = S_{12} = \frac{-2Y_{21}Y_0}{(Y_{11} + Y_0)(Y_{22} + Y_0) - Y_{12}Y_{21}} \tag{4.9}$$

where *Y₀* is the system admittance which is 0.02 in the simulations discussed in this chapter. The plots of return loss and insertion loss obtained using the Comsol simulation for a BST-on-Si laterally acoustically coupled filter are shown in Figure 4.14. The shapes of the in phase and out-of-phase lamb-wave modes for this filter at the second resonance mode are illustrated in Figure 4.15 and Figure 4.16, respectively.
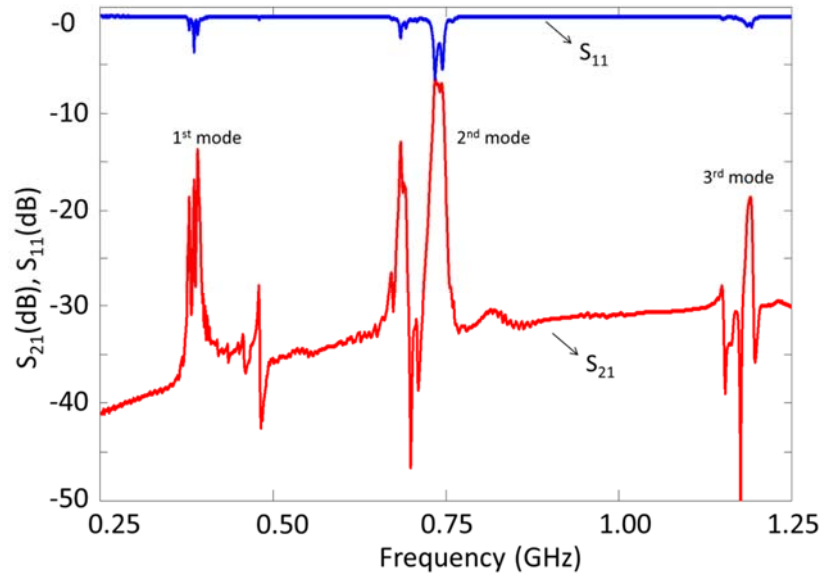
Figure 4.14: The insertion loss (S_{21}) and return loss (S_{11}) for a laterally coupled acoustic filter with lateral dimensions of W=30 μm, g=1 μm and number of fingers = 2.
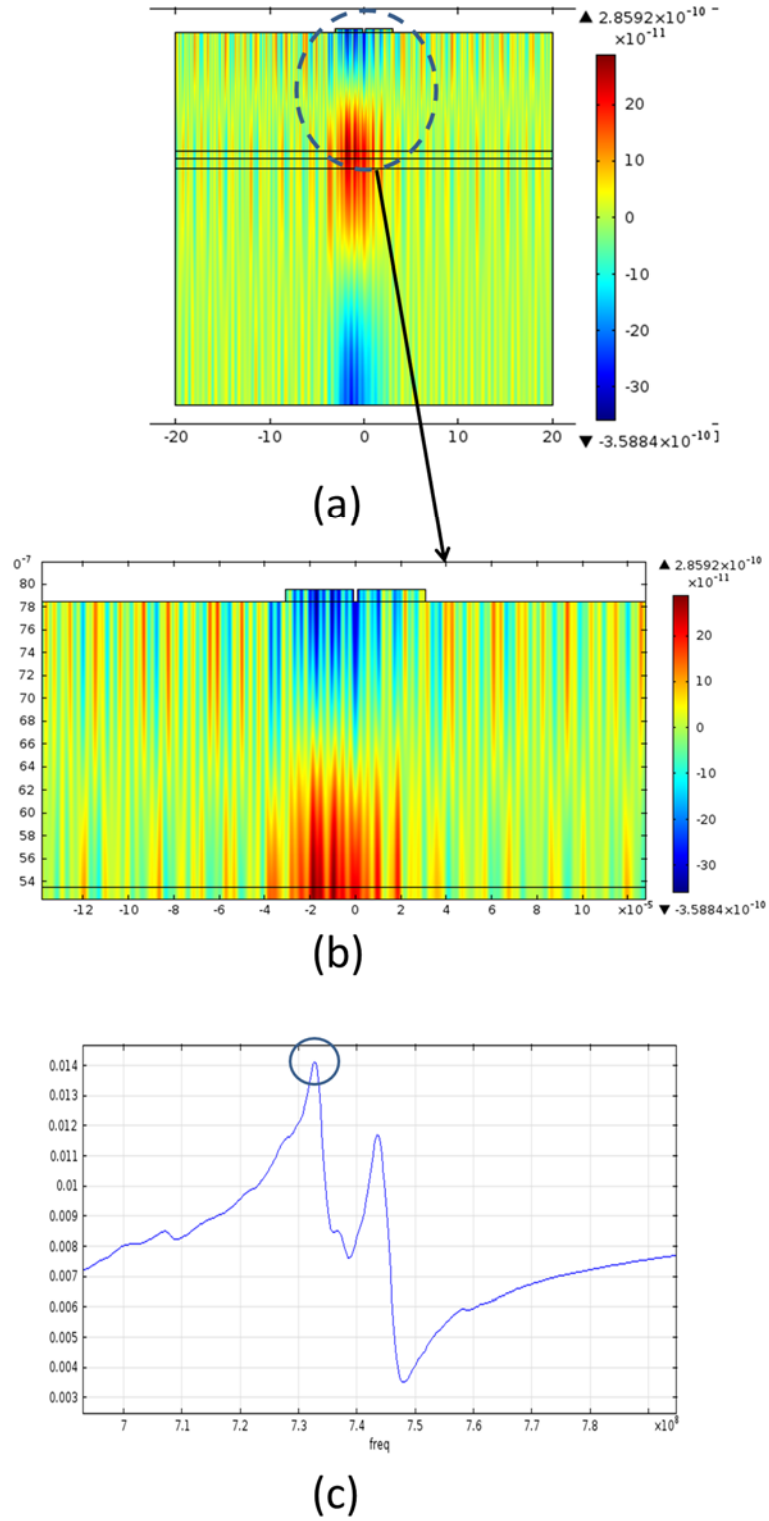
Figure 4.15: (a) and (b) show the simulated shape of the symmetric (in-phase) lamb wave mode for laterally coupled acoustic filter. The (c) shows the input admittance indicating the in-phase mode frequency with a circle.
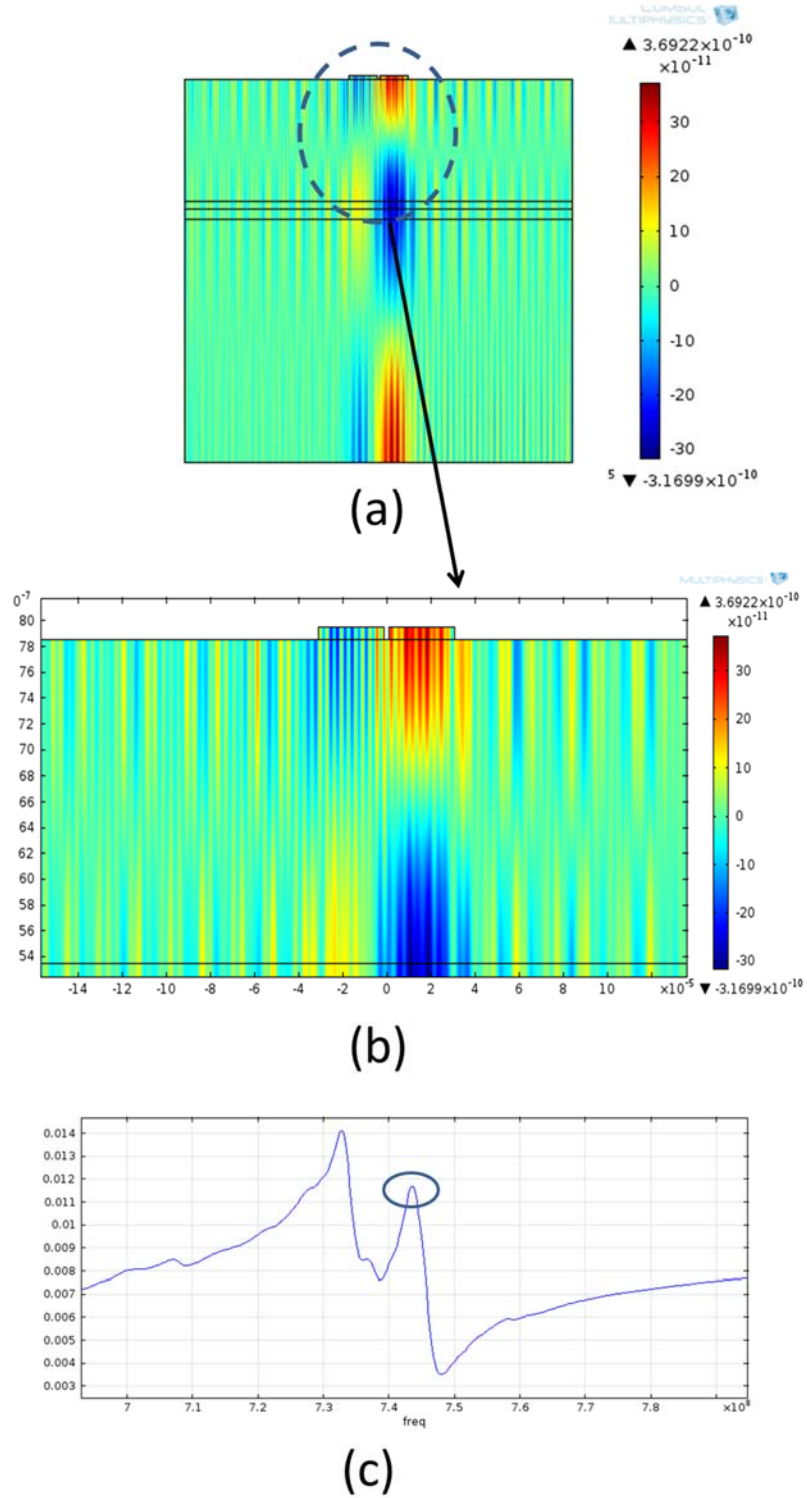
Figure 4.16: (a) and (b) show the simulated shape of the asymmetric (out-of-phase) lamb wave mode for laterally coupled acoustic filter de. (c) shows the input admittance indicating the out-of-phase mode frequency with a circle

In the following sub-sections, the effect of device's lateral geometry on the filter performance is discussed using the Comsol simulations. The simulation results are shown for the second resonance mode for which the thicknesses of the stacked layers are optimized. First the effect of electrode width and the electrode spacing (g) on the inter-resonator coupling coefficient is discussed. Then, the effect of the number of fingers on the inter-resonator coupling coefficient and on the resonator performance is analyzed. Finally, the filter response is analyzed as a function of the piezoelectric coefficient (d_{33}) to study the effect of electromechanical coupling on the insertion loss and inter-resonator coupling coefficient.

4.3.2   The Effect of Electrode Width (W) and Spacing Between Electrodes (g) on Filter's Response

The Y_{11} for the BST-on-Si laterally acoustically coupled filter structure shown in Figure 4.13 is simulated as a function of electrode width (W) and electrode spacing (g). The inter-resonator coupling coefficient (k) is then calculated at the second resonance mode using (4.2). It is observed that the inter-resonator coupling coefficient decreases with increasing electrode width (W). This is due to the increase in frequency spacing between the symmetric and anti-symmetric lamb waves as the electrode lateral dimension increases [116]. Figure 4.17 shows the inter-resonator coupling coefficient as a function of electrode width for various electrode spacing values.

The inter-resonator coupling coefficient decreases also with electrode spacing, as the acoustic wave attenuates exponentially (evanescent wave) in the region between input and output resonators. Figure 4.18 shows the inter-resonator coupling (k) coefficient as a function of electrode spacing (g) for various electrode widths (W).
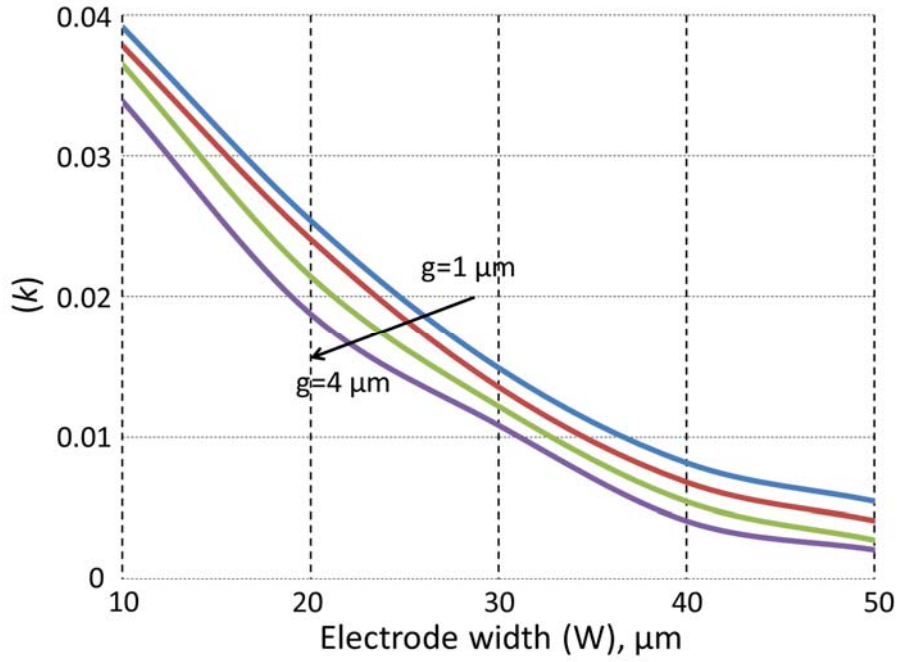
Figure 4.17: Inter-resonator coupling coefficient (k) as a function of electrode width (W) for various electrode spacing (g)
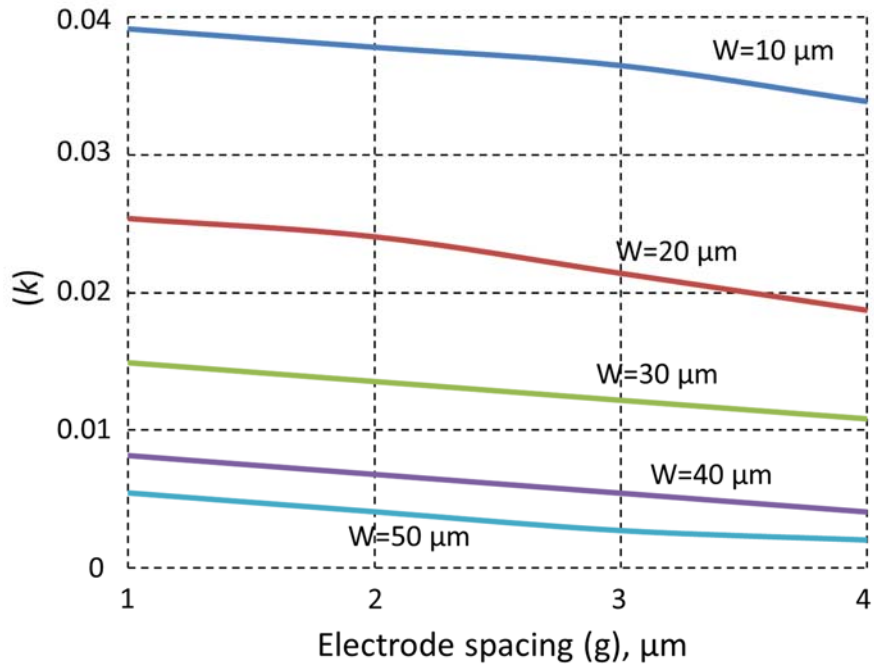
Figure 4.18: Inter-resonator coupling coefficient (k) as a function of electrode spacing (g) for various electrode widths (W)

4.3.3   The Effect of Number of Fingers on the Filter Performance

The filter shown in Figure 4.13 is simulated as a function of the number of fingers (N). In these simulations, the filter performance is degraded if the resonator area is very large due to the effect of large static capacitance (C_e) created by the sandwiched BST layer. Therefore, the simulations are performed by changing the number of fingers for up to N=6. The inter-resonator coupling coefficient increases with number of fingers. Figure 4.19 shows the inter-resonator coupling coefficient as a function of number of fingers. To illustrate the effect of the number of fingers (N) on the filter's electric response, the input admittance (Y_{11}) and insertion loss (S_{21}) for a filter with a 30 μm electrode width (W) and 1 μm electrode separation (g) is plotted as shown in Figure 4.20 and Figure 4.21, respectively.
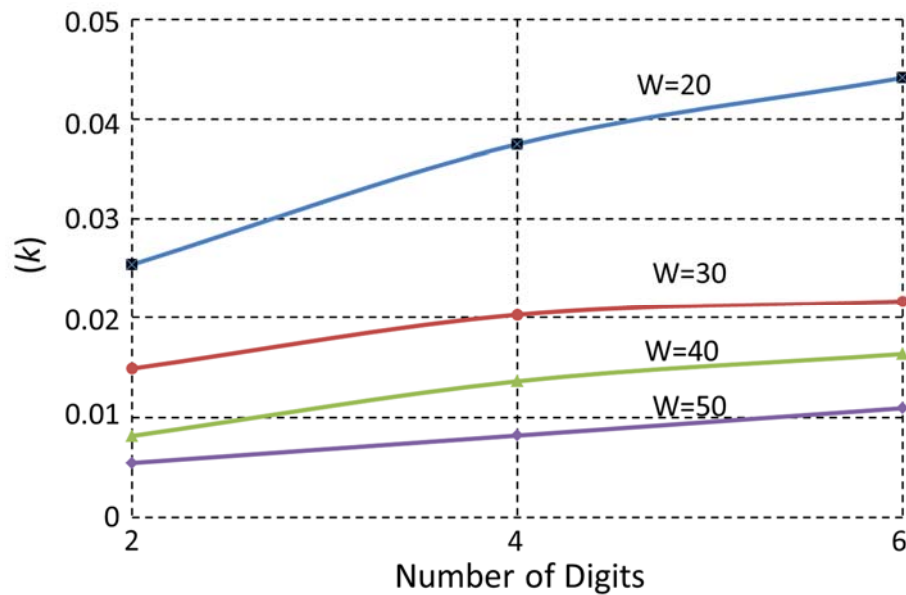
Figure 4.19: Inter-resonator coupling coefficient as a function of number of fingers
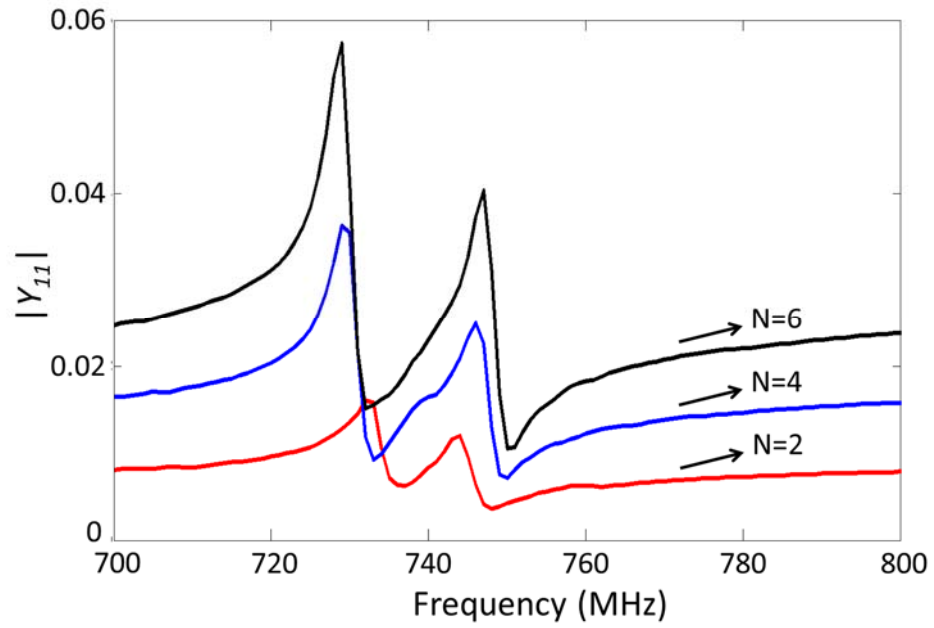
Figure 4.20: Y_{11} for 2,4 and 6 number of fingers (N). The W=30 μm and the g= 2 μm.
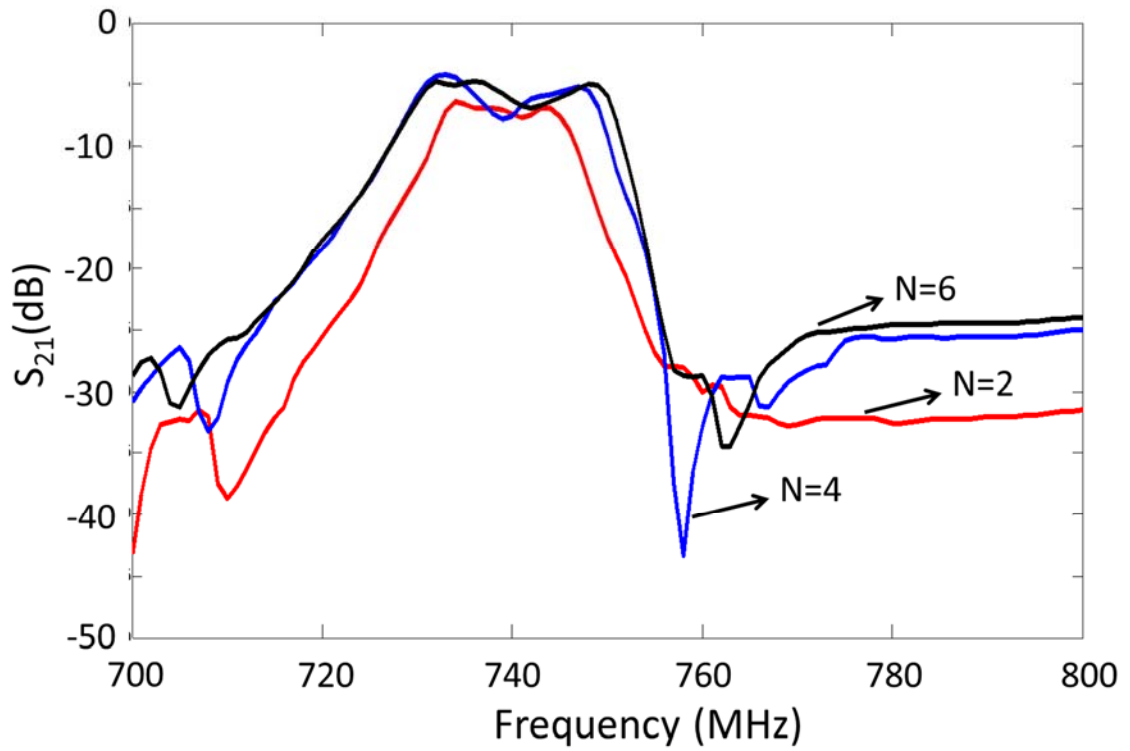
Figure 4.21: Insertion loss (S_{21}) for 2,4 and 6 number of fingers (N). The W=30 μm and the g= 2 μm.

4.3.4   The Effect of Piezoelectric Coefficient (d_{33}) on the Filter Peformance

The piezoelectric coefficient directly affects the effective electromechanical coupling coefficient (K_t^2) for the bulk acoustic resonators. A larger K_t^2 is desired for a good filter performance in acoustic filters [84]. The resonance modes get stronger with increasing d_{33} as expected. Figure 4.22 shows the insertion loss (S_{21}) of a filter for d_{33} of 1e-11 [C/N] to 5e-11 [C/N] with 1e-11 [C/N] steps at the second resonance mode. In this simulated filter, the number of digits (N), the electrode width (W) and the separation between electrodes (g) are 2, 20 μm and 2 μm, respectively. As shown in Figure 4.22, filter insertion loss improves and its bandwidth increases with increasing d_{33}.
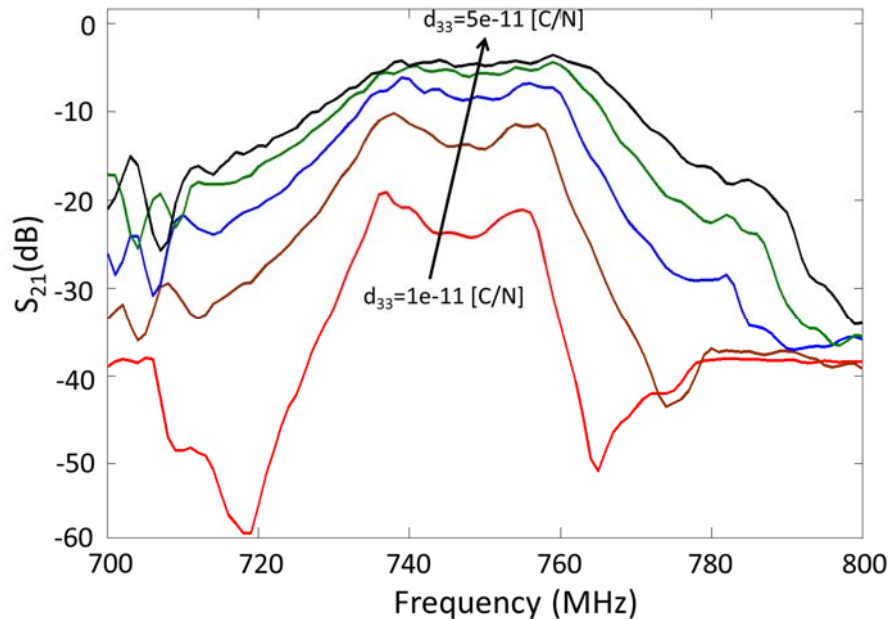
Figure 4.22**:** The insertion loss (S_{21}) for d_{33} of 1e-11 [C/N] to 5e-11 [C/N] at the second resonance mode

The Comsol simulations shown above are approximate due to the 2-D nature of simulations and lack of accuracy BST acoustic properties. Nevertheless, these

simulations can be used to understand the device performance as a function of device geometry and provide a starting point for designing the chip layout that includes filters with systematically varying lateral geometries. The following section explains the fabrications steps for the intrinsically switchable laterally coupled acoustic filters based on BST-on-Si composite structure.

4.4   Fabrication Procedure

The intrinsically switchable laterally acoustically coupled filters are fabricated on a silicon-on-insulator (SOI) wafer. The SOI wafer has a 5 μm thick device Si layer. This layer is used to create the Si membrane for the BST-on-Si composite structure Figure 4.7.

The device fabrication starts with growing a 200 nm thick layer of high quality SiO_2 on the SOI wafer. A 40 nm of TiO_2 and a 150 nm layer of platinum (bottom electrode) are deposited on the SiO_2 layer. The bottom electrode is patterned by selectively etching the Pt. An approximately 2.5 μm thick layer of BST thin film is deposited on top of the bottom electrode by pulsed laser deposition (PLD). PLD deposition is performed at 650 °C with a partial oxygen pressure of 300 mT. Next, a 100 nm thick layer of platinum is deposited and patterned by e-beam evaporation and lift-off for creating top electrodes. The chip is annealed under flowing O_2 at 500 ºC for 30 minutes. After annealing, the BST thin film is selectively etched using diluted hydrofluoric acid (HF). A total of 3 μm thick aluminum and gold layers are deposited for the probe contact pads. The silicon handle layer is etched away completely by deep reactive ion etching (DRIE) from the back side of the wafer. Finally, the buried oxide layer is wet etched to fully release the device. The fabrication steps for the laterally acoustically coupled filters explained here are the same as the BST-on-Si composite FBAR fabrication steps discussed in Chapter 2.

Therefore, Figure 2.20 in Chapter 2 illustrates the laterally coupled acoustic filter fabrication steps. The detailed recipes for each step are given in Appendix A.

4.5   Measurement Results

The filters were measured with 150 μm pitch size GSG probes. Filter's S-parameters are acquired by using an Agilent E8364C vector network analyzer. The measurement set up is calibrated with short-open-load-thru (SOLT) calibration. Devices are biased through bias tees connected to GSG probes at the input and output ports. During the measurements, the bias voltage is increased gradually from 0 V to 55 V until the input impedance no longer varies with the bias voltage due to the saturation of the voltage-induced electric polarization in the BST layer [78]. A microscope photo of a measured device with N = 4, W = 40 μm and g = 2 μm is shown in Figure 4.23.
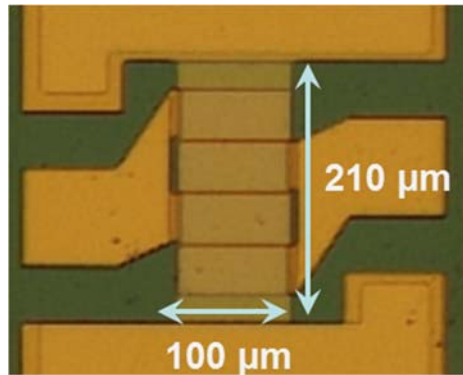
Figure 4.23**:** Microscope photo of a measured intrinsically switchable laterally acoustically coupled filter. In this filter N= 4, W= 40 μm and g= 2 μm.

The measurement results for an intrinsically switchable laterally acoustically coupled filter shown in Figure 4.23 are provided below for the second resonance mode. Figure 4.24 and Figure 4.25 show the insertion loss (S_{21}) and return loss (S_{11}) of the filter at a 0

V (off) and a 55 V (on) dc bias. Such a high turn-on voltage (e.g 55 V) is attributed to large BST thickness which is 2.5 μm in this device.
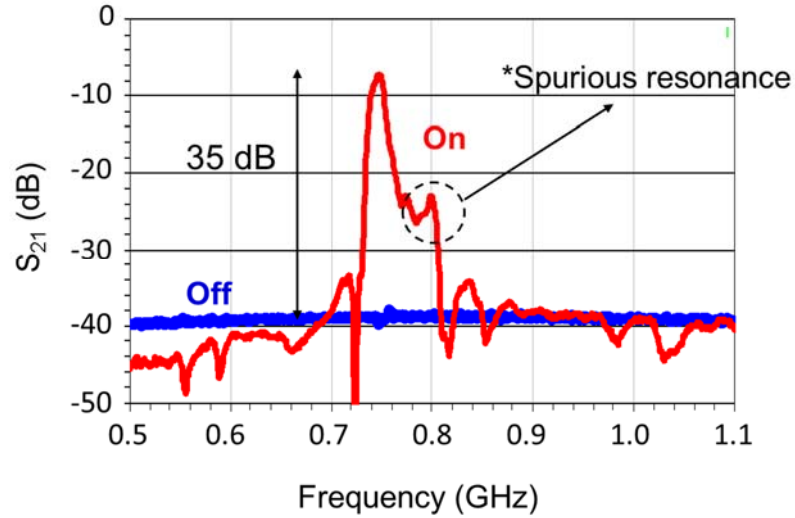
Figure 4.24: Insertion loss (S_{21}) of a measured filter for 0 V and 55 V dc bias
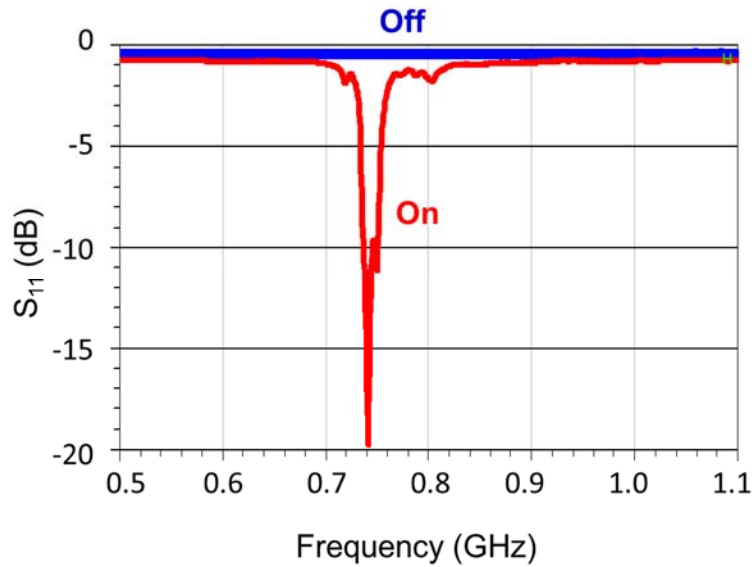
Figure 4.25: Return loss (S_{11}) of a measured filter for 0 V and 55 V dc bias

As shown in Figure 4.24, there is a spurious resonance mode slightly above the filter's passband. Such spurious resonances are caused by unwanted lamb-wave modes that are excited in the structure [105]. To predict these spurious modes accurately, a dispersion

curve of the composite structure with and without electrodes should be obtained with accurate acoustic parameters for the layers [105]. Such a study has not been performed yet and could be a future study with better characterized BST acoustic properties. The filter's measured performance is summarized in Table 4.2. The filter's insertion loss at several bias voltages is plotted in Figure 4.26. The filter's wide band response is shown in Figure 4.27. The second resonance mode provides the strongest resonance response as expected. The modes above the 3rd mode are very weak and not shown in Figure 4.27.

Table 4.2 Performance of the measured intrinsically switchable laterally acoustically coupled filter based on BST-on-Si structure

Center frequency (f_c)	748 MHz
3dB bandwidth (BW$_{3dB}$)	13.8 MHz (% 1.8)
Insertion Loss (S$_{21}$)	7.1 dB
Return Loss (S$_{11}$)	>10 dB
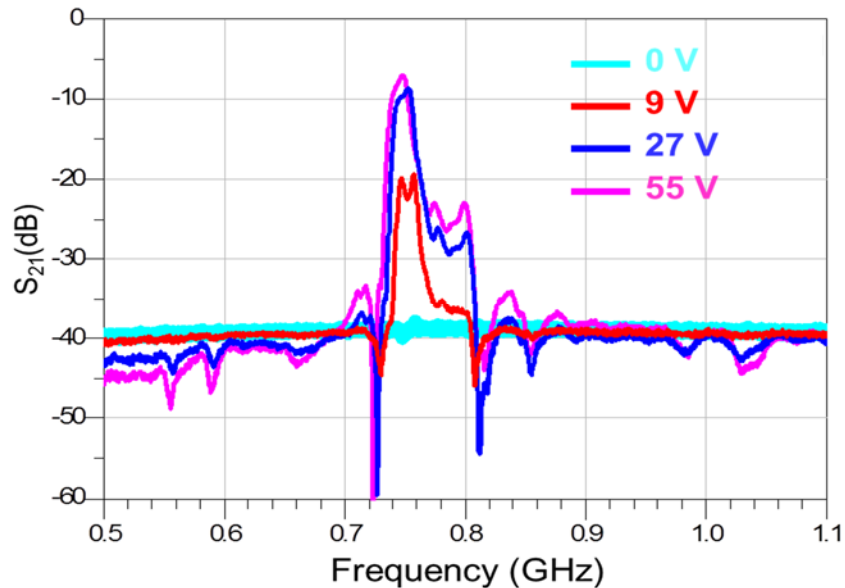
Figure 4.26: Measured insertion loss (S$_{21}$) at several bias voltages
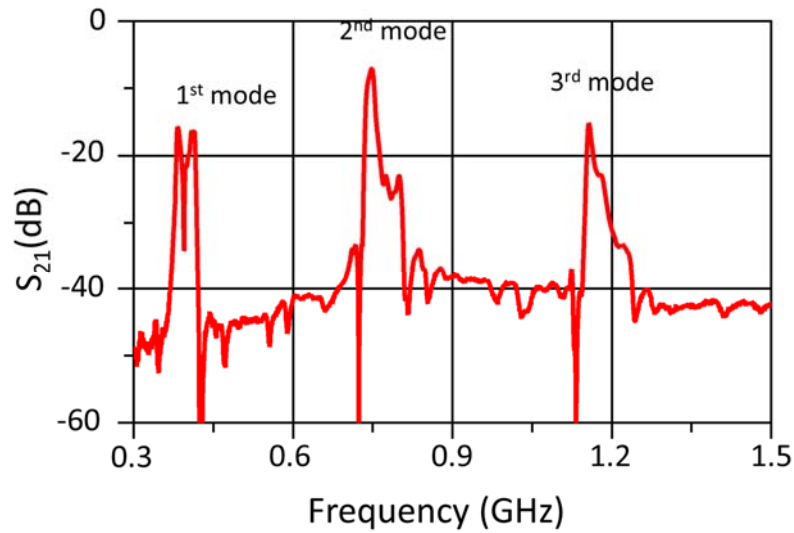
Figure 4.27: Wide band plot for the measured insertion loss (S_{21})

The measured filter response is fitted to an equivalent lumped element model shown in Figure 4.9. The return loss and the insertion loss for the fitted lumped element model and measurement results are shown in Figure 4.28. The lumped element model components and inter-resonator coupling coefficient is given in Table 4.3.
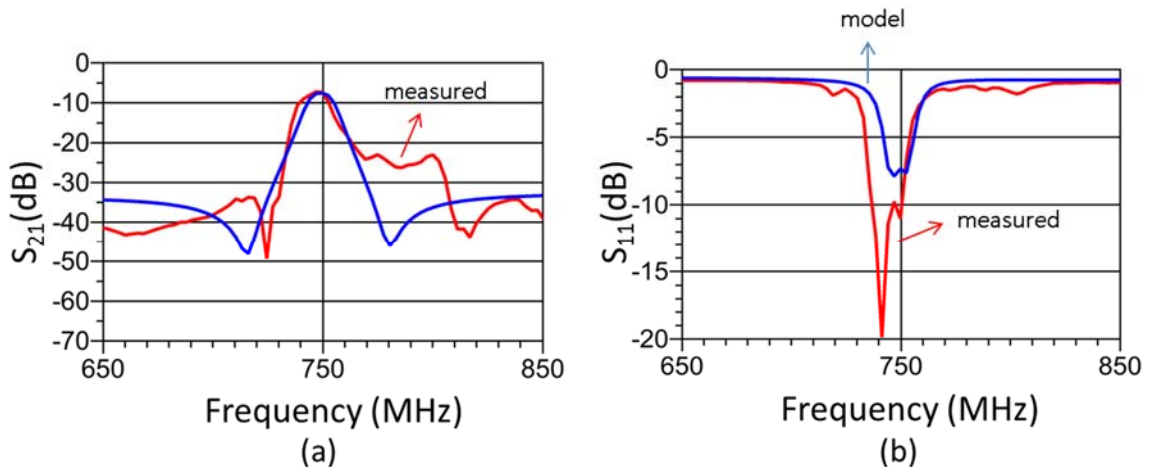
Figure 4.28: Measured and modeled (a) insertion loss (S_{21}) and, (b) return loss (S_{11})

Table 4.3 Component values from the fitted lumped element model

R_s	3 Ω
R_p	1500 Ω
R_e	2 Ω
C_e	4 pF
R_m	40 Ω
L_m	1000 nH
C_m	0.0448 pF
C_f	0.08 pF
M	13 nH

Based on lumped element model, most of the insertion loss is due to acoustic loss in the device. For example, by reducing the R_m from 40 Ω to 10 Ω, the insertion loss improves reduces from 7 dB to approximately 3.4 dB.

4.6   Conclusion

To the best of author's knowledge, the results for the first BST based intrinsically switchable acoustically coupled filter are presented here. The device provides approximately 40 dB of isolation when it is off and exhibits 7.1 dB of insertion loss when it is turned on (Figure 4.24). The filter consists of two BAW resonators coupled acoustically in the lateral direction and provides an out-of-band rejection level of more than 35 dB which is much higher than that of an electrically connected filter with the same number of resonators. Future work will focus on improving the performance of the

filters by depositing higher quality thin films. To predict the spurious modes accurately, well-characterized BST acoustic parameters are needed for simulations.

Chapter 5

Conclusions and Future Directions

5.1 Summary

In this dissertation, three different types of bulk acoustic wave devices based on BST-on-Si composite structure are presented. The first device is a high-Q intrinsically switchable composite FBAR. In this device, a detailed design procedure using an acoustic transmission line model is explained. A fabrication process for composite FBARs, using silicon-on-insulator (SOI) wafer, is described. Measured devices exhibit record Q values in BST based switchable BAW resonators.

The second device is a 1.5 stage intrinsically switchable electrically connected filter based on BST-on-Si composite FBARs. The detailed design procedure and measurement result of a fabricated filter are presented. The measured filter exhibits an insertion loss and return loss of 4.5 dB and 15 dB, respectively, when it is biased. Out of band rejection level is approximately 8 dB.

The third device is a laterally coupled acoustic filter based on BST-on-Si composite structure. The operation principles for these devices are discussed in detail. Filter's typical electric response is explained using a lumped element model that is commonly used for acoustically coupled filters. Multiphysics simulations are performed using a finite element method (FEM) based commercially available simulation tool (Comsol).

Using this simulation tool, the effect of device geometry and the piezoelectric coefficient on the performance of laterally coupled acoustic filters is studied. The fabrication procedure and measurement results for a laterally coupled acoustic filter are presented. The measured device exhibits approximately a 7 dB of insertion loss and more than 9 dB of return loss. To the best of author's knowledge, this is the first demonstration of intrinsically switchable acoustically coupled filters based on ferroelectric BST.

5.2 Future Work

5.2.1 BST Thin Film Deposition and Optimization

The intrinsically switchable resonators and filters discussed in this dissertation are based on thin film BST deposited using pulsed laser deposition system. Currently, a new magnetron-sputtering thin film deposition system is being installed by our research group. A detailed study of the deposition parameters can allow us to improve the BST's quality further for obtaining high performance BAW devices. Furthermore, BST's piezoelectric, dielectric and acoustic properties should be studied as a function of deposition parameters such as deposition temperature and argon to oxygen ratio. Such study will help in optimizing the performance of BAW devices.

In addition, BSTs with different Stoichiometry can be utilized. A future work can be studying the effect of Ba and Sr ratio on piezoelectric and acoustic properties of BST thin films.

5.2.2 Designing a symmetric composite FBAR

FBARs based on a BST-on-Si composite structure have been demonstrated. The structure is asymmetric along the horizontal line at the middle of the piezoelectric layer

and exhibits both even and odd resonance modes. Future work can be fabricating symmetric composite FBARs similar to the one shown in Figure 1.12. Although fabrication of the symmetric BST based resonators is a challenge, symmetric structure has the advantage of exhibiting reduced number of overmodes.

In symmetric structures, by incorporating low permittivity non-piezoelectric layers in between electrodes and BST, the effective permittivity of the region between the top and bottom electrodes can be reduced. This allows designing larger size FBARs with reduced edge-effect that limits the Q and K_t^2 hence performance of FBARs. However, addition of such a non-piezoelectric layer in between the electrodes and the BST increases the DC voltage levels to control the filters.

Appendices

Appendices

Appendix A

Fabrication Steps of Composite Resonators and Filters Based on BST-on-Si Structure

A.1 SOI Wafer Preperation

Start with a pre-platinized silicon-on-insulator (SOI) wafer with total thicknesses of 300 µm – 600 µm

• Dice and blow dry using N2 gas.

• Rinse in aceton for 3 min.

• Rinse in isopropyl alcohol (IPA) for 3 min.

• Rinse in the DI water for 5 min.

• N_2 blow dry.

• Dehydration bake 130 °C for 3 min.

A.2 Bottom Electrode Patterning

• Apply HMDS to substrate and let it stay for 30 sec.

• Spin HMDS at 4000 rpm for 30 sec.

• Spin SPR 220 3.0 at 3000 rpm for 30 sec.

• Soft bake at 115 °C for 90 sec.

- Image exposure 6 sec in MA/BA 6

- Post-exposure bake at 115 °C for 90 sec.

- Develop in AZ 300 for 1 min

- Rinse in DI water for 5 min and N_2 blow dry.

- Check the pattern under microscope.

- Oxygen asher at 250mT and 80W for 60 sec.

- Etch Pt in Plasmatherm 790 with reactive ion etching (RIE) method. Recipe in plasmatherm should be verified/optimized at the beginning of each batch fabrication

- Verify the etching by resistance measurement test in the etched area

- Oxygen asher at 250mT and 80W for 60 sec.

- Clean in warm acetone

- Put it in IPA

- N_2 blow dry.

- Dehydration bake 130 °C for 3 min.

A.3 BST Deposition in PLD

- Load the substrate and heat up the substrate with 5 °C/min rate.

- Substrate temperature of 650 °C.

- Partial oxygen pressure of 300 mTorr.

- In chamber oxygen annealing at 650 °C with 100 Torr oxygen for 1 hour.

- Cool down the substrate with 1 °C/min rate.

A.4 Top Electrode Deposition and Lift-Off

- Apply HMDS to substrate and let it stay for 30 sec.

• Spin HMDS at 4000 rpm for 30 sec.

• Spin 220 3.0 at 3000 rpm for 30 sec.

• Soft bake at 115 °C for 90 sec.

• Image exposure 6 sec in MA/BA 6

• Post-exposure bake at 115 °C for 90 sec.

• Oxygen asher at 250mT and 80W for 60 sec.

• Metal evaporation (Pt 1000 °A).

• Liftoff in Acetone for at least 1 hour.

• Rinse in isopropyl alcohol (IPA) for 5 min.

• N_2 blow dry.

• Dehydration bake 130 °C for 3 min

A.5 High-Temperature Annealing

• Furnace temperature at 500 °C.

• Flow oxygen with 2 sccm rate.

• Anneal for 30 min.

A.6 BST Etch in HF

• Apply HMDS to substrate and let it stay for 30 sec.

• Spin HMDS at 4000 rpm for 30 sec.

• Spin SPR 220 3.0 at 3000 rpm for 30 sec.

• Soft bake at 115 °C for 90 sec.

• Image exposure 6 sec in MA/BA 6

• Post-exposure bake at 115 °C for 90 sec.

• Develop in AZ300 for 1 min.

• Rinse in DI water for 5 min and N_2 blow dry.

• Check the pattern under microscope.

• Oxygen asher at 250mT and 80W for 60 sec.

• Hard bake 110 °C for 1 min.

• Wet etch in HF:DI (1:10) solution. (etch rate is about 200 nm for 20 sec)

• Rinse in DI water for 5 min and N_2 blow dry.

• Inspect the film thickness by Dektak.

• Strip photoresist in aceton for at least 1 hour.

• Rinse in isopropyl alcohol (IPA) for 5 min.

• N_2 blow dry.

• Dehydration bake 130 °C for 3 min.

A.7 Bias Network Deposition/Sputter and Lift-Off

• Apply HMDS to substrate and let it stay for 30 sec.

• Spin HMDS at 4000 rpm for 30 sec.

• Spin SPR 220 3.0 at 3000 rpm for 30 sec.

• Soft bake at 115 °C for 90 sec.

• Soft bake at 115 °C for 90 sec.

• Image exposure 6 sec in MA/BA 6

• Post-exposure bake at 115 °C for 90 sec.

• Develop in AZ300 for 1 min.

• Rinse in DI water for 5 min and N_2 blow dry.

• Check the pattern under microscope.

• Oxygen asher at 250mT and 80W for 60 sec.

• Deposit or Sputter the Resistance material

• Liftoff in Acetone for at least 1 hour.

• Rinse in isopropyl alcohol (IPA) for 3 min.

• N_2 blow dry.

• Dehydration bake 130 °C for 3 min.

A.8 Compensation Layer Deposition and Lift-Off

• Apply HMDS to substrate and let it stay for 30 sec.

• Spin HMDS at 4000 rpm for 30 sec.

• Spin SPR 220 3.0 at 3000 rpm for 30 sec.

• Soft bake at 115 °C for 90 sec.

• Soft bake at 115 °C for 90 sec.

• Image exposure 6 sec in MA/BA 6

• Post-exposure bake at 115 °C for 90 sec.

• Develop in AZ300 for 1 min.

• Rinse in DI water for 5 min and N_2 blow dry.

• Check the pattern under microscope.

• Oxygen asher at 250mT and 80W for 60 sec.

• Deposit Aluminum and Gold in Evaporator

• Liftoff in Acetone for at least 1 hour.

• Rinse in isopropyl alcohol (IPA) for 3 min.

• N_2 blow dry.

• Dehydration bake 130 °C for 3 min.

A.9 Contact Metal Evaporation and Lift-Off

• Apply HMDS to substrate and let it stay for 30 sec.

• Spin HMDS at 4000 rpm for 30 sec.

• Spin SPR 220 3.0 at 3000 rpm for 30 sec.

• Soft bake at 115 °C for 90 sec.

• Soft bake at 115 °C for 90 sec.

• Image exposure 6 sec in MA/BA 6

• Post-exposure bake at 115 °C for 90 sec.

• Develop in AZ300 for 1 min.

• Rinse in DI water for 5 min and N_2 blow dry.

• Check the pattern under microscope.

• Oxygen asher at 250mT and 80W for 60 sec.

• Deposit Aluminum and Gold in Evaporator

• Liftoff in Acetone for at least 1 hour.

• Rinse in isopropyl alcohol (IPA) for 3 min.

• N_2 blow dry.

• Dehydration bake 130 °C for 3 min.

Appendix B

Matlab Codes For Electrically Connected Filter Simulations

```matlab
%29 July 2011

clear,clc,clf

f=0.1e9:765.625e3:2.8e9;

%Velocity of longitudinal acoustic wave (m/s)
v_pt = 3300;    v_au = 2800;    v_sapphire = 11150; v_air = 360;
v_si = 8100;    v_sio2 = 5100;  v_sto = 8050;
v_sto = 10400;  v_zno = 6340;   v_pzt = 4500;    v_mo = 6290;
v_aln = 11000;  v_al = 6300;    v_bst = 5600; v_ti = 6100;

%Acoustic impedance (kg/m^2s)
z_pt = 69.8e6;  z_au = 23.18e6;  z_sapphire = 44.5e6;    z_air = 360;
z_si = 21e6;  z_sio2 = 12.55e6;   z_bst = 33e6; z_sto = 42.2e6;
z_zno = 36.4e6; z_pzt = 31.3e6;    z_mo = 64.2e6;  z_aln = 36e6;
z_al = 17e6; z_ti = 27.3e6;

%Acoustic quality factor
Q_pt = 130; Q_au = 130;  Q_sio2 = 130;
Q_bst = 300;   Q_sto = 9500;   Q_aln = 9500;
Q_sapphire = 9500; Q_ti = 100
% Q_si = 5000;
Q_si = 6.2e12./1000e6;
K2= 0.062;
Area_series = (1050)*(10^-12);

%Thickness (m)
t_au = 100e-9;
t_pt = 100e-9;
t_bst = 600e-9;
t_pt2 =150e-9;
t_ti=40e-9;
t_sio2 = 0.2e-6;
t_si = 10e-6;
t_sio2_2 =0e-6; %(optional)



%Dielectric Constant
EC_zno = 8.8;   EC_pzt = 350;    EC_aln = 9.5; EC_bst = 90;

% The PROPAGATION CONSTANT of gold (Au)
beta_au = 2*pi.*f/v_au;
alpha_au = beta_au/2/Q_au;
gama_au = alpha_au + j.*beta_au;

% The impedance seen through top au
```

```matlab
Zl = z_au.*(z_air + z_au.*tanh(gama_au.*t_au))./(z_au +
z_air.*tanh(gama_au.*t_au));

% The PROPOGATION CONSTANT of platinum
beta_pt = 2*pi.*f/v_pt;
alpha_pt = beta_pt/2/Q_pt;
gama_pt = alpha_pt + j.*beta_pt;

% The impedance seen through top electrode
Zl = z_pt.*(Zl + z_pt.*tanh(gama_pt.*t_pt))./(z_pt +
Zl.*tanh(gama_pt.*t_pt));

%_____
____

%Zr has the load of air and transmission line in Si, SiO2 and Pt

% The PROPOGATION CONSTANT of buried oxide
beta_sio2 = 2*pi.*f/v_sio2;
alpha_sio2 = beta_sio2/2/Q_sio2;
gama_sio2 = alpha_sio2 + j.*beta_sio2;

%The impedance seen after the buried oxide
Z_sio2_2 = z_sio2.*(z_air + z_sio2.*tanh(gama_sio2.*t_sio2_2))./(z_sio2
+ z_air.*tanh(gama_sio2.*t_sio2_2));

% The PROPOGATION CONSTANT of device silicon
beta_si = 2*pi.*f/v_si;
alpha_si = beta_si./2./Q_si;
gama_si = alpha_si + j.*beta_si;

% The impedance seen after silicon
Z_si = z_si.*(Z_sio2_2 + z_si.*tanh(gama_si.*t_si))./(z_si +
Z_sio2_2.*tanh(gama_si.*t_si));


% The PROPOGATION CONSTANT of oxide underneath of bottom electrode
beta_sio2 = 2*pi.*f/v_sio2;
alpha_sio2 = beta_sio2/2/Q_sio2;
gama_sio2 = alpha_sio2 + j.*beta_sio2;

% The impedance seen after oxide underneath of the bottom electrode
Z_sio2 = z_sio2.*(Z_si + z_sio2.*tanh(gama_sio2.*t_sio2))./(z_sio2 +
Z_si.*tanh(gama_sio2.*t_sio2));


% The PROPOGATION CONSTANT of titanium
beta_ti = 2*pi.*f/v_ti;
alpha_ti = beta_ti/2/Q_ti;
gama_ti = alpha_ti + j.*beta_ti;;

% The impedance after titanium
Z_ti= z_ti.*(Z_sio2 + z_ti.*tanh(gama_ti.*t_ti))./(z_ti +
Z_sio2.*tanh(gama_ti.*t_ti));
```

```matlab
% The impedance after the bottom electrode (platinum)
Zr = z_pt.*(Z_ti + z_pt.*tanh(gama_pt.*t_pt2))./(z_pt +
Z_ti.*tanh(gama_pt.*t_pt2));


%_____
____


% The DIELECTRIC CONSTANT and STATIC CAPACITANCE
E0 = 8.854e-12;
C_E = E0*EC_bst*Area_series/t_bst/(1);

% The PROPOGATION CONSTANT of BST
beta_bst = 2.*pi.*f./v_bst;
alpha_bst = beta_bst./2./Q_bst;
gama_bst = alpha_bst + j.*beta_bst;

% The half of the phase delay in BST
phi_bst = -j.*gama_bst.*t_bst/2;

% The normalized left and right impedances
zl = Zl./z_bst; zr = Zr./z_bst;


Zin_model_series =1+1./j./2./pi./f./C_E.*(1 -
K2.*tan(phi_bst)./phi_bst.*((zl+zr).*cos(phi_bst).*cos(phi_bst) +
j.*sin(2.*phi_bst))./((zl+zr).*cos(2.*phi_bst) +
j.*(zl.*zr+1).*sin(2.*phi_bst)));


% Now we have obtained the input impedance of the device based on
transmission
% line model

%_____
____


% Capacitance and Loss tangent is extracted from the Zin which was
obtained
% based on transmission line model

Zin_model_modulus = abs(Zin_model_series);




figure (1);
plot(f,abs(Zin_model_series));title('|Zin_series|');grid on;
hold on
% axis([0.1e9 5e9 0 120])
```

```
%_____
_____
_____
% Below provides the input impedance for the shunt resonator

t_au = 140e-9;
t_pt = 100e-9;
t_bst = 600e-9;
t_pt2 =150e-9;
t_ti=40e-9;
t_sio2 = 0.2e-6;
t_si = 10e-6;
t_sio2_2 =0e-6; %(optional)
Area_shunt = (2300)*(10^-12);



% %frequency (Hz)
% f = [0.5e9:0.005e6:5e9];



%Dielectric Constant
EC_zno = 8.8;    EC_pzt = 350;    EC_aln = 9.5; EC_bst = 90;


%Structure of the device: Air/Pt/BST/Pt/SiO2/Si
%Calculation of impedances: Zl --> Zin <-- Zr

%Zl has the load of air and transmission line in Pt and Au

% The PROPAGATION CONSTANT of gold (Au)
beta_au = 2*pi.*f/v_au;
alpha_au = beta_au/2/Q_au;
gama_au = alpha_au + j.*beta_au;

% The impedance seen through top au
Zl = z_au.*(z_air + z_au.*tanh(gama_au.*t_au))./(z_au +
z_air.*tanh(gama_au.*t_au));



% The PROPAGATION CONSTANT of platinum
beta_pt = 2*pi.*f/v_pt;
alpha_pt = beta_pt/2/Q_pt;
gama_pt = alpha_pt + j.*beta_pt;

% The impedance seen through top electrode
Zl = z_pt.*(Zl + z_pt.*tanh(gama_pt.*t_pt))./(z_pt +
Zl.*tanh(gama_pt.*t_pt));



%_____
____


%Zr has the load of air and transmisstion line in Si, SiO2 and Pt
% The PROPAGATION CONSTANT of buried oxide
```

```matlab
beta_sio2 = 2*pi.*f/v_sio2;
alpha_sio2 = beta_sio2/2/Q_sio2;
gama_sio2 = alpha_sio2 + j.*beta_sio2;

%The impedance seen after the buried oxide
Z_sio2_2 = z_sio2.*(z_air + z_sio2.*tanh(gama_sio2.*t_sio2_2))./(z_sio2
+ z_air.*tanh(gama_sio2.*t_sio2_2));




% The PROPAGATION CONSTANT of device silicon
beta_si = 2*pi.*f/v_si;
alpha_si = beta_si./2./Q_si;
gama_si = alpha_si + j.*beta_si;

% The impedance seen after silicon
Z_si = z_si.*(Z_sio2_2 + z_si.*tanh(gama_si.*t_si))./(z_si +
Z_sio2_2.*tanh(gama_si.*t_si));




% The PROPAGATION CONSTANT of oxide underneath of bottom electrode
beta_sio2 = 2*pi.*f/v_sio2;
alpha_sio2 = beta_sio2/2/Q_sio2;
gama_sio2 = alpha_sio2 + j.*beta_sio2;

% The impedance seen after oxide underneath of the bottom electrode
Z_sio2 = z_sio2.*(Z_si + z_sio2.*tanh(gama_sio2.*t_sio2))./(z_sio2 +
Z_si.*tanh(gama_sio2.*t_sio2));




% The PROPOGATION CONSTANT of titanium
beta_ti = 2*pi.*f/v_ti;
alpha_ti = beta_ti/2/Q_ti;
gama_ti = alpha_ti + j.*beta_ti;;




% The impedance after titanium
Z_ti= z_ti.*(Z_sio2 + z_ti.*tanh(gama_ti.*t_ti))./(z_ti +
Z_sio2.*tanh(gama_ti.*t_ti));




% The impedance after the bottom electrode (platinum)
Zr = z_pt.*(Z_ti + z_pt.*tanh(gama_pt.*t_pt2))./(z_pt +
Z_ti.*tanh(gama_pt.*t_pt2));
%_____
____



% The DIELECTRIC CONSTANT and STATIC CAPACITANCE
```

```matlab
E0 = 8.854e-12;
C_E = E0*EC_bst*Area_shunt/t_bst/(1);



% The PROPOGATION CONSTANT of BST
beta_bst = 2.*pi.*f./v_bst;
alpha_bst = beta_bst./2./Q_bst;
gama_bst = alpha_bst + j.*beta_bst;

% The half of the phase delay in BST
phi_bst = -j.*gama_bst.*t_bst/2;

% The normalized left and right impedances
zl = Zl./z_bst; zr = Zr./z_bst;

Zin_model_shunt =1+1./j./2./pi./f./C_E.*(1 -
K2.*tan(phi_bst)./phi_bst.*((zl+zr).*cos(phi_bst).*cos(phi_bst) +
j.*sin(2.*phi_bst))./((zl+zr).*cos(2.*phi_bst) +
j.*(zl.*zr+1).*sin(2.*phi_bst)));



% Now we have obtained the input impedance of the device based on
transmission
% line model

Zin_model_modulus = abs(Zin_model_shunt);



figure (1);
plot(f,abs(Zin_model_shunt),'r');title('|Zin_shunt|');grid on;

% Finding ABCD matrice

A= 1+(Zin_model_series./Zin_model_shunt);
B= 2.*Zin_model_series+(Zin_model_series.^2)./Zin_model_shunt;
C= 1./Zin_model_shunt;
D=1+(Zin_model_series./Zin_model_shunt);

%Finding S-parameters

denom= A+B/50+C*50+D;
S11= (A+B/50-C*50-D)./(denom);
S21= (2.*(A.*D-B.*C))./(denom);
figure(2)
plot(f,20*log10(S11),f,20*log10(S21))
```

Bibliography

Bibliography

[1]   J. L. Hilbert, "RF-MEMS for wireless communications," *Communications Magazine, IEEE,* vol. 46, pp. 68-74, 2008.

[2]   Y. Shim, "Fully Integrated High-Performance MEMS Lumped Element Filters for Reconfigurable Radios," 2013.

[3]   X. Zhu, *Switchable and Tunable ferroelectric thin film radio frequency components*: ProQuest, 2009.

[4]   I. F. Akyildiz, W.-Y. Lee, M. C. Vuran, and S. Mohanty, "NeXt generation/dynamic spectrum access/cognitive radio wireless networks: A survey," *Computer Networks,* vol. 50, pp. 2127-2159, 9/15/ 2006.

[5]   I. F. Akyildiz, L. Won-Yeol, M. C. Vuran, and S. Mohanty, "A survey on spectrum management in cognitive radio networks," *Communications Magazine, IEEE,* vol. 46, pp. 40-48, 2008.

[6]   C. Bin, Z. Qinyu, J. W. Mark, L. X. Cai, and H. V. Poor, "Toward efficient radio spectrum utilization: user cooperation in cognitive radio networking," *Network, IEEE,* vol. 26, pp. 46-52, 2012.

[7]   R. W. Brodersen, A. Wolisz, D. Cabric, S. M. Mishra, and D. Willkomm, "Corvus: a cognitive radio approach for usage of virtual unlicensed spectrum," *Berkeley Wireless Research Center (BWRC) White paper,* 2004.

[8]   M. Haddad, A. M. Hayar, and M. Debbah, "Spectral Efficiency of Cognitive Radio Systems," in *Global Telecommunications Conference, 2007. GLOBECOM '07. IEEE*, 2007, pp. 4165-4169.

[9]   S. Haykin, "Cognitive radio: brain-empowered wireless communications," *Selected Areas in Communications, IEEE Journal on,* vol. 23, pp. 201-220, 2005.

[10]   L. Won-Yeol and I. F. Akyildiz, "Optimal spectrum sensing framework for cognitive radio networks," *Wireless Communications, IEEE Transactions on,* vol. 7, pp. 3845-3857, 2008.

[11]   J. Z. a. M. A. Steven Mahon. (2008, August 2008) BAW Flip-Chip Switched Filter Bank Delivers Dramatic Form Factor Reduction. *High Frequency Electronics*. 24-28.

[12]   Available: http://www.herley.com/index.cfm?act=product&prd=537

[13]   A. Kozyrev, A. Mikhaylov, S. Ptashnik, S. Zinoviev, P. Petrov, N. Alford*, et al.*, "Electronically switchable bulk acoustic wave resonator based on paraelectric state ferroelectric films," *Electronics letters,* vol. 47, pp. 1326-1327, 2011.

[14]   S. Lee, V. Lee, S. A. Sis, and A. Mortazawi, "Large signal modeling of switchable ferroelectric FBARs," in *Microwave Integrated Circuits Conference (EuMIC), 2012 7th European*, 2012, pp. 24-27.

[15]   S. Lee, V. Lee, S. A. Sis, and A. Mortazawi, "Large-Signal Performance and Modeling of Intrinsically Switchable Ferroelectric FBARs," *Microwave Theory and Techniques, IEEE Transactions on,* vol. 61, pp. 415 - 422, 2013.

[16]   V. Lee, S. Lee, S. A. Sis, and A. Mortazawi, "Large signal performance of ferroelectric FBARs," in *Microwave Symposium Digest (MTT), 2012 IEEE MTT-S International*, 2012, pp. 1-3.

[17]   V. Lee, S. Sis, X. Zhu, and A. Mortazawi, "Intrinsically switchable interdigitated barium titanate thin film contour mode resonators," in *Microwave Symposium Digest (MTT), 2010 IEEE MTT-S International*, 2010, pp. 1448-1450.

[18]   V. Lee, S. A. Sis, S. Lee, and A. Mortazawi, "Intrinsically switchable ferroelectric bulk acoustic wave filters based on barium strontium titanate thin films," in *Wireless Symposium (IWS), 2013 IEEE International*, 2013, pp. 1-4.

[19]   V. Lee, S. A. Sis, J. D. Phillips, and A. Mortazawi, "Intrinsically Switchable Ferroelectric Contour Mode Resonators," *Microwave Theory and Techniques, IEEE Transactions on,* pp. 1-8, 2013.

[20]   V. Lee, S. A. Sis, X. Zhu, and A. Mortazawi, "Intrinsically switchable ferroelectric BAW resonators and filters," in *Microwave Conference (EuMC), 2010 European*, 2010, pp. 803-806.

[21]   A. Noeth, T. Yamada, P. Muralt, A. K. Tagantsev, and N. Setter, "Tunable thin film bulk acoustic wave resonator based on $Ba_xSr_{1-x}TiO_3$ thin film," *Ultrasonics, Ferroelectrics and Frequency Control, IEEE Transactions on,* vol. 57, pp. 379-385, 2010.

[22]   G. N. Saddik, D. S. Boesch, S. Stemmer, and R. A. York, "Strontium titanate DC electric field switchable and tunable bulk acoustic wave solidly mounted resonator," in *Microwave Symposium Digest, 2008 IEEE MTT-S International*, 2008, pp. 1263-1266.

[23]   G. N. Saddik and R. A. York, "An L-section DC electric field switchable bulk acoustic wave solidly mounted resonator filter based on $Ba_{0.5}Sr_{0.5}TiO_3$," *Ultrasonics, Ferroelectrics and Frequency Control, IEEE Transactions on,* vol. 59, pp. 2036-2041, 2012.

[24]   S. A. Sis, "Highly Linear 35 W Class F Power Amplifiers," Syracuse University, 2008.

[25]   S. A. Sis, V. Lee, S. Lee, and A. Mortazawi, "Intrinsically switchable thin film ferroelectric resonators utilizing electric field induced piezoelectric effect," in *Wireless Symposium (IWS), 2013 IEEE International*, 2013, pp. 1-4.

[26]   S. A. Sis, V. Lee, and A. Mortazawi, "Intrinsically switchable, BST-on-silicon composite FBARs," in *Microwave Symposium Digest (MTT), 2011 IEEE MTT-S International*, 2011, pp. 1-4.

[27]   S. A. Sis, V. Lee, J. D. Phillips, and A. Mortazawi, "Intrinsically switchable thin film ferroelectric resonators," in *Microwave Symposium Digest (MTT), 2012 IEEE MTT-S International*, 2012, pp. 1-3.

[28]   S. A. Sis, V. Lee, J. D. Phillips, and A. Mortazawi, "A DC voltage dependent switchable acoustically coupled BAW filter based on BST-on-silicon composite structure," in *Microwave Symposium Digest (MTT), 2012 IEEE MTT-S International*, 2012, pp. 1-3.

[29]   A. Volatier, E. Defay, M. Aid, A. Nhari, P. Ancey, and B. Dubus, "Switchable and tunable strontium titanate electrostrictive bulk acoustic wave resonator

integrated with a Bragg mirror," *Applied Physics Letters,* vol. 92, pp. 032906-032906-3, 2008.

[30] A. Vorobiev and S. Gevorgian, "Tunable thin film bulk acoustic wave resonators with improved Q-factor," *Applied Physics Letters,* vol. 96, pp. 212904-212904-3, 2010.

[31] B. Acikel, T. R. Taylor, P. J. Hansen, J. S. Speck, and R. A. York, "A new high performance phase shifter using $Ba_x Sr_{1-x} TiO_3$ thin films," *Microwave and Wireless Components Letters, IEEE,* vol. 12, pp. 237-239, 2002.

[32] L. Y. V. Chen, R. Forse, D. Chase, and R. A. York, "Analog tunable matching network using integrated thin-film BST capacitors," in *Microwave Symposium Digest, 2004 IEEE MTT-S International*, 2004, pp. 261-264 Vol.1.

[33] S. Courreges, L. Yuan, Z. Zhiyong, C. Kwang, A. Hunt, and J. Papapolymerou, "A Low Loss X-Band Quasi-Elliptic Ferroelectric Tunable Filter," *Microwave and Wireless Components Letters, IEEE,* vol. 19, pp. 203-205, 2009.

[34] E. G. Erker, A. S. Nagra, L. Yu, P. Periaswamy, T. R. Taylor, J. Speck*, et al.*, "Monolithic Ka-band phase shifter using voltage tunable $BaSrTiO_3$ parallel plate capacitors," *Microwave and Guided Wave Letters, IEEE,* vol. 10, pp. 10-12, 2000.

[35] J. Hai, M. Patterson, Z. Chenhao, and G. Subramanyam, "Frequency tunable microstrip patch antenna using ferroelectric thin film varactor," in *Aerospace & Electronics Conference (NAECON), Proceedings of the IEEE 2009 National*, 2009, pp. 248-250.

[36] J. Hai, M. Patterson, Z. Chenhao, and G. Subramanyam, "Frequency agile microstrip patch antenna using ferroelectric thin film varactor technology," in *Antennas and Propagation Society International Symposium, 2009. APSURSI '09. IEEE*, 2009, pp. 1-4.

[37] A. Jamil, T. S. Kalkur, and N. Cramer, "Tunable Ferroelectric Capacitor-Based Voltage-Controlled Oscillator," *Ultrasonics, Ferroelectrics and Frequency Control, IEEE Transactions on,* vol. 54, pp. 222-226, 2007.

[38] H. Katta, H. Kurioka, and Y. Yashima, "Tunable Power Amplifier Using Thin-Film BST Capacitors," in *Microwave Symposium Digest, 2006. IEEE MTT-S International*, 2006, pp. 564-567.

[39] J. Nath, D. Ghosh, J. P. Maria, A. I. Kingon, W. Fathelbab, P. D. Franzon*, et al.*, "An electronically tunable microstrip bandpass filter using thin-film Barium-Strontium-Titanate (BST) varactors," *Microwave Theory and Techniques, IEEE Transactions on,* vol. 53, pp. 2707-2712, 2005.

[40] J. Papapolymerou, C. Lugo, Z. Zhiyong, W. Xiaoyan, and A. Hunt, "A Miniature Low-Loss Slow-Wave Tunable Ferroelectric BandPass Filter From 11-14 GHz," in *Microwave Symposium Digest, 2006. IEEE MTT-S International*, 2006, pp. 556-559.

[41] J. Sigman, C. D. Nordquist, P. G. Clem, G. M. Kraus, and P. S. Finnegan, "Voltage-Controlled Ku-Band and X-Band Tunable Combline Filters Using Barium-Strontium-Titanate," *Microwave and Wireless Components Letters, IEEE,* vol. 18, pp. 593-595, 2008.

[42]   A. Tombak, J. P. Maria, F. Ayguavives, J. Zhang, G. T. Stauf, A. I. Kingon*, et al.*, "Tunable barium strontium titanate thin film capacitors for RF and microwave applications," *Microwave and Wireless Components Letters, IEEE,* vol. 12, pp. 3-5, 2002.

[43]   A. Tombak, J. P. Maria, F. T. Ayguavives, J. Zhang, G. T. Stauf, A. I. Kingon*, et al.*, "Voltage-controlled RF filters employing thin-film barium-strontium-titanate tunable capacitors," *Microwave Theory and Techniques, IEEE Transactions on,* vol. 51, pp. 462-467, 2003.

[44]   A. Victor, J. Nath, D. Ghosh, B. Boyette, J. P. Maria, M. B. Steer*, et al.*, "A voltage controlled oscillator using barium strontium titanate (BST) thin film varactor," in *Radio and Wireless Conference, 2004 IEEE*, 2004, pp. 91-94.

[45]   F. Zhiping, W. M. Fathelbab, P. G. Lam, V. Haridasan, J. P. Maria, A. I. Kingon*, et al.*, "Narrowband Barium Strontium Titanate (BST) tunable bandpass filters at X-band," in *Microwave Symposium Digest, 2009. MTT '09. IEEE MTT-S International*, 2009, pp. 1061-1064.

[46]   A. Artieda and P. Muralt, "High-Q AlN/SiO$_2$ symmetric composite thin film bulk acoustic wave resonators," *Ultrasonics, Ferroelectrics and Frequency Control, IEEE Transactions on,* vol. 55, pp. 2463-2468, 2008.

[47]   K. M. Lakin, G. R. Kline, and K. T. McCarron, "High-Q microwave acoustic resonators and filters," *Microwave Theory and Techniques, IEEE Transactions on,* vol. 41, pp. 2139-2146, 1993.

[48]   K. M. Lakin and J. S. Wang, "UHF Composite Bulk Wave Resonators," in *1980 Ultrasonics Symposium*, 1980, pp. 834-837.

[49]   J. Rosenbaum, "Design of Ultra High Frequency Composite Piezoelectric Resonators," in *Applications of Ferroelectrics. 1986 Sixth IEEE International Symposium on*, 1986, pp. 296-299.

[50]   J. Rosenbaum, H. L. Salvo, Jr., and S. V. Krishnaswamy, "Overtone Response of Composite Bulk Acoustic Resonators," in *40th Annual Symposium on Frequency Control. 1986*, 1986, pp. 206-210.

[51]   R. Ruby, "11E-2 Review and Comparison of Bulk Acoustic Wave FBAR, SMR Technology," in *Ultrasonics Symposium, 2007. IEEE*, 2007, pp. 1029-1040.

[52]   M. Rais-Zadeh, "Title," unpublished|.

[53]   E. Yoon, "EECS 414- Introduction to MEMS," September 2009 2009.

[54]   F. D. Bannon, J. R. Clark, and C. T. C. Nguyen, "High-Q HF microelectromechanical filters," *Solid-State Circuits, IEEE Journal of,* vol. 35, pp. 512-526, 2000.

[55]   I. J. Busch-Vishniac, "Trends in electromechanical transduction," *Physics Today,* vol. 51, p. 28, 1998.

[56]   W. Jing, R. Zeying, and C. T. C. Nguyen, "1.156-GHz self-aligned vibrating micromechanical disk resonator," *Ultrasonics, Ferroelectrics and Frequency Control, IEEE Transactions on,* vol. 51, pp. 1607-1628, 2004.

[57]   T. Mattila, A. Oja, H. Seppa, O. Jaakkola, J. Kiihamaki, H. Kattelus*, et al.*, "Micromechanical bulk acoustic wave resonator," in *Ultrasonics Symposium, 2002. Proceedings. 2002 IEEE*, 2002, pp. 945-948 vol.1.

[58]   S. Pourkamali, A. Hashimura, R. Abdolvand, G. K. Ho, A. Erbil, and F. Ayazi, "High-Q single crystal silicon HARPSS capacitive beam resonators with self-

aligned sub-100-nm transduction gaps," *Microelectromechanical Systems, Journal of,* vol. 12, pp. 487-496, 2003.

[59] S. Pourkamali, G. K. Ho, and F. Ayazi, "Low-Impedance VHF and UHF Capacitive Silicon Bulk Acoustic Wave Resonators—Part I: Concept and Fabrication," *Electron Devices, IEEE Transactions on,* vol. 54, pp. 2017-2023, 2007.

[60] S. Pourkamali, G. K. Ho, and F. Ayazi, "Low-Impedance VHF and UHF Capacitive Silicon Bulk Acoustic-Wave Resonators—Part II: Measurement and Characterization," *Electron Devices, IEEE Transactions on,* vol. 54, pp. 2024-2030, 2007.

[61] S. Pourkamali, H. Zhili, and F. Ayazi, "VHF single crystal silicon capacitive elliptic bulk-mode disk resonators-part II: implementation and characterization," *Microelectromechanical Systems, Journal of,* vol. 13, pp. 1054-1062, 2004.

[62] M. W. Putty, S. C. Chang, R. T. Howe, A. L. Robinson, and K. D. Wise, "One-port active polysilicon resonant microstructures," in *Micro Electro Mechanical Systems, 1989, Proceedings, An Investigation of Micro Structures, Sensors, Actuators, Machines and Robots. IEEE*, 1989, pp. 60-65.

[63] H. Zhili, S. Pourkamali, and F. Ayazi, "VHF single-crystal silicon elliptic bulk-mode capacitive disk resonators-part I: design and modeling," *Microelectromechanical Systems, Journal of,* vol. 13, pp. 1043-1053, 2004.

[64] E. E. Aktakka, "Integration of bulk piezoelectric materials into microsystems," The University of Michigan, 2012.

[65] C. S. McGahey, "Harnessing nature's timekeeper: a history of the piezoelectric quartz crystal technological community (1880-1959)," Citeseer, 2009.

[66] Available: http://www.diamond.ac.uk/Home/Science/Highlights/casestudy9.html

[67] S. Majumder, B. Perez, B. Roy, A. Martinez, and R. Katiyar, "Electrical Characteristics of Chemical Solution Deposited Nd^ 3^+ Doped PZT (53/47) Thin Films in Planar Electrode Configuration," in *MATERIALS RESEARCH SOCIETY SYMPOSIUM PROCEEDINGS*, 2001, pp. CC12. 14-CC12. 14.

[68] A. Ballato, "Piezoelectricity: old effect, new thrusts," *Ultrasonics, Ferroelectrics and Frequency Control, IEEE Transactions on,* vol. 42, pp. 916-926, 1995.

[69] J. F. Rosenbaum, *Bulk acoustic wave theory and devices* vol. 147: Artech House Boston, 1988.

[70] "IEEE Standard on Piezoelectricity," *ANSI/IEEE Std 176-1987,* p. 0_1, 1988.

[71] R. Weigel, D. P. Morgan, J. M. Owens, A. Ballato, K. M. Lakin, K.-Y. Hashimoto*, et al.*, "Microwave acoustic materials, devices, and applications," *Microwave Theory and Techniques, IEEE Transactions on,* vol. 50, pp. 738-749, 2002.

[72] J. G. Rodriguez-Madrid, G. F. Iriarte, J. Pedros, O. A. Williams, D. Brink, and F. Calle, "Super-High-Frequency SAW Resonators on AlN/Diamond," *Electron Device Letters, IEEE,* vol. 33, pp. 495-497, 2012.

[73] G. Piazza, P. J. Stephanou, and A. P. Pisano, "Piezoelectric Aluminum Nitride Vibrating Contour-Mode MEMS Resonators," *Microelectromechanical Systems, Journal of,* vol. 15, pp. 1406-1418, 2006.

[74] M. Rinaldi, C. Zuniga, C. Zuo, and G. Piazza, "Super-high-frequency two-port AlN contour-mode resonators for RF applications," *IEEE transactions on ultrasonics, ferroelectrics, and frequency control,* vol. 57, pp. 38-45, 2010.

[75] C. S. Hwang, S. O. Park, H. J. Cho, C. S. Kang, H. K. Kang, S. I. Lee*, et al.*, "Deposition of extremely thin (Ba, Sr) TiO 3 thin films for ultra-large-scale integrated dynamic random access memory application," *Applied physics letters,* vol. 67, pp. 2819-2821, 1995.

[76] A. I. Kingon, J.-P. Maria, and S. Streiffer, "Alternative dielectrics to silicon dioxide for memory and logic devices," *Nature,* vol. 406, pp. 1032-1038, 2000.

[77] B. Nagaraj, T. Sawhney, S. Perusse, S. Aggarwal, R. Ramesh, V. Kaushik*, et al.*, "(Ba, Sr) TiO thin films with conducting perovskite electrodes for dynamic random access memory applications," *Applied physics letters,* vol. 74, p. 3194, 1999.

[78] B. York, "Tunable dielectrics for RF circuits," *Multifunctional adaptive microwave circuits and systems,* pp. 159-207, 2009.

[79] D.-Y. Chen and J. D. Phillips, "Electric field dependence of piezoelectric coefficient in ferroelectric thin films," *Journal of electroceramics,* vol. 17, pp. 613-617, 2006.

[80] D. Damjanovic and R. Newnham, "Electrostrictive and piezoelectric materials for actuator applications," *Journal of intelligent material systems and structures,* vol. 3, pp. 190-208, 1992.

[81] D. Guyomar, P. J. Cottinet, L. Lebrun, C. Putson, K. Yuse, M. Kanda*, et al.*, "The compressive electrical field electrostrictive coefficient M33 of electroactive polymer composites and its saturation versus electrical field, polymer thickness, frequency, and fillers," *Polymers for Advanced Technologies,* vol. 23, pp. 946-950, 2012.

[82] Z. Xinen, J. D. Phillips, and A. Mortazawi, "A DC Voltage Dependant Switchable Thin Film Bulk Wave Acoustic Resonator Using Ferroelectric Thin Film," in *Microwave Symposium, 2007. IEEE/MTT-S International*, 2007, pp. 671-674.

[83] Z. Xinen, V. Lee, J. Phillips, and A. Mortazawi, "An Intrinsically Switchable FBAR Filter Based on Barium Titanate Thin Films," *Microwave and Wireless Components Letters, IEEE,* vol. 19, pp. 359-361, 2009.

[84] K.-y. Hashimoto, *RF bulk acoustic wave filters for communications*: Artech House, 2009.

[85] J. Hu, R. Parkery, R. Ruby, and B. Otis, "A wide-tuning digitally controlled FBAR-based oscillator for frequency synthesis," in *Frequency Control Symposium (FCS), 2010 IEEE International*, 2010, pp. 608-612.

[86] A. P. S. Khanna, E. Gane, and T. Chong, "A 2GHz voltage tunable FBAR oscillator," in *Microwave Symposium Digest, 2003 IEEE MTT-S International*, 2003, pp. 717-720 vol.2.

[87] L. Mingdong, S. Seok, N. Rolland, P. A. Rolland, H. El Aabbaoui, E. De Foucauld*, et al.*, "Comparison of low phase noise oscillators topologies using BAW resonator," in *Microwave Integrated Circuits Conference (EuMIC), 2010 European*, 2010, pp. 345-348.

[88] P. Wei, R. C. Ruby, R. Parker, P. W. Fisher, J. D. Larson, III, K. J. Grannen*, et al.*, "11E-3 A Thermally Stable CMOS Oscillator Using Temperature

Compensated FBAR," in *Ultrasonics Symposium, 2007. IEEE*, 2007, pp. 1041-1044.

[89] Y. Osugi, T. Yoshino, K. Suzuki, and T. Hirai, "Single crystal FBAR with LiNbO3 and LiTaO3 piezoelectric substance layers," in *Microwave Symposium, 2007. IEEE/MTT-S International*, 2007, pp. 873-876.

[90] M. Rinaldi, C. Zuniga, C. Zuo, and G. Piazza, "AlN contour-mode resonators for narrow-band filters above 3 GHz," in *2009 Joint Meeting of the European Frequency and Time Forum and the IEEE International Frequency Control Symposium (EFTF-IFCS 2009)*, 2009, pp. 70-74.

[91] R. Ruby, "FBAR-from technology development to production," in *2nd International Symposium on Acoustic Wave Devices for Future Mobile Communication Systems*, 2004.

[92] M. Norling, J. Berge, and S. Gevorgian, "Parameter extraction for tunable TFBARs based on Ba<inf>x</inf>Sr<inf>1−x</inf>TiO<inf>3</inf>," in *Microwave Symposium Digest, 2009. MTT '09. IEEE MTT-S International*, 2009, pp. 101-104.

[93] H. M. Lavasani, R. Abdolvand, and F. Ayazi, "A 500MHz Low Phase-Noise A1N-on-Silicon Reference Oscillator," in *Custom Integrated Circuits Conference, 2007. CICC '07. IEEE*, 2007, pp. 599-602.

[94] J. D. Larson, III, R. C. Bradley, S. Wartenberg, and R. C. Ruby, "Modified Butterworth-Van Dyke circuit for FBAR resonators and automated measurement system," in *Ultrasonics Symposium, 2000 IEEE*, 2000, pp. 863-868 vol.1.

[95] K. Kun-Wook, G. Myeong-Gweon, Y. Jong-Gwan, and P. Han-Kyu, "Resonator size effects on the TFBAR ladder filter performance," *Microwave and Wireless Components Letters, IEEE,* vol. 13, pp. 335-337, 2003.

[96] X. Wencheng, Z. Xu, S. Choi, and C. Junseok, "A High-Quality-Factor Film Bulk Acoustic Resonator in Liquid for Biosensing Applications," *Microelectromechanical Systems, Journal of,* vol. 20, pp. 213-220, 2011.

[97] F. F. C. Duval, R. A. Dorey, R. W. Wright, H. Zhaorong, and R. W. Whatmore, "Fabrication and modeling of high-frequency PZT composite thick film membrance resonators," *Ultrasonics, Ferroelectrics and Frequency Control, IEEE Transactions on,* vol. 51, pp. 1255-1261, 2004.

[98] H. P. Hsu, "On The General Relation Between /spl alpha/ and Q (Correspondence)," *Microwave Theory and Techniques, IEEE Transactions on,* vol. 11, pp. 258-258, 1963.

[99] Z. Xinen, C. Ding-Yuan, J. Zhang, J. D. Phillips, and A. Mortazawi, "Characterization of thin film BST tunable capacitors using a simple two port measurement technique," in *Microwave Symposium Digest, 2005 IEEE MTT-S International*, 2005, p. 4 pp.

[100] C. Muller and M. A. Dubois, "Effect of size and shape on the performances of BAW resonators: A model and its applications," in *Ultrasonics Symposium, 2008. IUS 2008. IEEE*, 2008, pp. 1552-1556.

[101] R. Abdolvand and F. Ayazi, "7E-4 Enhanced Power Handling and Quality Factor in Thin-Film Piezoelectric-on-Substrate Resonators," in *Ultrasonics Symposium, 2007. IEEE*, 2007, pp. 608-611.

[102] R. Ohara, N. Yanase, T. Yasumoto, M. Kawase, S. Masuko, T. Ohno*, et al.*, "P2G-4 Suppression of Acoustic Energy Leakage in FBARs with Al Bottom Electrode: FEM Simulation and Experimental Results," in *Ultrasonics Symposium, 2007. IEEE*, 2007, pp. 1657-1660.

[103] R. C. Ruby, P. Bradley, Y. Oshmyansky, A. Chien, and J. D. Larson, III, "Thin film bulk wave acoustic resonators (FBAR) for wireless applications," in *Ultrasonics Symposium, 2001 IEEE*, 2001, pp. 813-821 vol.1.

[104] D. M. Pozar, *Microwave engineering*: Wiley. com, 2009.

[105] T. Pensala, J. Meltaus, K. Kokkonen, and M. Ylilammi, "2-D modeling of laterally acoustically coupled thin film bulk acoustic wave resonator filters," *Ultrasonics, Ferroelectrics and Frequency Control, IEEE Transactions on,* vol. 57, pp. 2537-2549, 2010.

[106] K. M. Lakin, "Coupled resonator filters," in *Ultrasonics Symposium, 2002. Proceedings. 2002 IEEE*, 2002, pp. 901-908 vol.1.

[107] K. M. Lakin, "Bulk acoustic wave coupled resonator filters," in *Frequency Control Symposium and PDA Exhibition, 2002. IEEE International*, 2002, pp. 8-14.

[108] K. M. Lakin, "Thin film resonator technology," *Ultrasonics, Ferroelectrics and Frequency Control, IEEE Transactions on,* vol. 52, pp. 707-716, 2005.

[109] K. M. Lakin, J. Belsick, J. F. McDonald, and K. T. McCarron, "High performance stacked crystal filters for GPS and wide bandwidth applications," in *Ultrasonics Symposium, 2001 IEEE*, 2001, pp. 833-838 vol.1.

[110] W. Beaver, "Theory and design of the monolithic crystal filter," in *21st Annual Symposium on Frequency Control. 1967*, 1967, pp. 179-199.

[111] W. D. Beaver, *Theory and design principles of the monolithic crystal filter*: UMI Dissertation Service, 1988.

[112] R. Rennick, "An equivalent circuit approach to the design and analysis of monolithic crystal filters," *Sonics and Ultrasonics, IEEE Transactions on,* vol. 20, pp. 347-353, 1973.

[113] J. Meltaus, T. Pensala, and K. Kokkonen, "Parametric study of laterally acoustically coupled bulk acoustic wave filters," *Ultrasonics, Ferroelectrics and Frequency Control, IEEE Transactions on,* vol. 59, pp. 2742-2751, 2012.

[114] J. Meltaus, T. Pensala, K. Kokkonen, and A. Jansman, "Laterally coupled solidly mounted BAW resonators at 1.9 GHz," in *Ultrasonics Symposium (IUS), 2009 IEEE International*, 2009, pp. 847-850.

[115] W. Pan, R. Abdolvand, and F. Ayazi, "A low-loss 1.8 GHz monolithic thin-film piezoelectric-on-substrate filter," in *Micro Electro Mechanical Systems, 2008. MEMS 2008. IEEE 21st International Conference on*, 2008, pp. 176-179.

[116] V. A. Thakar, W. Pan, F. Ayazi, and M. Rais-Zadeh, "Acoustically coupled thickness-mode AIN-on-Si band-pass filters-Part II: simulation and analysis," *Ultrasonics, Ferroelectrics and Frequency Control, IEEE Transactions on,* vol. 59, pp. 2270-2277, 2012.

[117] P. Wanling, V. A. Thakar, M. Rais-Zadeh, and F. Ayazi, "Acoustically coupled thickness-mode AIN-on-Si band-pass filters-part I: principle and devices," *Ultrasonics, Ferroelectrics and Frequency Control, IEEE Transactions on,* vol. 59, pp. 2262-2269, 2012.

[118] R. Abdolvand and F. Ayazi, "Monolithic Thin-Film Piezoelectric-on-Substrate Filters," in *Microwave Symposium, 2007. IEEE/MTT-S International*, 2007, pp. 509-512.